Review of the Scalable Core–Shell Synthesis Methods: The Improvements of Li-Ion Battery Electrochemistry and Cycling Stability

Suchakree Tubtimkuna, Dmitri L. Danilov, Montree Sawangphruk,
*and Peter H. L. Notten**

The demand for lithium-ion batteries has significantly increased due to the increasing adoption of electric vehicles (EVs). However, these batteries have a limited lifespan, which needs to be improved for the long-term use needs of EVs expected to be in service for 20 years or more. In addition, the capacity of lithium-ion batteries is often insufficient for long-range travel, posing challenges for EV drivers. One approach that has gained attention is using core–shell structured cathode and anode materials. That approach can provide several benefits, such as extending the battery lifespan and improving capacity performance. This paper reviews various challenges and solutions by the core–shell strategy adopted for both cathodes and anodes. The highlight is scalable synthesis techniques, including solid phase reactions like the mechanofusion process, ball-milling, and spray-drying process, which are essential for pilot plant production. Due to continuous operation with a high production rate, compatibility with inexpensive precursors, energy and cost savings, and an environmentally friendly approach that can be carried out at atmospheric pressure and ambient temperatures. Future developments in this field may focus on optimizing core–shell materials and synthesis techniques for improved Li-ion battery performance and stability.

S. Tubtimkuna, D. L. Danilov, P. H. L. Notten
Fundamental Electrochemistry (IEK-9) Forschungszentrum Jülich
D-52425 Jülich, Germany
E-mail: p.h.l.notten@tue.nl
S. Tubtimkuna, M. Sawangphruk
Department of Chemical and Biomolecular Engineering School of Energy
Science and Engineering Vidyasirimedhi Institute of Science and Technology
Rayong 21210, Thailand
D. L. Danilov, P. H. L. Notten
Eindhoven University of Technology Eindhoven
Eindhoven, MB 5600, The Netherlands
P. H. L. Notten
University of Technology Sydney Broadway
Sydney, NS 2007, Australia

1. Introduction

Lithium-ion batteries (LIBs), frequently utilized as the main power source for EVs, are in high demand due to the growing popularity of electric cars (EVs). However, the typical cycle-life for these batteries is ≈4000–5000 cycles or around 10 years. There is a strong need to improve the cycle-life in order to meet the long-term demands of EVs, which are expected to be in operation for 20 years or more. In addition, the capacity of LIBs is often limited for long-range travel, which can be a challenge for EV drivers. Researchers and battery manufacturers are exploring ways to extend the lifespan and boost the capacity of LIBs to address these challenges and support the transition to a low-carbon transportation system.[1]

Using a core–shell structure in cathode and anode materials of LIBs is one strategy that has gained interest. It can offer several advantages, including an increased lifespan and improved capacity performance.[2] The core–shell structure can enhance the electrochemical performance and battery stability because 1) the shell layer of the cathode material has the potential to serve as a barrier that keeps the core material from coming into direct contact with the electrolyte. Avoiding chemical interactions between the core material and the electrolyte can assist in avoiding degradation of the core material. A stable solid-electrolyte interface (SEI) layer is created at the shell layer of the anode material, inhibiting aggregation, and buffering significant volume change. 2) The total electrode conductivity can be increased by covering the core material with a shell layer that has a higher electronic conductivity since the core material may have a lower electronic conductivity than the shell material. This technique can reduce electrode resistance and improve the overall performance of the battery. Core–shell synthesis techniques are a crucial aspect of the pilot plant-scale production of LIBs due to their ability to efficiently produce large quantities of high-quality cathode and anode materials with desired core–shell structures. While liquid and gas phase reactions have traditionally been the most common techniques for applying coatings on cathode and anode materials, they come with various challenges, including environmental concerns, low yields, high precursor costs, expansive reactions, and difficulties in

**ADVANCED
SCIENCE NEWS**

www.advancedsciencenews.com
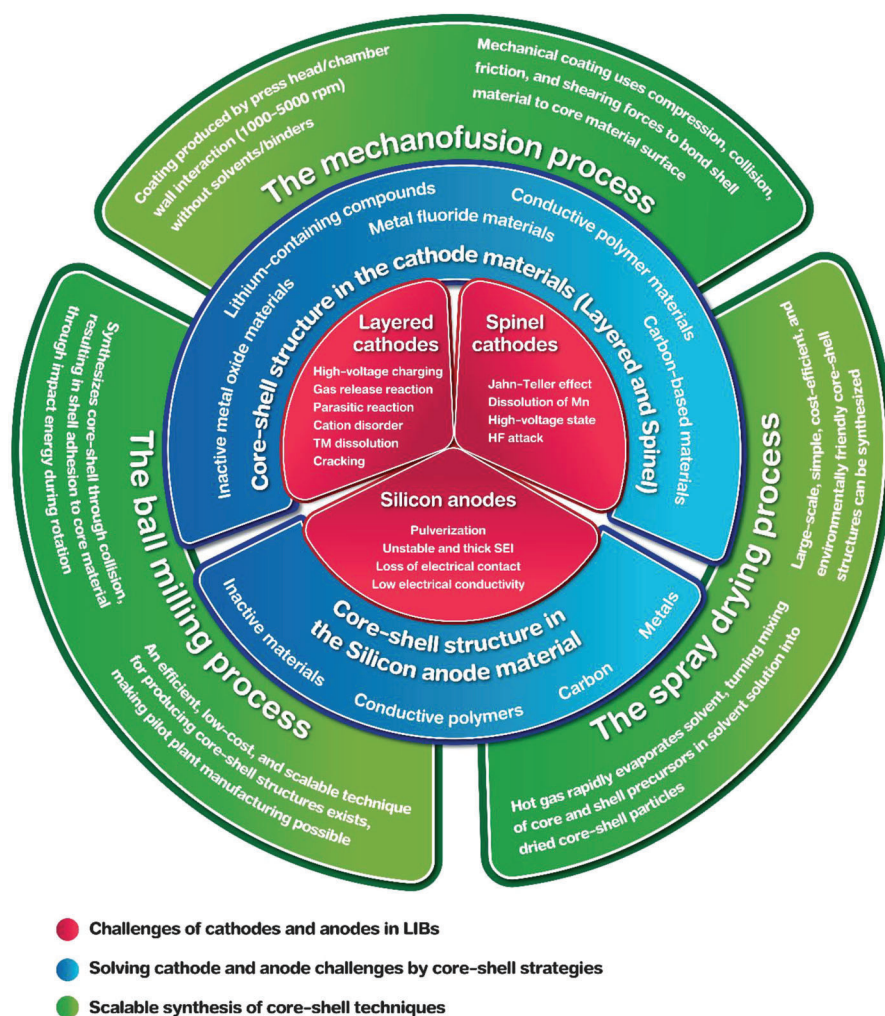
**small
methods**

www.small-methods.com

Figure 1. Challenges in layered and spinel cathodes and silicon anodes in LIBs are addressed through core–shell strategies and scalable synthesis techniques.

scaling up. As such, solid reactions have gained significant attention in recent years as a promising alternative for coating core–shell structures in LIBs. These reactions offer several benefits, including continuous operation with a high production rate, compatibility with inexpensive precursors, energy and cost savings, and an environmentally friendly approach that can be carried out at atmospheric pressure and environmental temperatures.

The review discusses the challenges of both cathode and anode materials in LIBs and how a core–shell strategy can help to address these challenges. The cathode materials discussed include layer and spinel materials, while the discussed anode material is focusing on silicon. The core–shell strategy involves creating a protective layer around the core material to improve its performance and stability in LIBs. This review also discusses scalable synthesis techniques for producing core–shell materials, including solid-phase reactions such as the mechanofusion, ball-milling, and spray-drying process (**Figure 1**). In conclusion, the review highlights the potential of the core–shell strategies in addressing the challenges of cathode and anode materials in LIBs. Scalable synthesis techniques, such as solid-phase

reactions are essential for the pilot plant production of these materials. The use of core–shell materials in LIBs has the potential to improve their performance and stability, making them more viable for large-scale applications. Future developments in this area will likely focus on further optimizing the synthesis and performance of these materials.

2. Cathode Challenges in LIBs

2.1. Layered Cathodes

2.1.1. High-Voltage Charging

The practical reversible specific capacity of $LiCoO_2$ (LCO) is only half its theoretical limit (274 mAh·g^{-1}) at a cut-off voltage of 4.2 V versus Li/Li$^+$.[3] Therefore, to increase the specific capacity, it is necessary to charge the cells above the standard voltage of 4.2 V.[4] When the cut-off voltage increases to 4.5 V, the capacity is approximately 220 mAh·g^{-1}.[5] Unfortunately, several serious challenges limit LCO from being used in high-voltage conditions. First, at

**ADVANCED
SCIENCE NEWS**
www.advancedsciencenews.com
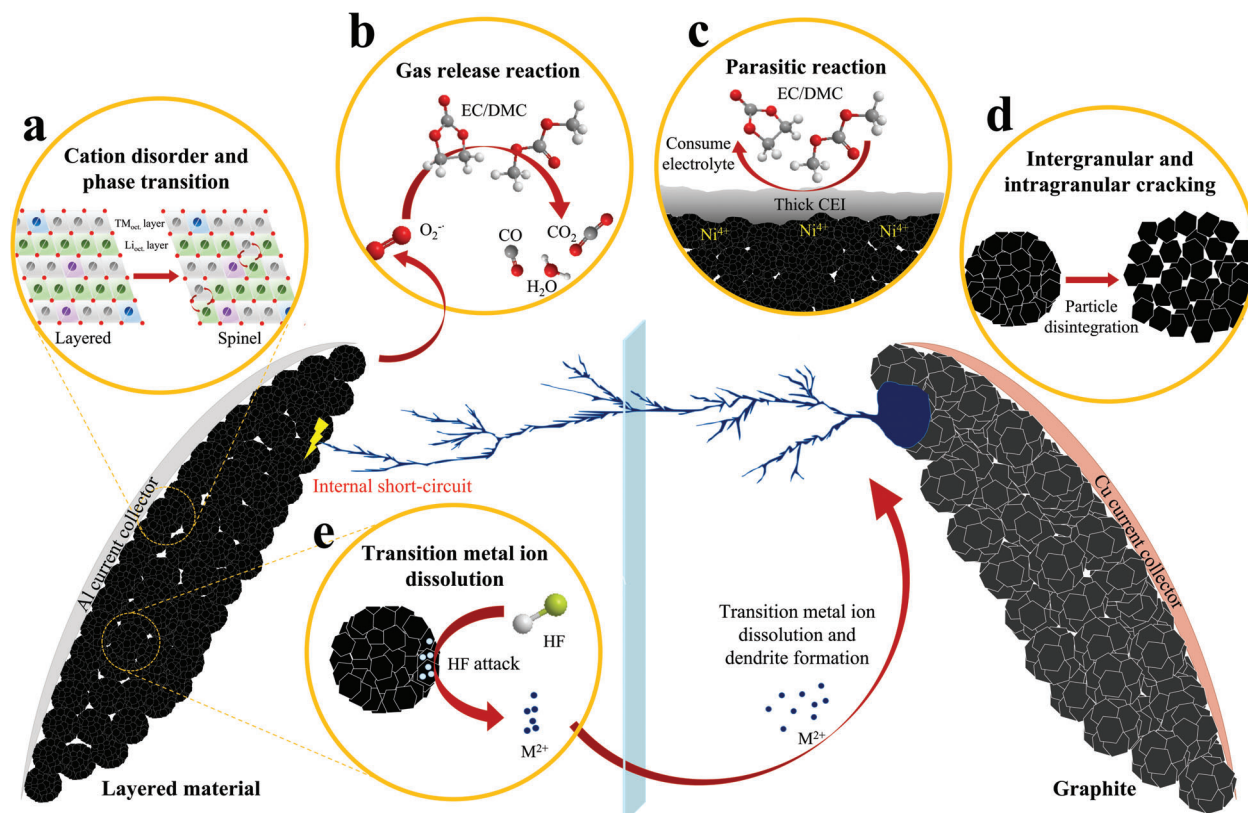
**small
methods**
www.small-methods.com

Figure 2. Schematic representation of the key challenges of layered cathodes in LIBs: a) cation disorder and phase transition, b) gas release reaction, c) parasitic reaction, d) intergranular and intragranular cracking, and e) transition metal ion dissolution.

high-voltage charging, too much Li^+ is extracted from the LCO layered structure, and the layered lattice transition metal (TM) slab tends to collapse. This phenomenon causes instability of the LCO structure and the unfavorable phase transition (O3 phase to O6 phase or H1–H3 at ≈4.5 V vs Li/Li^+). The resultant irreversible transformation destroys the layered LCO structure.[4a,6] Second, Co^{3+} is oxidized to Co^{4+} at the LCO surface when the voltage is high. Subsequently, Co^{4+} ions react with the organic electrolyte and may cause side reactions. These reactions destabilize the bulk structure and accelerate the irreversible loss of the active transition metal. That finally leads to poor cycling performance and severe capacity fading.[7]

2.1.2. Cation Disorder and Phase Transition

Cation disorder is a phenomenon known as mixing between Ni^{2+} and Li^+ in the Li slab layers. Ni, as part of NMC (Ni-rich) material, is partially located in the transition metal layer (Ni, Mn, and Co share similar crystal) as Ni^{2+} (0.69 Å). It possesses a similar ionic radius as Li^+ (0.76 Å).[8] Therefore, Ni^{2+} and Li^+ can easily exchange positions in the delithiated state through Ni^{2+} diffusion to the octahedral sites of Li^+ to neighboring tetrahedral sites.[9] During long-term cycling, cation mixing transforms the crystal structure from a layered structure via a spinel phase to a final rock-salt structure, as shown in **Figure 2**a. The Li^+ mobility is impeded due to this cation disordering. That reduces the rate capability and

causes rapid capacity fading of LIBs using Ni-rich cathodes. In addition, the rock-salt structure (ion-insulating) can release O_2 to the environment. It can react with the organic electrolyte to generate CO_2 and increase the interfacial resistance of electrodes due to high kinetic barriers in the Li^+ insertion/desertion process.[8] This tendency for Li/Ni mixing occurs much more frequently as the Ni ratio, operating temperature, cut-off voltage, and SOC increase.

2.1.3. Gas Release Reactions

The most dangerous safety concern of LIBs is the problem of gas formation and leakage. There is a serious risk of batteries exploding catastrophically due to the exothermic reactions involved during gas release. These reactions result in a series of chain reactions.[10] CO, CO_2, and H_2O are the byproducts of gaseous decomposition reactions (Figure 2b). In Ni-rich (NMC) cathodes, gas generation is caused by three factors:

1) Ni-rich material is generally less stable at the charged state. The interaction between the electrolyte and the surface of the active material leads to the loss of oxygen from the lattice caused by structural change of layered structure into the rock salt structure.[11]
2) Decomposition of inactive Li_2CO_3 and reaction with the electrolyte.[12]
3) Direct electrolyte oxidation.[13]

2300345 (3 of 46)

**ADVANCED
SCIENCE NEWS**

www.advancedsciencenews.com

**small
methods**

www.small-methods.com

2.1.4. Parasitic Reactions

Effect of Ni^{4+}: In the high-voltage state, large amounts of reactive Ni^{4+} are generated that can directly react with the electrolyte. That results in the formation of thick cathode electrolyte interphase (CEI) layers. This formation leads to the consumption of electrolytes, gas evolution, and increased impedance, as illustrated in Figure 2c.[14] Higher cut-off voltages and elevated temperatures intensify these reactions. Li$_2$CO$_3$, Li$_x$PO$_y$F$_z$, Li$_x$PF$_y$, and LiF are the main compounds reported in the CEI of Ni-rich materials.[15]

CO$_2$ Generation: A high concentration of Ni^{4+} at high voltage can increase the CO$_2$ evolution.[16] Note that cathodes with higher Ni content are more sensitive to parasitic reactions with Ni^{4+}. Moreover, the interaction of oxygen with carbonate-base electrolytes is another source of CO$_2$.[17] Other reactions that result in the production of CO$_2$ include solvent hydrolysis (if OH$^-$ ions are present), oxidation of electrolyte impurities, and hydrofluoric acid (HF) interaction with lithium carbonate at the surface impurity.[18] The challenges led to capacity fading, short cycling life, poor rate capability, gas release, and thermal runaway.

2.1.5. Intergranular and Intragranular Cracking

In the charging process, Li$^+$ is extracted from the lattice, and the repulsion between O^{2-} layer decreases with increased TM-O covalent bonding. Lattice expansion along the *c*-axis and shrinkage along the *a*- and *b*-axis can result from increased electrostatic interaction between neighboring TM layers.[19] The stress created by the non-uniform accommodation of this volume change might cause mechanical failure. In the real world, layered cathode materials are secondary particles created from densely packed primary particles. However, secondary particles generally produce intergranular cracks throughout the charge and discharge cycling process (Figure 2d) due to the anisotropic expansion and contraction of primary particles.[20] The microstrain in cracking material destruction is one of the essential degradation mechanisms for cathode materials. First, low grain-to-grain connections caused by cracks can result in low electrical conductivity and even the fragmentation of active materials, resulting in material losses. Second, the cracking provides new surfaces that are exposed to electrolytes and produce additional locations for corrosion, side reactions, and surface phase transition, which accelerates the degradation of batteries.[21] Defects in the Ni–Li antisites and lattice disorder, as well as Columbic repulsion between the ions, frequently cause intragranular cracking. During prolonged cycling, the lattice defects in the pristine particles keep getting worse and finally turn into nanoscale cracks. Furthermore, intragranular cracking is a mechanical failure and structural degradation under extreme electrochemical conditions.[22]

2.1.6. Transition Metal Ion Dissolution

The dissolution of transition metal ions occurs when metal interacts with acidic species present in the liquid electrolytes. Acidic species are generated in the liquid electrolyte through hydrolysis of LiPF$_6$ to form HF.[18] As a result, HF will corrode the cathodes and cause the dissolution of transition metal ions from the cathodes.[18,23] Furthermore, Mn produces Mn^{4+} and Mn^{2+} ions by disproportionating Mn^{3+} after an HF attack. Mn^{2+} is also soluble in electrolytes. Its presence on the anode implies capacity fading because it reduces the number of Li$^+$ insertion sites.[14b,23,24] Mn^{2+} can further migrate and deposit at the anode side, catalyzing electrolyte reduction and SEI formation.[25] In addition, the accumulation of Mn at the anode can lead to internal short-circuits caused by the Mn dendrite penetrating through the polymer separator. That causes direct contact between the anode and cathode, as schematically shown in Figure 2e. Only HF attack-induced TM dissolution dominates at low voltages. At high voltages, fast oxidation of both the electrolyte and cathode followed by cation exchange dominates to generate soluble TM complexes. The resulting dissolution of NMC materials can also result in capacity attenuation.[26]

2.1.7. Thermal Instability

During the delithiation process, phase transition of LCO is initiated at higher than 200 °C (from layered to spinel) to form O−O bonds and oxygen release. This process leads to the formation of electrochemically inactive phases with less oxygen in their stoichiometry (rock-salt phase).[27] Moreover, the alloying strategy has been promising to increase the structural and thermal stability of high-capacity layered oxide cathode materials. NMC (LiNi$_{1−x−y}$Mn$_y$Co$_x$O$_2$) and NCA (LiNi$_{1−x−y}$Co$_y$Al$_x$O$_2$) cathodes were successfully created and commercialized.[28] Compared to LCO, these materials exhibit better Li-stoichiometry, enhanced electrochemical performance, and higher thermal stability.[29] NMC433 exhibited the first phase transition at 250 °C, and there was no rock-salt phase until after 600 °C. However, phase transitions of NMC811 (Ni-rich) are observed at the lower temperature of 135 °C. The final phase transition to the rock-salt phase is observed at 365 °C.[30] The weaker M−O bonds in the delithiated state have also been associated with the thermal instability of Ni-rich cathodes. The oxygen binding energy indicates the strength of the M−O bonds as a function of Li concentration in different NMCs.[31] It is evident that when the Ni content of NMC increases and Li deintercalation occurs, the oxygen binding energy decreases. As a result, oxygen is liberated in a strongly delithiated form, causing Ni ions lowered from a higher valence state to undergo an exothermic process. Thus, the Ni-rich cathode challenged the thermal stability during battery operation. The system will produce heat. For this reason, there is a chance of heat leaks or, in extreme cases, even explosion.[32]

2.2. Spinel Cathode

2.2.1. Jahn-Teller Effect

The Jahn-Teller effect is a phenomenon describing the distortion of the geometric arrangement of molecules due to the asymmetric e$^-$ (electron) occupancy in the degraded orbital (**Figure 3**a). This process reduces the symmetry and degeneration of molecules and the system's energy.[33] At the discharge state, the valence state of Mn decreases with the continued embedding of lithium ions. Mn^{4+} will also be converted to Mn^{3+}, causing the

ADVANCED
SCIENCE NEWS
www.advancedsciencenews.com

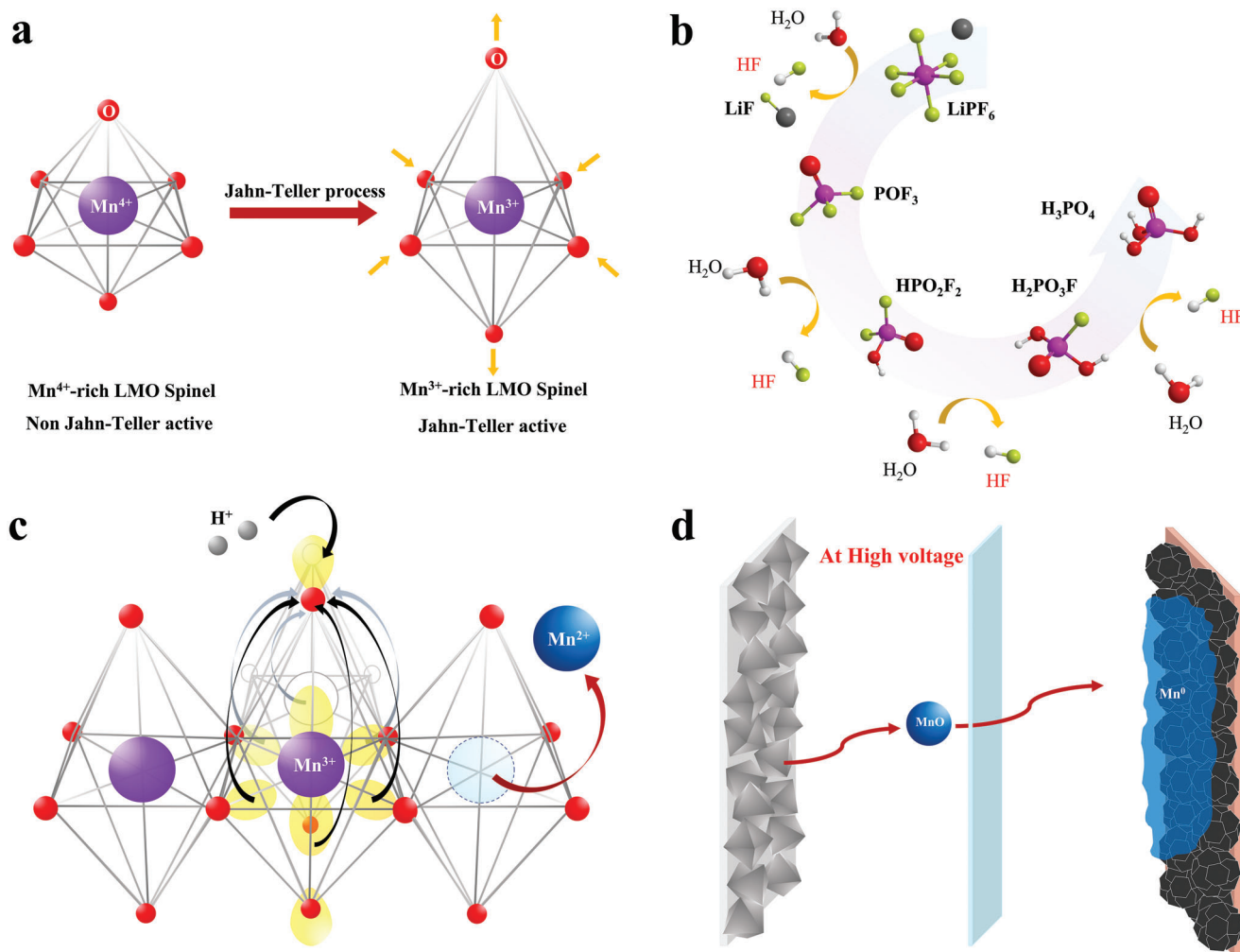small
methods
www.small-methods.com

Figure 3. Schematic representation of the key challenges of spinel cathodes in Li-ion batteries: a) Jahn-Teller distortion, b) reaction of a lithium salt (LiPF$_6$) and trace water to generate HF acid, c) dissolution of Mn^{2+}, and d) the high-voltage state.

crystal structure to change from a cubic LiMn$_2$O$_4$ to a tetragonal Li$_2$Mn$_2$O$_4$. This leads to low symmetry obstructing Li$^+$ diffusion, e$^-$ conduction, and a large anisotropic volume change of around 16%, directly affecting structural damage.[34]

2.2.2. Dissolution of Mn

The Mn dissolution is one of the most important challenges of spinel cathode. Three leading causes of Mn dissolution are Mn^{2+} dissolved in the electrolyte, HF attack of the host material, and the high voltage of charging.

Mn^{2+} Dissolution in an Electrolyte: In the discharge process, as the amount of Mn^{3+} increases, the material surface will show a disproportionation reaction of Mn^{3+}, turning into Mn^{4+} and Mn^{2+} as shown in the following Equation (1)[35]

$$2Mn^{3+} \rightarrow Mn^{4+} + Mn^{2+} \tag{1}$$

The generated Mn^{2+} dissolves into the electrolyte, resulting in a continuous loss of active material.

HF Attack: As illustrated in Figure 3b, the reaction between lithium salt (LiPF$_6$) in the conventional electrolyte of LIBs and trace water produces HF and other acidic substances, according to[36]

$$LiPF_6 + H_2O \rightarrow LiF + 2HF + POF_3 \tag{2}$$

$$POF_3 + H_2O \rightarrow HPO_2F_2 + HF \tag{3}$$

$$HPO_2F_2 + H_2O \rightarrow H_2PO_3F + HF \tag{4}$$

$$H_2PO_3F + H_2O \rightarrow H_3PO_4 + HF \tag{5}$$

Furthermore, Figure 3c illustrates that HF can attack the surface of LMO (LiMn$_2$O$_4$) to produce Mn^{2+}[37]

$$2LiMn_2O_4 + 4H^+ \rightarrow 3\lambda - MnO_2 + Mn^{2+} + 2Li^+ + 2H_2O \tag{6}$$
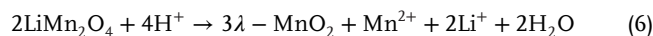
Moreover, HF acid can also attack the surface of LNMO (LiNi$_{0.5}$Mn$_{1.5}$O$_4$), which is another type of spinal material. That
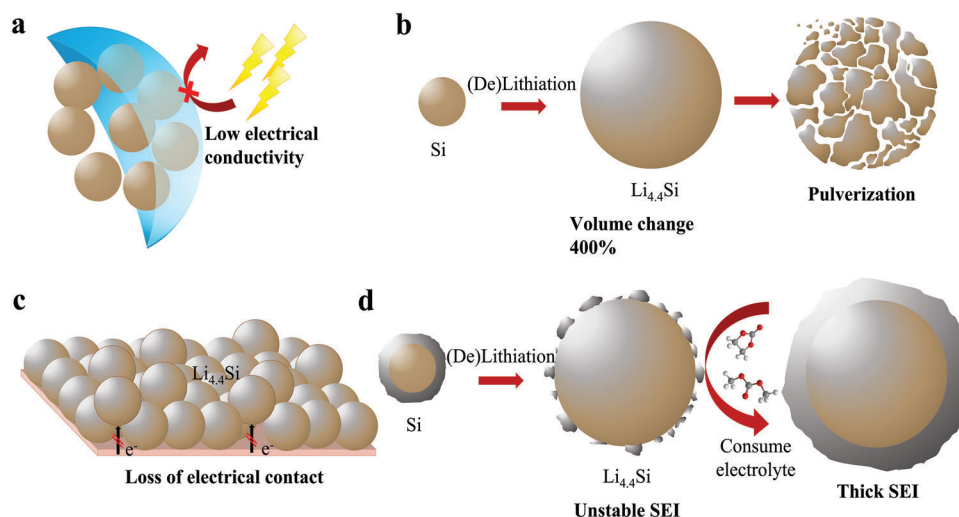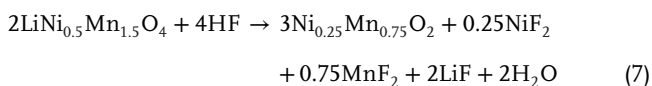
Figure 4. Schematic of the key challenges of Si anodes in Li-ion batteries: a) low electrical conductivity, b) pulverization, c) loss of electrical contact, and d) unstable and thick SEI.

process releases Ni^{2+} and Mn^{2+} to be dissolved in the electrolyte, according to[38]

$$2LiNi_{0.5}Mn_{1.5}O_4 + 4HF \rightarrow 3Ni_{0.25}Mn_{0.75}O_2 + 0.25NiF_2$$
$$+ 0.75MnF_2 + 2LiF + 2H_2O \qquad (7)$$

The dissolved Mn^{2+} can redeposit at the surface of the LMO cathode or migrate to the anode side induced by concentration gradients. Then it precipitates at the anode surface, resulting in slower Li diffusion, declined discharge capacity, and a lower capacity retention of LMO.[39]

High-Voltage State: LNMO cathode can operate at high voltage (5 V vs Li/Li$^+$) with high thermal stability, energy density, and electrochemical stability.[40] Despite its poor cycling performance, the LNMO cathode in LIBs is affected by parasitic reactions resulting from electrolyte degradation at high voltages. The commercial electrolyte is usually composed of $LiPF_6$ in carbonate-base solvents. Such electrolytes tend to be oxidized under high voltage due to a narrow working potential range of 0–4.5 V.[41] The resulting byproducts, such as CO_2, CO, POF_3, $C_2H_5OCOOPF_4$, and OPF_2ORF, can further react with the SEI and lithium metal at the anode side. CO_2 can also react with the anode to generate inactive Li_2CO_3 cover layers at the surface. Byproducts with fluorine elements can generate HF acid, resulting in increased capacity fading of LIBs.

During the final stage of charging, the delithiated structure becomes unstable and loses some of its MnO content, which causes it to transform into a more stable single-phase structure. This leads to greater dissolution of Mn with a higher proportion of Mn^{4+}, resulting in overcharging. According to Equation (8),[42] the phase transition may result in Mn dissolving from spinel at high voltage, according to

$$Li_xMn_2O_4 \rightarrow Li_xMn_{2-\gamma}O_{4-2\gamma} + \gamma MnO_2 \qquad (8)$$
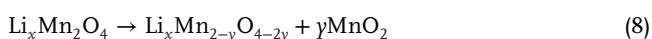
Following the dissolution of the Mn, the MnO (Mn^{2+}) dissolves into the liquid electrolyte and is transferred to the anode[43]

$$\gamma Mn^{2+} + Li_xC_6 \rightarrow \gamma Mn^0 + Li_{x-2\gamma}C_6 + 2\gamma Li^+ \qquad (9)$$
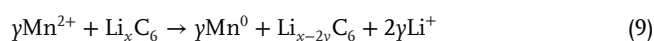
After that, Mn^0 eventually covers the anode surface. This process inhibits the intercalation of lithium in the graphite and raises the anode impedance. Additionally, the deposition of Mn can generate inactive $LiCO_3$ when it reacts with carbonate-base electrolytes and lithium (Figure 3d).[44] As a result of the prolonged cycle life, this mechanism consumes active Li-ions and, consequently, its storage capacity deteriorates dramatically.

3. Anode Challenges in LIBs

3.1. Silicon Anodes

3.1.1. Low Electrical Conductivity

In practical applications of LIBs, the electronic conductivity of Si (particles) is $\approx 10^{-3}$ S·cm^{-1} at room temperature.[45] This property makes it challenging to use these electrode materials due to the low e$^-$ conductivity, Li$^+$ diffusion, and electrochemical kinetics (**Figure 4**a).[46] And from above reasons lead to limitations in the development of total capacity and kinetics of Si anodes.[47]

3.1.2. Material Pulverization

In the process of electrochemical lithiation, silicon can accommodate up to four lithium atoms, making it an alloy anode. However, this mechanism leads to substantial changes in volume due to the significant consumption of lithium. For instance, the transformation from Si to $Li_{4.4}Si$ involves an expansion in volume of about 400%.[48] This repeated expansion and contraction during lithium insertion and extraction creates significant stress on the
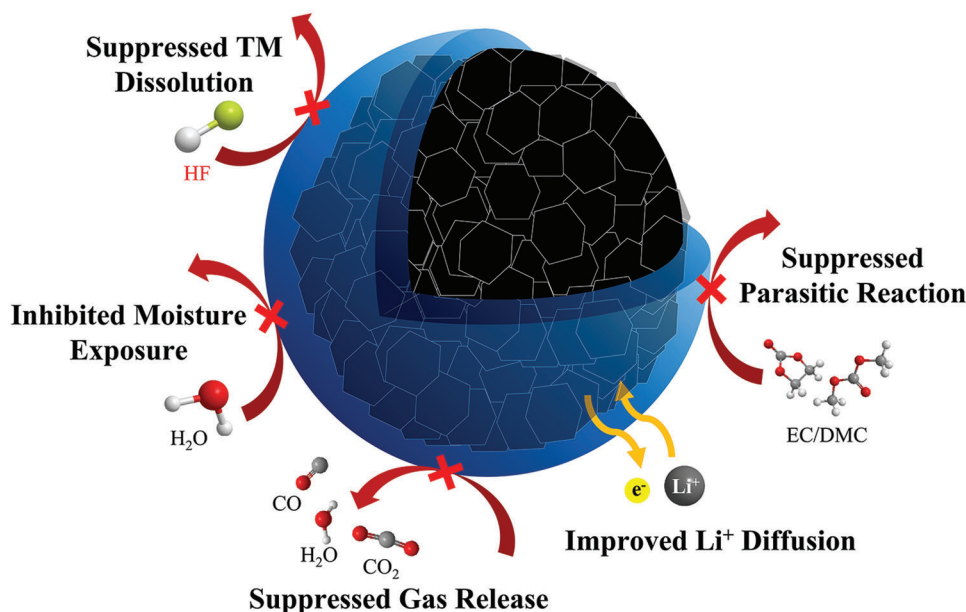
**ADVANCED
SCIENCE NEWS**

www.advancedsciencenews.com

**small
methods**

www.small-methods.com

Figure 5. Schematic illustration of the core–shell strategy for layered and spinel cathodes in LIBs, which prevents direct contact with the electrolyte, reduces gas release reactions, parasitic reactions, and the dissolution of transition metals due to HF acid, and improves the Li$^+$ diffusion coefficient.

silicon particles in particular, shrinkage occurs during delithiation. That can cause cracking and pulverization of Si, as illustrated in Figure 4b.[49] As shown in Figure 4c, this process leads to a loss of electrical contact between the active powder particles and the current collector and, consequently, to a considerable loss of active material, which causes low-capacity stability and rapid capacity decay.[50]

3.1.3. Unstable SEI

Along with pulverization, SEI is another serious problem caused by large volumetric changes during electrochemical cycling.[51] Due to the reduction of the organic electrolyte, the SEI layer covers the anode surface when the anode potential is less than ≈1 V versus Li/Li$^+$. In order to prevent other side reactions and the cycle-life performance of LIBs from dropping continuously, the SEI layer should be dense and stable, electronically insulating but ionically conducting.[52] As the volume of silicon steadily increases during the lithiation process, the formed SEI becomes cracked, exposing the electrode surface to bring the fresh Si surface in contact with the electrolyte. That results in the continuous growth of the SEI.[53] This unstable SEI consumes more electrolyte molecules and lithium ions (Figure 4d). This process increases the internal resistance of thick SEI, resulting in low coulombic efficiency, low electronic conductivity, and electrode degradation.[54]

4. Solving Cathode Challenges by Core–Shell Strategies

Various strategies have been developed to optimize the benefits and mitigate the limitations of layered and spinel cathode materials in LIBs. Two outstanding approaches are the design of core–shell structures and metal ion doping:

1) Core–shell structure design: layered or spinel cathode materials are coated by a protective shell made of an electronically and structurally stable cathode material to form a core–shell structure. This design prevents direct contact with the electrolyte, reducing gas release reactions, parasitic reactions, and the dissolution of transition metals due to HF acid. The core–shell approach also offers several benefits, including enhanced storage properties, simplified electron transfer and conductivity, and an increased Li$^+$ diffusion coefficient.[55] These improvements result in better electrochemical performance and increased battery stability (**Figure 5**).

2) Metal ion doping design: the introduction of metal ion doping into layered and spinel cathode materials offers several advantages, such as improved structural stability, increased electronic conductivity, higher capacity, enhanced safety, and greater cost-effectiveness. To fully realize these benefits, researchers must optimize factors such as dopant selection, doping methods, and treatment parameters.[56] As a result, metal ion doping remains a dynamic area of research in the pursuit of maximizing electrochemical performance in LIBs.

4.1. Layered Cathodes

4.1.1. LCO (LiCoO$_2$)

Coating of LCO with a shell thickness of 100 to 1000 Å as a core–shell structure effectively prevents direct contact with carbonate-base electrolytes, suppresses phase transitions, decreases cation disorder, and improves the structural stability.[57] As a result, the electrochemical performance is significantly enhanced. That relates to reversible capacity, cyclic behavior, and rate capability.

LCO coatings with inactive metal oxide is well known in the literature, including Al$_2$O$_3$,[58] MgO,[59] SnO$_2$,[60] ZnO,[61] Fe$_2$O$_3$,[62]
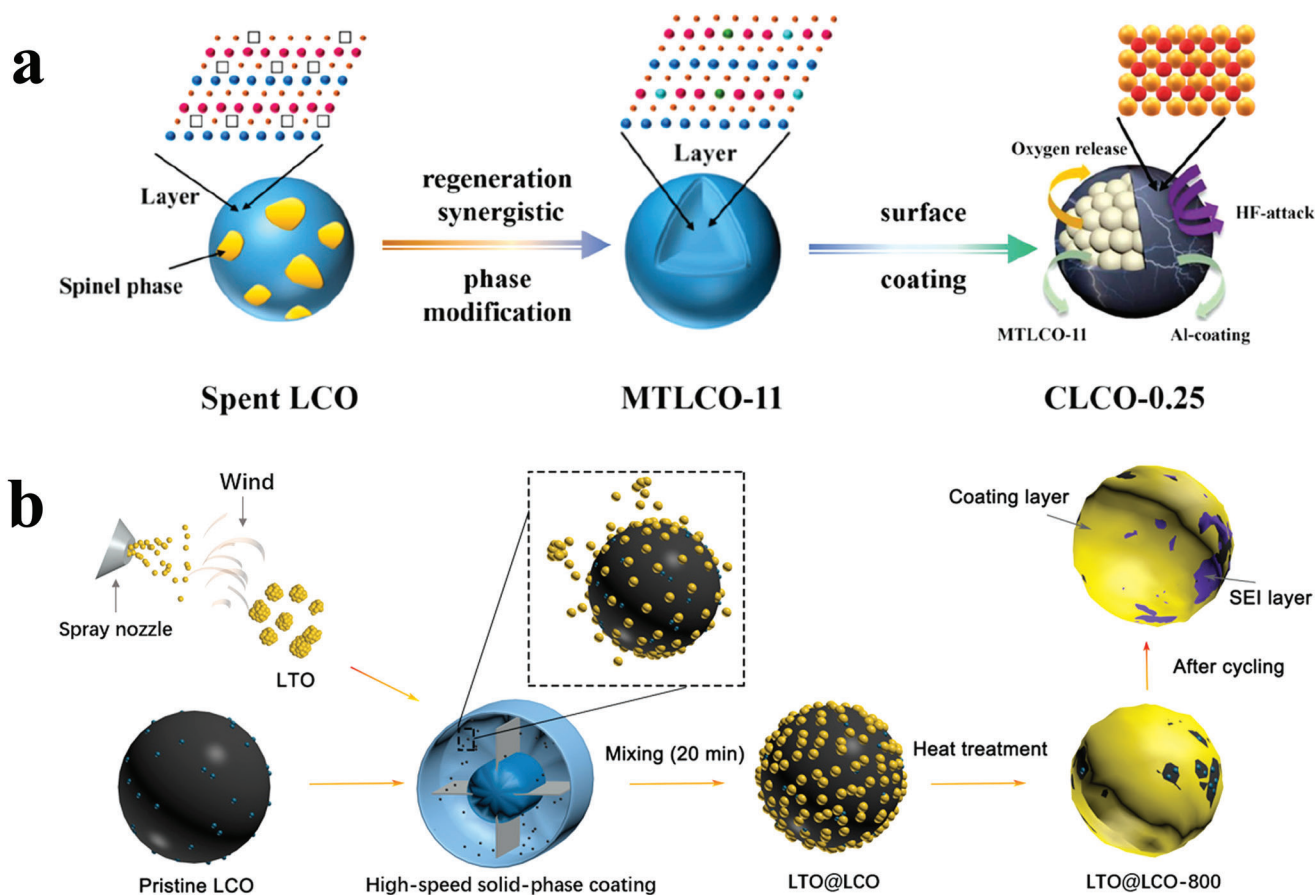
Figure 6. a) Schematic diagram of coating MTLCO-11 and CLCO-0.25 on a LCO cathode material. Reproduced with permission.[66] Copyright 2022, American Chemical Society. b) Schematic diagram of high-rate solid phase coating process of LTO@LCO cathode material. Reproduced with permission.[69] Copyright 2020, American Chemical Society.

ZrO_2,[63] and TiO_2.[64] The insulator coatings can help to reduce the chemical or parasitic reactions during the charge and discharge cycling process and at the high voltage during charging. However, the inert metal oxide layer not only can improve the capacity of LIBs at higher cut-off voltages but can also influence the high-rate capability by improving the Li^+ conductivity across the interface of the cathode and electrolyte.[65] Another unique method was recently presented by the group of Zhao. Direct regeneration of consumed LCO materials with Al-compounds coating suppressed the interface side reaction at a high cutoff voltage, as shown in **Figure 6**a.[66] The coating layers, composed of Al_2O_3 and $LiCo_{1-y}Al_yO_z$ solid solution, at the surface of synergistically regenerated materials exhibit high cycling stability. That is advantageous for suppressing side reactions and preventing corrosion at the interface or attacking the bulk phase caused by harmful substances, such as HF, in the electrolyte during battery operation.

To overcome the weaknesses of metal oxides that cannot increase the capacitance and are suffering from low Li^+ conductivities, Li-containing compounds with high ionic conductivity are alternative coating materials. The examples are, $LiAlO_2$,[67] $LiNbO_3$,[68] $Li_4Ti_5O_{12}$,[69] $LiAlF_4$,[70] $Li_{1.6}Mg_{1.6}Sn_{2.8}O_8$,[71] $LiPON$,[72] and $Li_7La_3Zr_2O_{12}$.[73] A quick and simple scalable high-rate solid phase coating technique was devised by Wang

et al. in their study to encapsulate LCO in a thin $Li_4Ti_5O_{12}$ (LTO) layer.[69] LTO has a fast Li^+ diffusivity of 1×10^{-6} cm^2·s^{-1} and outstanding structure stability even at high voltage.[74] According to Figure 6b, a considerable number of nanosized LTO particles created using the sand milling technique are attached to the surface of the LCO microspheres by a high-rate solid-phase coating. Heat processing results in encapsulating the LCO micro-spheres within a consistent, continuous LTO layers. Due to the suppression of bulk phase transition and surface side reactions, the cycling stability of the cathode materials improved when tested at high voltages while being armored within such continuous and robust LTO layers.

On the other hand, carbon coatings can improve the cycling stability and rate capability of LCO significantly because it acts as a transport medium and increases the electronic conductivity of cathodes. Also, these coatings physically prevent side reactions between LCO and the carbonate-base electrolytes.[75] The research by Lin et al. shows that the innovative synthetic method for in situ synthesis of a carbon coating LCO heterostructure derived from a metal-organic framework (MOF) was elevated-temperature solid-state annealing.[76] A simple microwave-assisted approach was used to synthesize a zeolitic imidazolate framework (ZIF67) efficiently. The ZIF67 powder was first prepared and then combined with lithium carbonate

**ADVANCED
SCIENCE NEWS**

www.advancedsciencenews.com

**small
methods**

www.small-methods.com

for high-temperature sintering lithiation. This transformed the ZIF67 nanopolyhedron into an LCO particle, which was further annealed using a solid-state method at elevated temperatures. To achieve complete conversion and produce a series of core–shell LCO@C particles with high crystallinity, they were heated under nitrogen at 600, 700, and 800 °C. The carbon-coated layers on these particles prevent direct contact between the LCO bulk and electrolyte, improving electrochemical conductivity and reducing structural distortion caused by strain during lithium insertion and extraction. This enhances long-term cycling stability and improves the electrochemical performance, particularly at high cut-off voltages of 4.5 V.

Overall, an ideal core–shell coating strategy allows it to create a high-voltage, chemically, and electrochemically stable, low-resistant surface layer and boost the electrical conductivity for LCO. A homogeneous and conformal core–shell is also necessary to homogenize the lithium flow throughout the (dis)charge process. This property is particularly important for LCO when cycled at high voltages, as the structure quickly collapses at high delithiated states, and more Li^+ is extracted from the LCO structure. It is caused by inhomogeneous (de)lithiation may accelerate this process.

4.1.2. Ni-rich NMC ($LiNi_{1-x-y}Mn_yCo_xO_2$) and NCA ($LiNi_{1-x-y}Co_yAl_xO_2$)

The idea of adopting a core–shell strategy is to cover the highly reactive Ni-rich cathode material with an outer sphere of less reactive material.[77] This structure enables the combination of the shell outstanding stability with a core of high electrochemical performance.[32a,78] The core–shell strategy has proven to be an effective method to protect the reactive Ni^{4+} of Ni-rich cathode material from unfavorable side reactions. In order to both boost the surface structural and thermal stability, the coating layer creates a physical barrier between the active material and electrolyte, especially in the highly lithiated states.[79] Additionally, these coatings can protect Ni-rich cathode materials effectively against corrosion by HF, formed by hydrolysis of $LiPF_6$. The scavenger of acidic HF leads to the dissolution of transition metal ions out of the surface of the active material, causing lattice damage and continuous loss of active material.[55c,e,80] During (de)lithiation, the coating layer could help to suppress the phase transition of cathodes from a layered structure to a rock-salt phase because the presence of the physical layer can prevent the loss of oxygen from the lattice by preventing the reaction between reactive Ni^{4+} and electrolyte.[81] Although core–shell materials cannot directly suppress the intergranular and intragranular cracking, it reduces effects of lattice expansion along the c-axis and shrinkage along the a-axis and b-axis. However, the core–shell morphology can avoid parasitic reactions caused by the interaction between the fresh surface (reactive surface) formed by cracking and electrolyte.[82] Moreover, Ni-rich cathode materials tend to form surface impurities under ambient conditions, which causes to lose capacity more quickly during cycling, become higher impedance, and generate gas. Another beneficial side effect of a stable coating layer is the improved storage property of Ni-rich cathode materials by protecting of CO_2 and H_2O from the ambient condition.[83]

On the other hand, changing the chemical properties of the electrode/electrolyte interface can increase the raw material capacity and simplify e^- transfer by introducing coating materials with superior ionic and electronic conductivity.[84] Finally, core–shell structure increases the ability of materials to withstand mechanical deterioration. The cathode material particles shatter under the high stresses experienced during the electrode calendaring process.[85] The mechanically induced materials capacity degradation is suppressed, and the integrity of the particles during cycling is improved when the material has a mechanically-strong protective layer created by the core–shell strategy.

Metal oxide is one of the most common coating materials demonstrated via testing to be highly stable under exertive conditions, such as windows with extended operating potential voltage and higher elevated cycling temperatures due to inert material with properties that are virtually nonreactive to electrolytes and prevent corrosion caused by HF scavengers.[86] Surface coating of Ni-rich (NMC and NCA) with an inert material can be divided into the following categories: metal oxide (Al_2O_3,[87] TiO_2,[88] ZnO,[56a,89] V_2O_5,[90] MgO,[91] ZrO_2,[92] SiO_2,[93] Co_3O_4,[89,94] CeO_2[95]), metal fluoride (LiF,[96] AlF_3,[97] CaF_2,[98] FeF_3,[99] MgF_2[100]) and metal phosphate ($AlPO_4$,[101] Li_3PO_4,[102] $MnPO_4$,[103] $LaPO_4$,[104] $FePO_4$,[101a,105] $Ni_3(PO_4)_2$[106]). **Figure 7**a illustrates the results of a thorough investigation of the ideal coating and its impact on the electrochemical performance and safety of the NCM811 cathode material by Ramakrishna and colleagues.[107] They developed a novel TiO_2 nanolayer using a simple wet chemical technique. The prepared coating effectively reduced the surface area in contact between the cathode and electrolyte to reduce transition metal dissolution. It also prevented unfavorable side effects, including HF attacks. As a result, the coated NMC811 with TiO_2 showed significantly improved cycle performance and rate capability. The exothermic peak of the NCM811 cathode material was also moved to higher temperatures. The cathode phase change during heating was postponed by surface modification using TiO_2 nanoparticles. This outcome demonstrates the value of TiO_2 coating in improving the performance and safety of NCM811 cathode materials in LIBs. Moreover, Ming and co-workers have developed a unique organic ligand coordination complex to stabilize the metal phosphate in a non-aqueous solution and then use it to modify NCM with $AlPO_4$. The schematic representation of the coating process and the various chemical compositions of the coating layer are shown in Figure 7b.[101b] Previous to forming an amorphous $AlPO_4$ layer after sintering, the $AlPO_4$-based solution can evenly disperse over the NCM particles at the molecular level and create a thin film after drying. This strategy addresses the issue of nonuniform coating in the existing precipitation process. It creates a new path to molecularly controllable ultra-thin surface modification. Consequently, the performance of NCMs in high-voltage situations has significantly improved, including their stability and reliability, as well as their cycling and cycling capabilities.

Nevertheless, inert materials have the disadvantage of having low conductivity for ions and electrons. That hinders the cell performance at fast (dis)charge rates and slightly increases the irreversible capacity of the Ni-rich cathode materials. Conductive polymers (polypyrrole (PPy),[108] poly(3,4-ethylenedioxythiophene),[109] polyaniline (PANI),[110] and
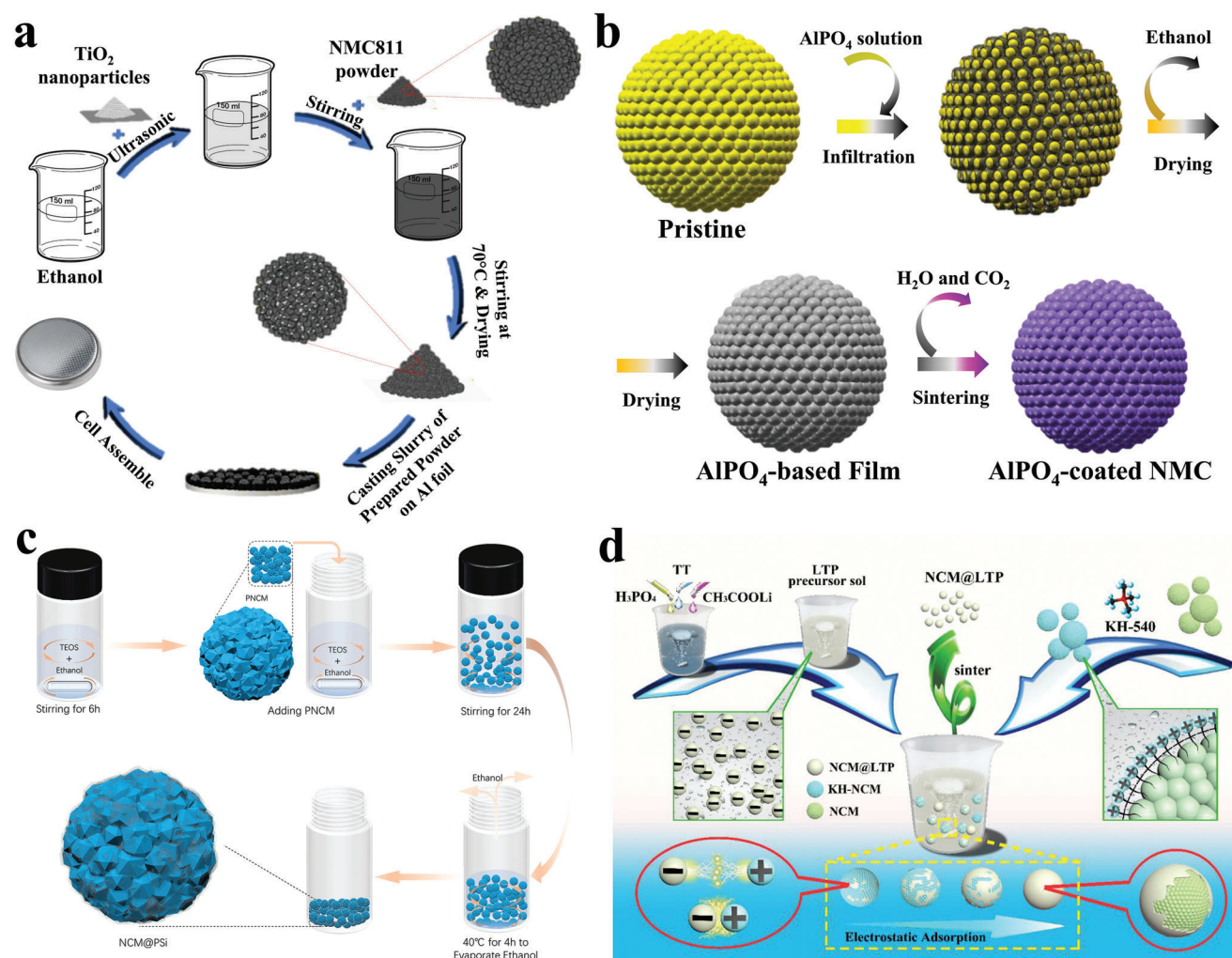
Figure 7. a) Schematic illustration of applying an TiO_2 coating on a NCM811 cathode powder and cell assembling with the modified cathode. Reproduced with permission.[107] Copyright 2021, American Chemical Society. b) Schematic illustration of surface modification of $AlPO_4$ for NCM. Reproduced with permission.[101b] Copyright 2019, American Chemical Society. c) Schematic illustration of coating process of PNCM via polysiloxane. Reproduced with permission.[112] Copyright 2021, American Chemical Society. d) Schematic illustration of preparation and charge attraction effect on NCM@LTP. Reproduced with permission.[126] Copyright 2019, Elsevier.

3,4-ethylenedioxythiazide (PEDOT)[109]) have attracted much attention from researchers as coating materials, due to their high electronic conductivity, stability elasticity, electrochemical activity, and low cost. These polymers could simultaneously stabilize and buffer the volume change of cathodes during cycling. Additionally, coating layers of conductive polymers may enhance the rate capability and charge-transfer process at the surface of Ni-rich cathodes.[111] Li et al. demonstrated that coating the NCM cathode with polysiloxane via a wet chemical process may prevent interfacial side reactions by removing the HF in the electrolyte and the H_2O on the NCM, as shown in Figure 7c.[112] This method guarantees stable electrochemical cell performance. The polysiloxane coating prevents adverse effects on the NCM, which helps increase the structural stability of the NCM cathode. At the same time, the rate performance of the NMC@PSi is better than that of PNCM (pristine NCM) at various rates. All these improvements are attributed to the polysiloxane coating layer.

Electrically conductive carbon materials are another example of a coating material with improved electronic conductivity compared to an inert coating material (metal oxide, metal fluoride, and metal phosphate).[113] Highly conductive carbon material can be coated on a surface to increase e⁻ transfer through the interface of the cathode material particles, accelerating the process of heterogeneous charge transfer on a Ni-rich surface. The coating can also add additional pathways for e⁻ to travel between the cathode material particles and between the cathode material particles and the current collector.[114] Additionally, this material shows faster Li⁺ diffusivity and less gas generation at high charging potentials voltages resulting in higher capacity and cycling stability, especially at high rates.[115]

Unfortunately, most of the coating materials for Ni-rich cathode have low ionic and electronic conductivity, which is detrimental to rate performance and even reversible capacity. Therefore, Li-containing inorganic oxides, as a prominent coating material, are introduced, such as $LiTi_2(PO_4)_3$,[116] Li_3PO_4,[117] Li_2SiO_3,[118]

**ADVANCED
SCIENCE NEWS**

www.advancedsciencenews.com

**small
methods**

www.small-methods.com

Li_2ZrO_3,[119] $LiAlO_2$,[120] Li_2CO_3,[121] Li_2TiO_3,[122] Li_2MnO_3,[123] and $LiCoO_2$.[124] Li-containing inorganic oxides can improve the rate performance of Ni-rich cathode materials and facilitate the diffusion of Li^+ at the interface between the active material and electrolyte. Additionally, they can act as a barrier to minimize unwanted side reactions. When tiny particles of these oxides are attached to the surface, they preferentially react with the HF present in the electrolyte.[125] Thus, the coating layer is successfully maintained throughout the cycle lifetime, resulting in a stable interface with low impedance. Tian and co-workers have presented a novel approach for synthesizing NCM@LTP cathode material (Figure 7d).[126] The self-assembled electrostatic charge attraction between LTP (negative charge) and NMC@KH-540 (positive charge) is maintained, facilitating uniform NCM surface coatings. As a superior solid electrolyte, NASICON-type $LiTi_2(PO4)_3$ (LTP) exhibits ultrahigh Li^+ conductivity in the group of $Li_xM_2(PO_4)_3$. Electrochemical experiments have also revealed that coating with LTP increases cycling stability at high cut-off voltage while simultaneously improving ionic transport. Hopefully, the work by Tian will provide novel insights for future coating developments.

4.2. Spinel Cathodes

4.2.1. LMO ($LiMn_2O_4$)

The synthesis of morphologies,[127] metal ion doping,[128] and surface coating have all been examined as potential solutions to improve LMO material. Despite efforts to control the synthesis of morphologies and introduce metal–ion doping, it is still not possible to completely prevent the dissolution of Mn due to HF attack at the interface between the electrode and electrolyte during charging and discharging. On the other hand, the coating layer is a practical and controllable approach that can:

1) Prevent direct contact between the active cathode material and electrolyte, reducing Mn dissolution.
2) Minimize the Mn deposition on the anode surface, resulting in a slower impedance increase.
3) Suppress phase transitions and dendrite formation.
4) Enhance the structural stability at high voltage.
5) Decrease the disorder of cations in crystal sites.
6) Increase the electronic and ionic conductivity of the electrodes.[129]

The majority of efforts have been focused on covering the surface of the core–shell structure with various inert shell materials, such as metal oxide (MgO,[130] Mn_2O_3,[131] CeO_2,[132] ZrO_2,[133] Al_2O_3,[134] TiO_2,[135] SiO_2[136]), fluorides (LaF_3,[137] MgF_2,[138] AlF_3,[139] and FeF_3[140]), and phosphates (YPO_4,[141] $AlPO_4$,[142] $FePO_4$,[143] and $LaPO_4$[144]), to solve these challenges. These inert layers act as HF scavengers that reduce Mn dissolution and side reactions by preventing direct contact between the active material and the electrolytes. The resultant core–shell constructions with inert shells have also been investigated for enhancing cycling or thermostability at high temperatures. The Tu group also demonstrates the co-existence of an Al-diffusion surface layer and an oxide coating at the surface.[145] That was carried out to avoid

surface Jahn-Teller distortion and delay Mn dissolving, retaining good structural stability and electrical contact. In the study by Yu and co-workers, TiO_2 nanocoating is deposited to an LMO electrode using the atomic layer deposition (ALD) technique, as shown in **Figure 8**a. This highly homogeneous, conform, and dense amorphous coating layer is directly coated at the cathode electrode to maintain electrical conductivity. The polarization and self-discharge of this coated material are low. The highly conformal and ultrathin TiO_2 coating improves the kinetics of Li^+ diffusion. It stabilizes the electrode and electrolyte interface resulting in increased electrochemical performance.[146]

Metal nanoparticles are another choice for coating. This coating can improve electrical contact between particles to direct e^- toward the current collector and improve Li^+ diffusion pathways of the cathode material. In Figure 8b, Julien and co-workers exhibit LMO cathode material coated with Ag via a co-precipitation synthesis process. The coating state forms nanospheres covering the surface of LMO with major Ag particles and minor AgO. The synergistic effect of Ag and AgO can enhance specific surface area up to 4.1 $m^2 \cdot g^{-1}$ and raise mesoporosity, which might promote accessible diffusion pathways for Li^+ to LMO particles. Moreover, a small amount of Ag can reduce the thickness of SEI. The presence of the superficial conductive layer increases the interparticle electrical contact of LMO. It creates a thin insulating AgO layer that shields against side reactions. This strategy increases the rate capability and cycling life of the LMO cathode.[147]

Besides, limited ionic and electronic conductivity of inert coating materials lead to a restriction of the electron transfer kinetics. Amorphous carbon,[148] graphene oxide,[149] rGO,[150] and CNTs[151] are examples of several forms of carbon coatings that have been investigated to overcome the weaknesses of inert coating materials.[152] Moreover, the advantages of carbon-based surface coating are as follows: 1) Excellent electrochemical and chemical stability. Carbon has great electrochemical stability and good resistance to corrosion from HF due to the reduce interaction between the electrolyte and electrode, which reduces the Mn dissolution.[153] Additionally, the cathode materials might be protected from oxygen and moisture in the air by carbon, which cannot be easily oxidized. 2) Carbon possesses distinct physical properties such as anisotropic conductivity, low density, high mechanical strength, and structural flexibility.[154] 3) Carbon exhibits outstanding electrical conductivity, which can enhance the flow of e^- through the coated shell, resulting in better utilization of the active material.[155] 4) The 3D structure of the carbon layer has the potential to prevent the collapse of the cathode material's structure, thereby reducing the formation of cracks in the particles due to structural changes.[156] 5) Low cost and abundance.

In addition, a novel nitrogen-containing carbon (N–C) coating developed by Lee and colleagues significantly improved the cyclability and discharge capacity of LMO cathodes. Easy coating of N–C material onto the LMO resulted in an ordered surface encapsulation promoted fast Li^+ diffusion while preserving the structure of the LMO core material. The coating reduced Mn dissolution by preventing direct contact between the electrode and electrolyte. This coating process promises to produce a high-performance cathode material for LIBs, as evidenced by observed EIS and cycling characteristics (Figure 8c).[153]

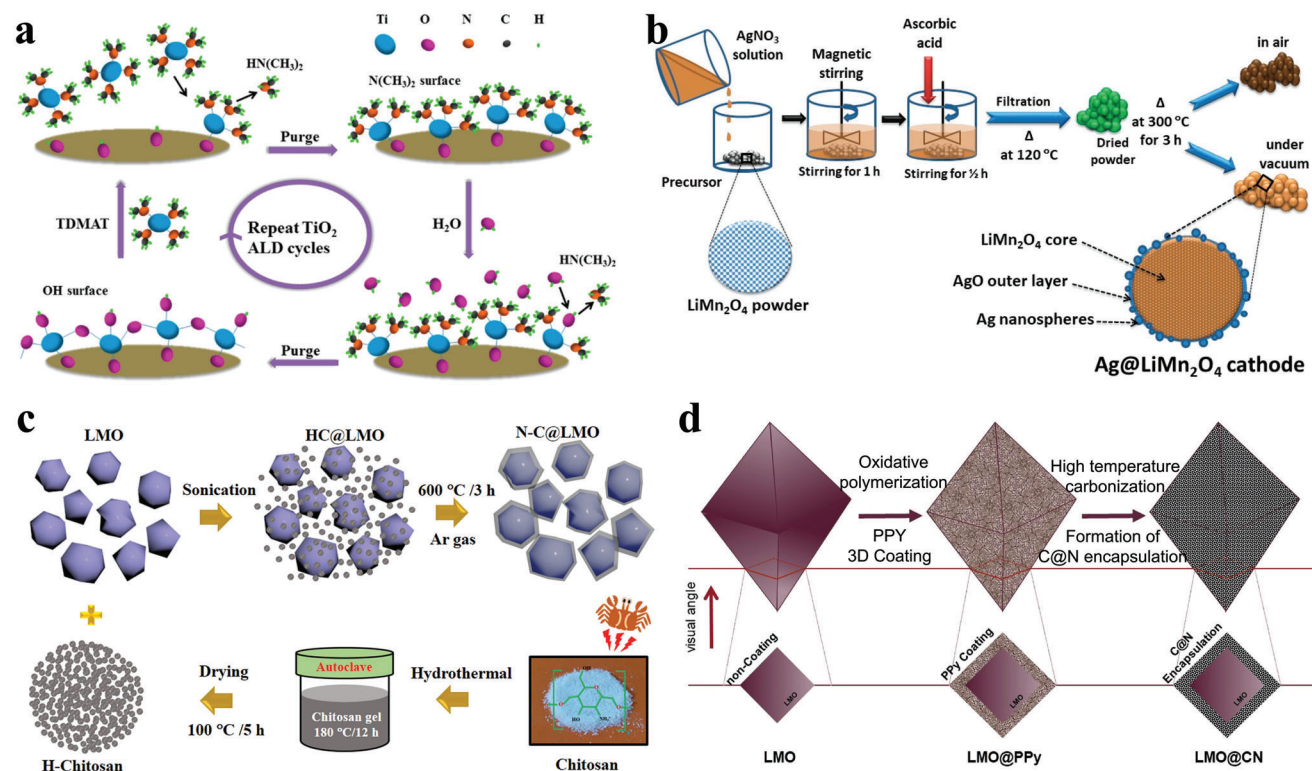Another example of conductive polymer coatings is polypyrrole (PPy)[157] and polyacrylonitrile (PAN).[158] Conducting

**ADVANCED
SCIENCE NEWS**

www.advancedsciencenews.com

**small
methods**

www.small-methods.com

Figure 8. a) Schematic illustration of TiO_2 layer deposited on LMO electrode surface via ALD. Reproduced with permission.[146] Copyright 2018, American Chemical Society. b) Schematic illustration of the Ag coating process of LMO nanoparticles. Reproduced with permission.[147] Copyright 2020, MDPI. c) Schematic illustration of preparation of N–C@LMO via ultrasonication and calcination process. Reproduced with permission.[153] Copyright 2016, Springer Nature. d) Schematic illustration of three-dimensional *in-situ* polymerization and high-temperature annealing of PPy on a LMO surface. Reproduced with permission.[160] Copyright 2022, Elsevier.

polymers can improve the kinetic performance of LMO and reduce the charge-transfer resistance of Li^+ at the interface of the electrolyte and electrodes.[159] Figure 8d illustrates the procedure used by Yuan et al. to create a unique carbon-encapsulated LMO membrane electrode created by growing the PPy coating in situ after high-temperature annealing. The coating layer served as a conductive layer to improve both electronic and ionic transport and as a buffer layer to prevent crystal volume collapse and dissolution of Mn. This core–shell material demonstrated a faster Li^+ electrosorption rate, higher Li^+ diffusivity, and better stability than the LMO electrode.[160]

4.2.2. LNMO ($LiNi_{0.5}Mn_{1.5}O_4$)

Numerous techniques have been studied to address these issues, including coatings,[161] cation doping,[162] and electrolyte additives.[163] Among them, the core–shell structure has been recognized as an excellent method for preventing direct contact between the LNMO electrode and electrolyte by creating a completely protective layer at the LNMO surface, thereby suppressing the undesirable side reactions. Additionally, this technique can improve the structural stability at high voltages, the electrode and electrolyte surface stability, the ionic or electronic conductivity, inhibit the phase transition, and reduce cation disorder at crystal

sites.[164] As a result, it can significantly improve the electrochemical performance of LIBs.

One potential approach to overcome these shortcomings of LNMO is a core–shell structure with metal oxides (Al_2O_3,[161a,165] TiO_2,[166] ZrO_2,[167] CeO_2,[168] ZnO,[169] MgO,[170] V_2O_5,[171] SiO_2,[172] and MoO_3[173]) and phosphates ($AlPO_4$,[174] $FePO_4$,[167] and Li_3PO_4[175]). From literature, inactive shell materials have been adopted to address the issues of electrolyte oxidation and dissolution of transition metals due to their electrically nonconductive and electrochemically stable properties and enhanced electrochemical performance at both room and elevated temperatures. These inert layers can provide a protective barrier to avoid direct contact of the particle surface with the electrolyte at high voltages and also eliminate the harmful HF acid molecules produced in the electrolyte, resulting in an improvement of the cycling performance of spinel LNMO cathodes. The results of using ALD to produce ultrathin Al_2O_3 coatings on LNMO particles are reported by Kim et al. The core–shell showed considerably reduced self-discharge and transition metal dissolution in combination with significantly improved coulombic efficiency, cycle retention, and rate capability. This discrepancy results from the ALD-deposited Al_2O_3 coatings, inhibiting side reactions at high voltages. In addition, the SEI layers on uncoated and Al_2O_3-coated LNMO particles after cycling performance are represented schematically in **Figure 9**a. The Al_2O_3-coated LNMO particles

**ADVANCED
SCIENCE NEWS**

www.advancedsciencenews.com
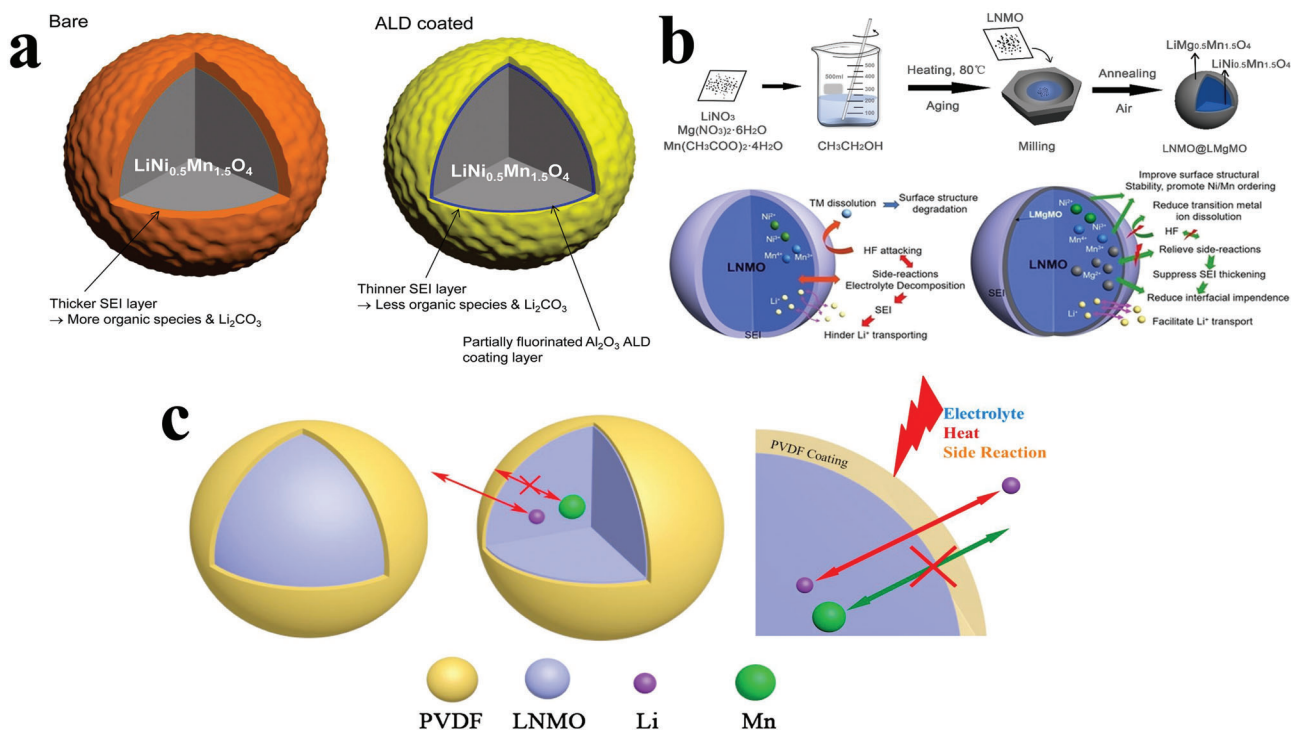
**small
methods**

www.small-methods.com

Figure 9. a) Schematic illustration of a bare and Al_2O_3-coated (ALD) LNMO electrodes after (dis)charge cycling, showing different features in the SEI layers Reproduced with permission.[176] Copyright 2015, Elsevier. b) Schematic illustration of the advantages of the integrated surface coating to stabilize the surface of the LNMO particle with $LiMg_{0.5}Mn_{1.5}O_4$ (LMgMO). Reproduced with permission.[189] Copyright 2020, Wiley-VCH. c) Schematic illustration of PVDF coating at a LNMO surface and its role in protecting LNMO and suppressing undesired interfacial reactions and Mn dissolution. Reproduced with permission.[193] Copyright 2018, Elsevier.

have substantially thinner SEI layers and have fewer organic species than the bare LNMO particles.[176]

Metal fluoride (LiF,[177] MgF_2,[178] CeF_4,[179] and AlF_3[180]) is also an effective coating material for LNMO cathodes because 1) it suppresses the Mn dissolution of active materials via a physical protecting layer, 2) inhibits the fast SEI growth during (dis)charging, 3) provides surface stabilization due to a strong ionic bonding with high ionic conductivity and (electro)chemical stability and insolubility that significantly improves Li^+ transport during the cycling process.[181] As a result, the structural stability, interface stability, cycling capability, and thermal stability of LNMO are improved significantly.

Nevertheless, these conventional coating layers, including oxides and fluorides, are often not electrochemically active and have poor electronic and/or ionic conductivity. The inert coating materials are insulators for Li^+ conduction and could prevent Li^+ migration.[182] Therefore, utilizing core–shell materials composed of Li-containing inorganic oxides such as $LiNiPO_4$,[183] Li_2ZrO_3,[184] $Li_{0.33}La_{0.56}TiO_3$,[161c] $LiAlSiO_4$,[185] and $LiNbO_3$[186] as the shell material is recommended as it serves as both a protective layer and an efficient electrical and ionic conductor. The same crystal structure exists in both the core and shell, allowing coherent connections at the interface. Additionally, Li^+ diffusion channels present at the intersection of the two materials exhibit exceptional thermodynamic stability.[187] Also, some Li-containing inorganic oxides may absorb HF acid through aluminosilicates with hierarchical porosity, leading to increased cycle performance and thermal stability of the LNMO

cathode.[188] LNMO@LMgMO, synthesized via a sol-gel self-combustion method, was introduced by Xie and co-workers as cathode materials for LIBs that can endure both high voltages and temperatures. The synergistic effect improves the Ni/Mn ordering and crystal stability of LNMO. LMgMO ($LiMg_{0.5}Mn_{1.5}O_4$) gives LNMO a Li^+ transport window for enhancing Li^+ diffusion. The physical protective layer that LMgMO creates at the surface of LNMO also reduces the growth of SEI film, minimizes surface side-reactions, and impedance growth. In addition, as shown in Figure 9b, LMgMO could effectively prevent HF attack at the LNMO surface, decrease transition metal dissolution, and enhance material reversibility.[189]

Unfortunately, the Li^+ diffusivity does not change significantly due to the poor conductivity of these inorganic materials. These coatings potentially reduce the high-rate performance of the composite compared to the case when the coating is absent. Conductive carbon coatings have been mentioned as alternative material. However, it is still challenging to apply to LNMO because Mn^{4+} in LNMO is quickly reduced by carbon to Mn^{3+}, which requires a reducing atmosphere for the carbon source to carbonize at high temperatures.[190] Identifying another unique coating substance that may serve as a protective and conductive layer for LNMO is crucial in this regard. Conducting polymers (PEDOT,[191] polyimide (PI),[192] polyvinylidene fluoride (PVDF),[193] and PPy[194]) has been considered a possible addition in recent years to help LIBs operate better during cycling also at higher rates. The utilization of a conducting polymer layer serves to enhance ion conductivity and inhibit unintended surface reactions on LNMO.
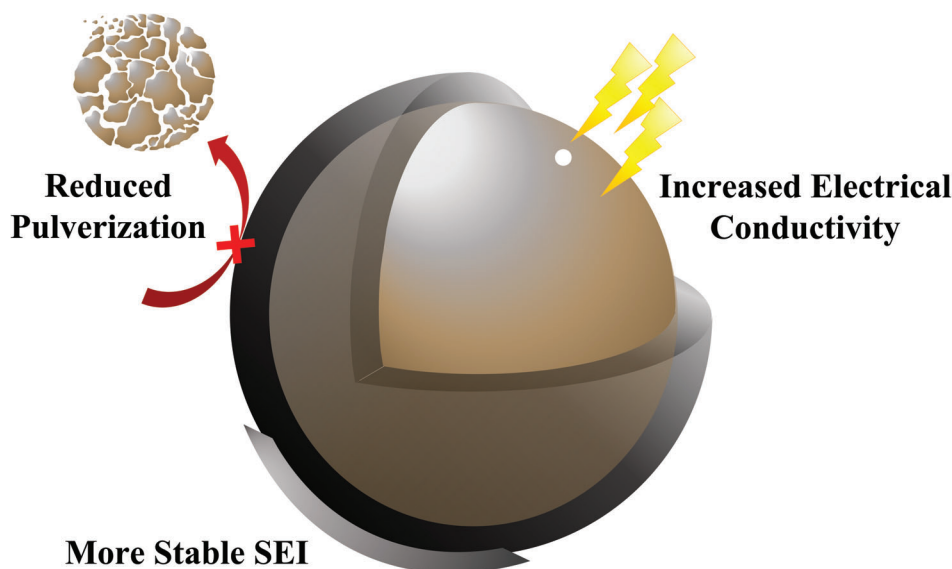
Figure 10. Schematic illustration of the core–shell strategy for silicon anodes in LIBs, which mitigates pulverization, stabilizes the SEI, and improves electrical conductivity.

This effectively minimizes dissolution of Mn during the charge and discharge process. Gao et al. produced the conductive PPy-coated LNMO applied as cathode materials in LIBs. They showed excellent electrochemical performance at high potentials and during long-term cycling due to the fact that 1) PPy acts as a conductive polymer that can improve the conductivity and reduce the charge transfer resistance of bare LNMO, 2) the PPy layer can suppress transition metal dissolution into the electrolyte and 3) PPy protection layer can prevent undesirable reactions between the cathode electrode and electrolyte at the surface of the active material at high temperatures, which results in significantly enhancing the coulombic efficiency.[194a] The Huang group[193] presented a method where PVDF is deposited on the surface of the particles using a liquid coating technique to support the 5 V spinel LNMO cathode in organic electrolyte. PVDF is electrochemically inert and oxidation resistant. Researchers have discovered that the continuous and completely covered PVDF layer effectively reduces electrolyte decomposition at the electrode-electrolyte interface and protects LNMO from corrosion by the organic electrolyte, particularly under high voltage and high-temperature conditions. The electrochemically inactive surface coating essentially prevents the formation of an SEI film, and the impedance rise of the electrode during cycling is decreased. During prolonged electrochemical cycling, the PVDF wrapping layer prevents Mn from dissolving into the electrolyte. Consequently, the 5 V spinel LNMO cathode is successfully stabilized in the organic electrolyte, and as shown in Figure 9c, its overall electrochemical performance is significantly improved.

5. Solving Anode Challenges by Core–Shell Strategies

5.1. Silicon Anodes

Various techniques have been developed to illustrate the advantages and minimize the drawbacks of silicon anode nanomate-

rials. That includes the design of novel structures,[195] dispersing silicon into an active or inactive matrix,[196] and coating the core–shell with an electronically conductive or inactive layer[197] as follows:

1) The creation of unique structures that can decrease volume expansion, pulverization, and contraction during the lithiation and delithiation of silicon anodes, respectively. That includes, for example, zero-dimensional nanoparticles (0D), nanowires, nanotubes, and nanorods (1D), and nanosheets and thin films (2D).
2) Various composites of active and inactive materials have been widely used in these approaches, with the inactive component serving as a structural buffer to reduce mechanical stress and help to reduce the significant volume changes of the active silicon. That prevents the electrode integrity from deteriorating.[198]
3) The core–shell structure consists of crystalline silicon (Si) in the core and a conducting material or inactive layer as the shell. Si mainly contributes to the capacity of the LIBs. In contrast, layer materials allow for the prevention of Si particle aggregation, can buffer significant volume changes, and form a stable solid-electrolyte interface (SEI) layer (**Figure 10**). Furthermore, conducting materials can further increase electrical conductivity. As a result, core–shell architectures can enhance the capacity retention and cyclability of LIBs.[199]

The most common technique for addressing these issues is covering the Si anode with various carbonaceous nanomaterials to create Si@C core–shell structures. Examples are carbon black,[200] carbon nanotubes,[201] graphite,[202] and graphene.[201,203] The mechanical characteristics, electrical conductivity, and capacity to accommodate Li^+ insertion and extraction of the carbon shell materials can all affect the long-term cyclability and kinetics of the LIBs.[204] During several alloying processes, the carbon layer serves as a soft medium to absorb
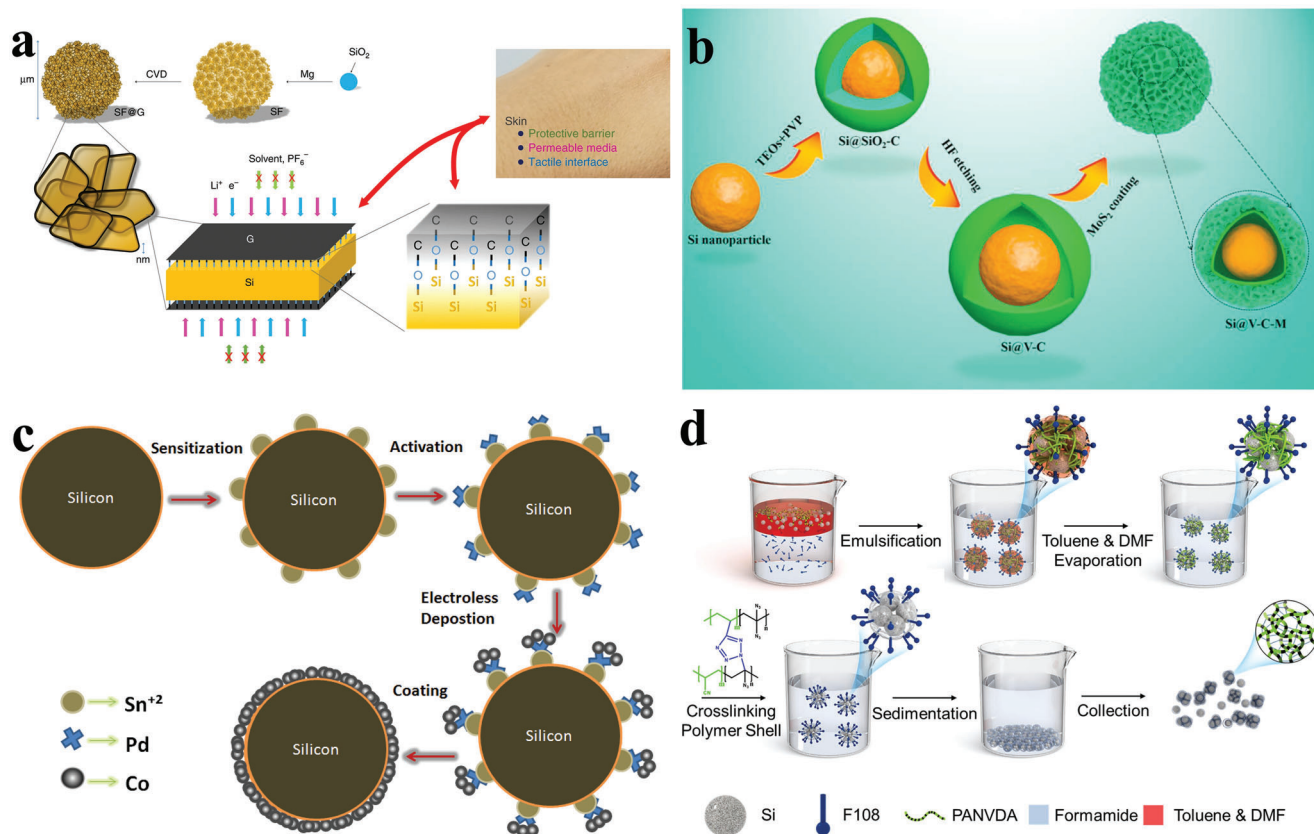
Figure 11. a) Schematic illustration of the synthesized SF@G features a two-dimensional covalently bound component interface. Reproduced with permission.[207] Copyright 2020, Springer Nature. b) Schematic illustration of the synthesis of Si@V-C-M (void-carbon-MoS₂) composite anodes. Reproduced with permission.[210a] Copyright 2020, Elsevier. c) Schematic illustration of the core–shell Si/Co composite powder formation by electroless cobalt plating. Reproduced with permission.[218] Copyright 2014, Elsevier. d) Schematic illustration of the synthesis process of Si NPs@x-PAN core–shell material via an emulsion-based technique. Reproduced with permission.[224] Copyright 2022, Elsevier.

volume changes.[205] The physical barrier of the carbon shell isolates the contact between silicon and electrolyte, thereby improving the stability of the SEI film.[206] To address the issue of significant volume changes in silicon electrodes during cycling, Zhi and colleagues proposed a new design for skin-like covalent encapsulation of silicon electrodes. This methodology is described as 2D covalent encapsulation using chemical vapor deposition (CVD), as illustrated in **Figure 11**a. The novel material design is demonstrated using covalently bonded, 2D silicon-carbon hybrid materials. Regarding weight, volume, and area, their excellent reversibility, capacity, and rate capability provide a remarkable degree of integrated performance. The binding of Si and C is crucial because it creates a reliable and effective contact between silicon and electrically conductive C, allowing rapid electronic and ionic transfer to/from silicon.[207]

Nevertheless, silicon anodes can be coated with the most widely used inert materials, such as metal silicide,[208] metal oxides,[209] metal sulfides,[210] and silicon oxides.[211] Due to the unique characteristics of these inactive shell materials, it is possible to increase the adhesion to the conductive binders and prevent the formation of unstable SEI layers when silicon comes into direct contact with the electrolyte. The volume expansion of silicon particles during cycling also declined to maintain its structural electrode integrity.[212]

Figure 11b schematically shows the fabrication process of molybdenum sulfide (MoS₂)-C double-protective-shell layers that Wang and co-workers developed to reduce the structural collapse of the silicon anode in yolk-shell (Si@V-C-M) anodes. The exterior MoS₂ shells withstand mechanical stress to maintain structural integrity and stability. In contrast, polyvinylpyrrolidone-produced carbon shells provide internal voids (V) to inhibit the volume expansion of silicon nanoparticles. Additionally, this intricately designed architecture promotes Li⁺ and e⁻ transport by reaping the benefits of pseudo-capacitance behavior driven by coating structure. The reversible capacity, extended cycle stability, and better rate performance of the Si@V-C-M yolk-shell may be improved by the structural evolution and kinetics properties of the (de)lithiation process.[210a]

However, the carbon coating method necessitates a high-temperature operation of >700 °C, such as carbonizing carbon materials or the thermal decomposition of acetylene gas. These metal coating techniques are highly valuable and may be applied at relatively low temperatures to improve the electrical conductivity of Si-based materials further.[213] Metallic materials (Ag,[214] Al,[215] and Cu[216]) with high mechanical strength, outstanding ductility, and high electrical conductivity can be used as coatings to create tougher, more flexible forms that can withstand volume expansion of silicon during cycling. Meanwhile, the high

ADVANCED
SCIENCE NEWS
www.advancedsciencenews.com

small
methods
www.small-methods.com

electrical conductivity of the coating material provides fast pathways for the transfer of electrons. Its high electrochemical stability can prevent direct contact between silicon and the electrolyte through core–shell coating.[217] Figure 11c shows the pretreatment and electroless deposition procedure and illustrates the method that Cetinkaya et al. provided for forming core–shell Si/Co materials. The improved charge transfer kinetics and decreased charge transfer resistance resulted from the higher core–shell Si/Co conductivity Increasing the cobalt content at the silicon surface improves the cycling performance and capacity retention of the electrode because the cobalt shell layer acts as a buffer against significant volume changes during the Li^+ insertion and extraction process.[218]

Furthermore, conductive polymer coatings are another choice that can be synthesis at low temperatures and is a scalable process. The coating layers of conductive polymer (PPy,[219] PANI,[220] polyacrylic acid (PAA),[221] and PEDOT[222] on silicon nanoparticles show excellent electrical conductivity, excellent chemical stability, and high structural stability of LIBs. All that is due to the uniform Li^+ transport around the silicon nanoparticles ascribed to the wettability of polar solvents on the conductive polymer coatings. This wettability prevents the localization of Li^+ insertion, leading to an ultrafast rate capability and a prolonged cyclic performance.[223] The synthesis of silicon nanoparticles with cross-linked PAN (Si NPs@x-PAN) via an emulsion-based technique is depicted in Figure 11d by Park and colleagues. Ultra-thin PAN polymer coating layers may help to improve the long-term cyclability of LIBs. Such layers compensate for the mechanical stress of silicon nanoparticles. More specifically, silicon nanoparticles are provided with a homogeneous Li^+ current by cross-linked, nanometer-thick PAN coatings. Cross-linking the PAN polymer chains significantly increased their elasticity. That also efficiently distributed the stress from the silicon nanoparticles and permitted extremely stable cycling performance.[224]

6. Scalable Synthesis of Core–Shell Techniques

6.1. Solid-Phase Reactions

The most common technique for applying coatings on cathode and anode materials in LIBs as core–shell structure is by liquid and gas phase reactions. For example, liquid phase reactions include wet-chemical, sol-gel, hydrothermal/solvothermal, electrochemical methods, and chemical polymerization routes. The advantage of liquid phase reaction is the creation of uniform particle size distributions and smaller size particles at the nanoscale. Generating a compound with high crystallinity and the ability to carry out the reaction at lower temperatures prevents damage to the host structure.[225] However, the drawbacks of this method include 1) the risk of damaging Ni-rich cathode materials caused by ion exchange between Li^+ from the cathode materials and H^+ from the solution when using aqueous solutions. 2) Concerns for the environment are raised when using organic solvents because of the waste streams that may be produced and the possible emissions of volatile organic compounds. 3) Requires extra processing steps (filtering and drying process), increasing energy costs, and negatively affecting the environment. 4) Low yield, high precursor cost, and challenging scaling up of these processes.[226]

Gas phase reactions such as CVD, physical vapor deposition (PVD), and ALD have the following advantages for providing both cathode and anode materials with core–shell structures:

1) The thickness of the coating layer can be controlled at the nanometer range and the shape of the coating layer corresponds to the surface of the substrate, resulting in a uniform thickness of the coating.
2) Various materials can be deposited, including surfaces made of conductive and insulating materials.
3) The processes involved only need a small amount of precursor, and the deposition temperature is low.
4) The surface coating can decrease the rate of surface reactions and increase ionic conductivity of the electrode.[227]

Unfortunately, gas phase reactions have various challenges with scaling up the deposition process, such as

1) The slow production rate of the coating layers.
2) Requires complicated synthesis procedures, which raises operating expenses.
3) The coating preparation procedure is complicated by eliminating the excess precursors when the coating is complete.[228]
4) Very expensive reaction.

Solid reactions are the preparation method between the solid core and solid shell material to create core–shell structures by mechanofusion process, ball-milling, and spray-drying process via physical-mechanical force. Recently, solid reactions have attracted widespread interest in scaling up the pilot plant processes for several reasons, such as: 1) solid reactions can perform continuously, producing several grams per minute. They offer easy and dependable access to small particles, ranging from tens to hundreds of nanometers, that can be generated from affordable precursors; 2) there are significant energy, money, and time savings since it avoids using hazardous solvents, binders, and subsequent drying; 3) these techniques make the dry particle coating approach for surface modification auspicious, affordable, environmental temperature, atmospheric pressure, and ecologically responsible; 4) reducing the solvent impurity that causes damage to active material during the core–shell synthesis process.[229]

Expanding upon the previously discussed solid-phase reactions, a table is included to further elucidate the impact of various shell materials and their associated preparation methods on LIBs. As illustrated in **Table 1**, an overview of various phase reaction synthesis methods, including liquid, gas, and solid reactions, are employed to synthesize core–shell morphologies for both anode and cathode materials. The application of these protective shell coatings plays a significant role in substantially augmenting the electrochemical performance of LIBs, ultimately contributing to enhanced rate capability and cycling stability.

6.1.1. Mechanofusion Process

Figure 12a illustrates a mechanofusion machine consisting of three parts: a chamber parts, a press head, and a scraper. The material must be coated with particles of two different sizes in order to produce a core–shell structure using a mechanofusion

Table 1. Overview of various phase reaction synthesis methods for core–shell morphologies applied to cathodes and anodes.

Core material	Shell material	Phase reaction	Method	Electrochemical performance			Ref.
				Capacity [mAh·g^{-1}]	Capacity [mAh·g^{-1}] @ 1.0C	Capacity retention [% cycles^{-1}]	
Layered cathodes							
NCA	C	Liquid	Wet chemical	220@0.1C	180	88/200@1C	[230]
		Gas	CVD	121@0.05C	80	90/100@0.1C	[231]
		Solid	Mechanofusion	200@0.1C	178	84/250@0.5C	[115b]
		Solid	Ball-milling	187@0.1C	175	97/80@0.2C	[232]
NMC	C	Liquid	Wet chemical	200@0.2C	175	94/50@1C	[233]
		Liquid	Sol-gel	191@0.5C	179	90/100@1C	[234]
		Gas	CVD	207@0.1C	175	94/100@0.1	[235]
		Solid	Mechanofusion	192@0.1C	160	78/200@1C	[236]
		Solid	Ball-milling	114@0.15C	64	33/200@1.0C	[237]
NMC	ZrO$_2$	Liquid	Sol-gel	205@0.1C	128	95/50@0.1C	[92b]
		Liquid	Wet chemical	180@0.1C	150	98/25@0.2C	[238]
		Gas	ALD	200@0.1C	170	94/50@0.5C	[92a]
		Solid	Mechanofusion	193@0.1C	133	83/200@1C	[239]
		Solid	Ball-milling	197@0.2C	175	83/100@0.5C	[240]
		Solid	Spray-drying	161@0.1C	139	87/40@1C	[241]
NMC	Al$_2$O$_3$	Liquid	Wet chemical	199@0.1C	–	99/100@0.5C	[242]
		Liquid	Freeze drying	272@0.1C	200	97/90@1C	[243]
		Gas	ALD	213@0.1C	–	74/100@0.1C	[244]
		Solid	Mechanofusion	184@0.1C	110	77/300@0.5C	[245]
		Solid	Spray-drying	182@0.1C	–	148/100@0.5C	[246]
Spinel cathodes							
LMO	C	Liquid	Wet chemical	98@0.1C	–	91.2/100@0.1C	[247]
		Liquid	Hydrothermal	138@0.1C	–	98/100@0.1C	[148b]
		Gas	CVD	–	–	90/200@0.1A·cm^{-3}	[248]
		Gas	ALD	120@0.1C	80	–	[249]
		Solid	Mechanofusion	129@0.2C	118	82/1000 @0.75C	[250]
		Solid	Ball-milling	121@0.1C	116	96/100@0.2C	[150]
LNMO	SiO$_2$	Liquid	Wet chemical	133@0.1C	130	97/200@0.1C	[172a]
		Liquid	Sol-gel	260@0.2C	220	78/40@1C	[251]
		Solid	Mechanofusion	127@1C	127	89/100@1C	[252]
		Solid	Ball-milling	130@0.5C	133	97/400@10C	[253]
Silicon anodes							
Si	C	Liquid	Wet chemical	1800@0.1A·g^{-1}	–	90/50@0.1A·g^{-1}	[254]
		Liquid	Polymerization	1887@0.5C	650	86/40@0.5C	[255]
		Gas	CVD	2500@0.3A·g^{-1}	–	53/70@0.3A·g^{-1}	[256]
		Solid	Mechanofusion	1500@0.1C	1000	67/1000@1C	[257]
		Solid	Ball-milling	680@0.2C	600	94/50@0.2C	[258]
		Solid	Spray-drying	480@0.2C	460	86/500@0.2C	[259]
Si	Graphite	Liquid	Wet chemical	816@0.1C	723	82/50@0.2C	[260]
		Liquid	Hydrothermal	860@0.2C	797	86/150@0.2C	[261]
		Gas	CVD	537@0.1C	–	95/50@0.5C	[262]
		Solid	Mechanofusion	950@0.1C	950	68/100@0.25C	[263]
		Solid	Ball-milling	1800@0.1 A·g^{-1}	–	50/140@0.1A·g^{-1}	[264]
		Solid	Spray-drying	2757@0.1A·g^{-1}	–	99/500@0.5A·g^{-1}	[265]

**ADVANCED
SCIENCE NEWS**

www.advancedsciencenews.com
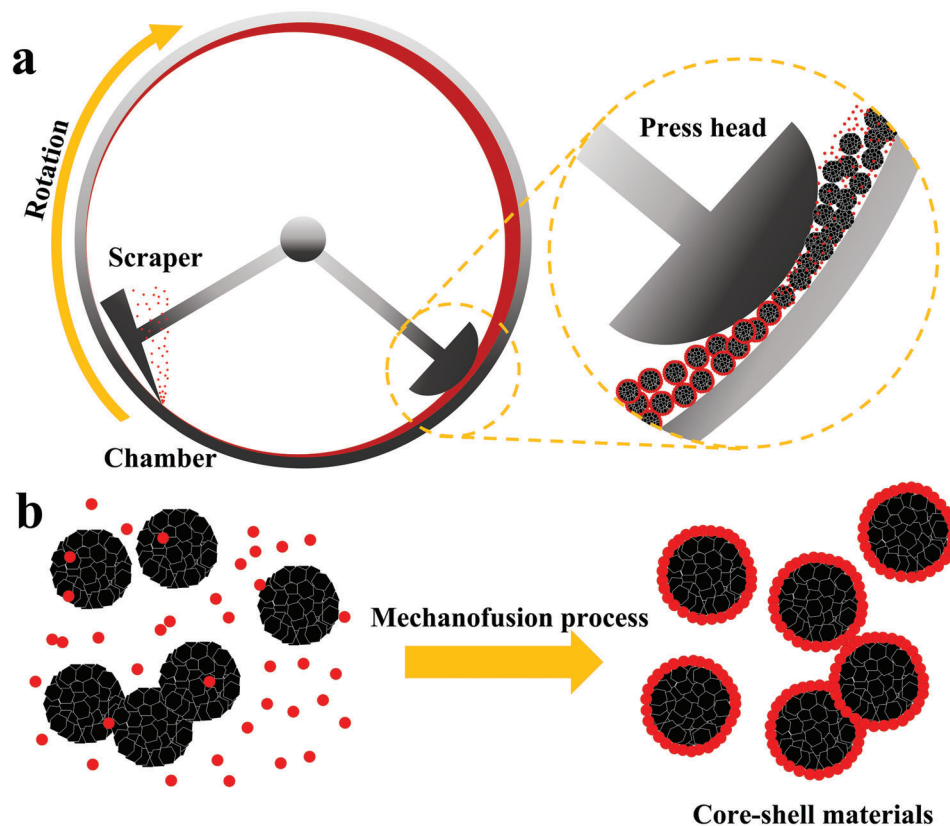
**small
methods**

www.small-methods.com

Figure 12. Schematic illustration of a) a mechanofusion system and b) scalable synthesis of core–shell materials via mechanofusion.

process.[266] The larger particles, in this example, were most probably micrometers in diameter, while the smaller particles were in the nanometer range. The large particles coated were core material, and the small particles are responsible for the formation of the shell material. The mixing powders are added to the chamber and referred to as feedstock. It consists of a rotating cylindrical chamber, a fixed press head and a scraper. At the beginning, the rotation of the chamber can generate a centrifuge force between mixing powders and the chamber wall leading to the acceptable aggregation of shell particles to adhere to the surface of larger particles. And then, mixing powder passes through the converging space between the fixed press head and the rotating chamber wall. The large particles then collide with other large particles at a high shear rate, transferring some of the small particles which have adhered to their surfaces. The small aggregates gradually disperse at all large particle surfaces by friction and collision between particles. The quantity of mechanical energy input, which can temporarily melt the particle surface, significantly impacts the dispersion rate and degree of collision. As the particles come out of the diverging space of the press head region, the particles adhere to each other and the chamber wall.

The function of the scraper is to remove the powder that is adhered to the chamber wall. The sheared particle combination then returns to the chamber and moves again into the direction of the press head. The sheared particles continuously undergo this process of compression, frictional shearing, and deagglomeration while the chamber rotates.[267] Finally, the continuous coating process ensures that all the particles get their

turn running through the press head thousands of times, creating a core–shell structure, as shown in Figure 12b. A homogeneous coating over the core particles is guaranteed by high-rate operation (1000–5000 rpm) and a continuous mechanical force with a three-dimensional dispersion without damaging the morphology. In addition, mechanical coatings depend only on compression, collision, friction, and shearing forces to adhere the shell material particles to the surface of the core material particles without needing any solvents or binders. Despite the small size of the shell particles, van der Waals interactions may be strong enough to maintain firm attachment of the shell particles to the core particle.[268]

Operational parameters impact the coating of core–shell structures through the mechanofusion process.

1) Processor rotation rate

Core and shell material particles deagglomerate with increased rotating rate and improved flow characteristics leading to a more uniform distribution at the surface of the core material particles. Moreover, increasing the processor rotation rate does not harm properties and do not damage core–shell materials.

2) Processing time

A minimum processing time is necessary so that core and shell material particles deagglomerate. The shell material particles have enough time to coat the core material particle surfaces.

2300345 (18 of 46)

**ADVANCED
SCIENCE NEWS**

www.advancedsciencenews.com

**small
methods**

www.small-methods.com

In addition, increasing the time can guarantee that the shell material completely covers the surface of the core material. However, increasing the processing time does not impact the flow properties because mechanofusion does not result in significant particle attrition. This means that the process energy does not break or micronize the particles.[269]

3) The degree of coverage at the surface of core material particles

The degree of coverage at the surface of the core material particles in the core–shell structure depends on several factors, including: i) the required particle size ratio of the core to shell being greater than 10:1; ii) the properties of the shell material; iii) the relative adhesive properties of the core and shell particles; iv) adjusting the distance between the press head and scraper and the chamber wall; and v) the energy input from the machine.[270]

As shown in **Figure 13**a, the authors presented a synergistic effect of surface protection by coating NMC811 with crystalline inert ZrO_2 nanoparticles utilizing a green and scalable mechanofusion technology and Zr^{4+} doping via an annealing procedure at 800 °C.[239] After annealing, the cross-sectional FE-SEM image of the NMC@Zr-800 as core–shell is shown in Figure 13b. After annealing at 800 °C, the ZrO_2 shell was thinner as some Zr^{4+} migrated into the bulk of the NMC811, particularly in the Li layer. The shell thickness decreased from 245 to 60 nm. Additionally, TEM images of NMC@Zr-800 with EDS mapping reveal that the ZrO_2 shell is uniformly distributed at the surface of NMC811 with adjustable Zr^{4+} doping in the bulk, introduced by the subsequent annealing procedure. Figure 13c displays the contour plots of the in operando XRD spectra for the three 2θ regions containing the (003), (101), and (104) diffraction peaks of NMC@Zr-800. According to the NMC@Zr-800, which exhibits a normal phase change similar to the pristine NMC811, the material structure did not collapse throughout the mechanofusion and high-temperature annealing process.

Furthermore, in operando XRD analysis using Rietveld refinement was utilized to determine the changes in lattice parameters and unit cell volumes during lithiation and delithiation. The results showed that the c-parameter rapidly increased and gradually decreased as Li intercalation occurred. In contrast to unmodified NMC811, the lattice properties and cell volume of NMC@Zr-800 underwent minimal alterations. The presence of Zr^{4+} in the Li-slabs acted as a pillaring agent, preserving the layered structure and hindering rapid shrinkage and potential microcrack formation during charging at high voltages. The small change in the c-lattice of NMC@Zr-800 at 4.3 V provided further evidence for this. Additionally, the cell volume change in NMC@Zr-800 was lower than that of pure NMC811. The cycling test showed that the ZrO_2 coating and Zr^{4+} doping synergistically enabled NMC@Zr-800 to exhibit excellent capacity retention after 200 cycles. Electrochemical performance, including rate capability, cycle performance, and coulombic efficiency, was evaluated for all materials, with C-rates ranging from 0.1 to 2.0 C in the same potential window (Figure 13d). At C-rates of 0.1, 0.25, 0.5, 1.0, and 2.0 C, NMC@Zr-800 demonstrated discharge capacities of 193, 183, 157, 133, and 111 mAh·g^{-1}, respectively. The improved rate performance at higher C-rates could be attributed to the presence of Zr^{4+}, which could increase the Li layer spacing and promote Li$^+$ diffusion. The cycling performance of NMC@Zr-800 at a high charge current of 1.0 C for 200 cycles was exceptional, with a capacity retention of 83% and a coulombic efficiency of ≈100%.

According to Figure 13e, all materials were also evaluated with respect to the electrochemical performance using 18 650 cylindrical full-cells. The study evaluated the rate capability, cycle performance, and coulombic efficiency of cells at 1.0 C after 1000 cycles. The cells included NMC811//Graphite, NMC@Zr//Graphite, and NMC@Zr-800//Graphite within a voltage range of 3.0–4.3 V at 0.1–2.0 C. The NMC@Zr-800 demonstrated the highest rate performance with reduced polarization, especially at high C-rates, consistent with the half-cell results. In the stability test of the 18 650 full-cells, cells were operated at a high rate of 1.0 C for 1000 cycles with a practically constant discharge voltage. The NMC@Zr-800 cell showed the best capacity retention of 68% due to the synergistic doping and coating effect, improving the Li$^+$ diffusion coefficient and kinetics while reducing crack formation and metal dissolution. These benefits enabled good rate capability and excellent cycling stability, as observed in both half-cells (CR2032) and 18 650 cylindrical full-cell batteries.

Figure 14a illustrates the use of a green and scalable solvent-free mechanofusion process to create a core–shell structure of NMC811 with a thin layer of carbon nanosphere coating (NMC811cs). This approach aims to address the drawbacks of NMC811 such as poor electrical conductivity, cation mixing, parasitic reactions with electrolytes, and the formation of microcracks, by incorporating a carbon nanosphere coating. The FE-SEM image of NMC811cs, which exhibits a smoother surface appropriate for uniformly coating with a carbon shell, can be seen in Figure 14b. Furthermore, the EDS mapping result from HR-TEM images reveals carbon shell layers of 50 nm carbon nanospheres uniformly covering the surface of NMC811. The NMC811 core displays a distinct crystalline structure, in contrast to the carbon nanospheres, which have a turbostratic structure with amorphous and graphitic regions. Interestingly, it is possible to see that some regions of the NMC811 materials surface have overlapping carbon nanospheres. The high-rate rotation results in an interparticle collision, compression force, and localized high temperature, leading to surface fusion and penetration of fine particles into the larger particle bodies. The contour plot of the in operando XRD spectra, which includes the (003), (101), and (104) diffraction planes, illustrates the selected three 2θ regions of NMC811cs (Figure 14c). The NMC811cs demonstrated a typical phase shift, much like the original NMC811, indicating that the structure was preserved with improved lithium storage capabilities following the mechanofusion process.

In addition, the in operando XRD measurement supports the rapid and uniform phase change with minimal Li$^+$ diffusion and kinetics resistance. The abrupt shrinkage in the c-axis does not affect the structural integrity of NMC811cs since it exhibits better cycle stability than the original NMC811 with less c-parameter variation. At increasing rates, it was discovered that the Li content and overpotential in the LiO6 layer of NMC811 are related to the contraction in the c-lattice. In a coin half-cell, the rate capability and cycle tests were evaluated (Figure 14d). The rate capability of NMC811 and NMC811cs were measured at various current densities between 0.1 and 5.0 C and a potential window between 3.0 and 4.4 V versus Li$^+$/Li. In the study, it was observed that NMC811cs has specific capacities of 191, 182, 175, 168, 160, 142, 134, and 105 mAh·g^{-1} at 0.1, 0.25, 0.5, 0.75, 1.0, 2.0, 2.5, and 5.0
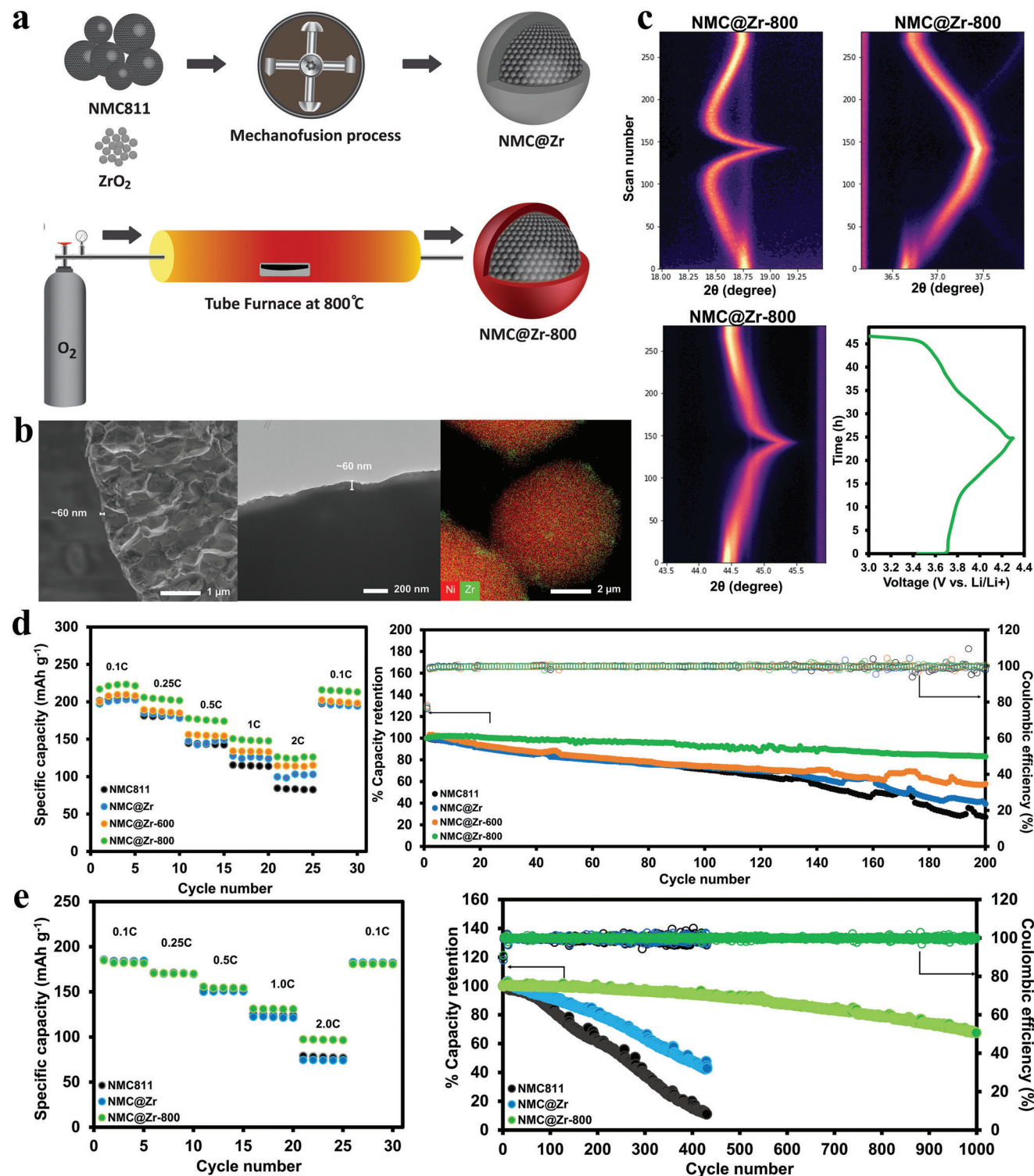
Figure 13. a) Schematic illustration of NMC@Zr core–shell preparation via mechanofusion process and NMC@Zr-800 with a subsequent annealing process. b) cross-sectional FE-SEM, TEM images, and EDS mapping of NMC@Zr-800. c) Contour plots of in operando XRD spectra of NMC@Zr-800 at 0.05 °C. d) Rate capabilities and cycle performance and coulombic efficiency at 1.0 °C after 200 cycles of NMC811, NMC@Zr, NMC@Zr-600, and NMC@Zr-800. e) Rate capabilities and cycling test and coulombic efficiency at 1.0 C after 1000 cycles of NMC811, NMC@Zr, and NMC@Zr-800 18 650 full-cells. Reproduced with permission.[239] Copyright 2022, Wiley-VCH.

Figure 14. a) Schematic illustration of NMC811cs (NMC811@C core–shell) core–shell preparation via the mechanofusion process. b) FE-SEM, HR-TEM images, and EDS mapping of NMC811cs. c) Contour plots of in operando XRD spectra of NMC811cs at 0.1 C. d) Rate capabilities and cycle performance and coulom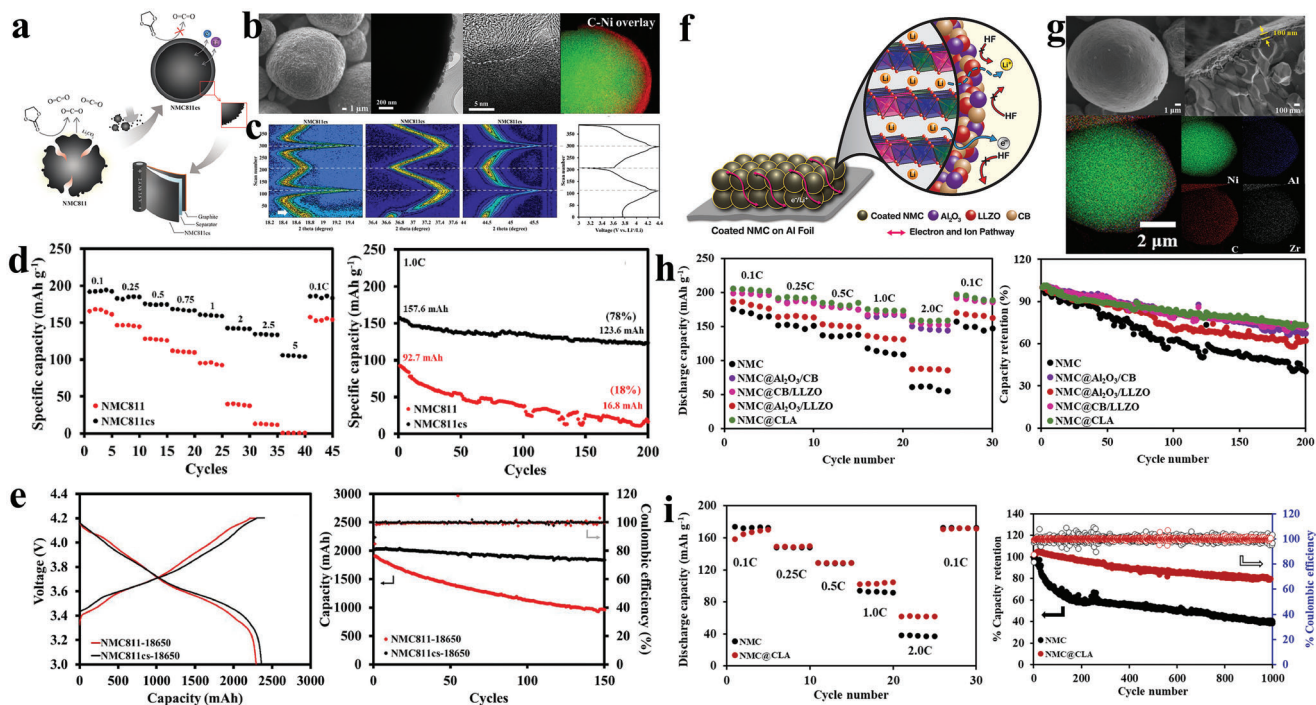bic efficiency at 1.0 C after 200 cycles of NMC811 and NMC811cs. e) GCD profiles at 0.1 C and stability test at 1.0 C of NMC811 and NMC811cs 18 650 full-cells. Reproduced with permission.[236] Copyright 2021, Elsevier. f) Schematic illustration of an NMC@CLA core–shell configuration can prevent acidic HF scavenger and increase the electronic conductivity. g) FE-SEM, STEM images with EDS mapping of NMC@CLA. h) Rate capabilities and capacity retention of the uncoated and coated NMC cathode at 0.5 C for 200 cycles. i) Rate capabilities and capacity retention and coulombic efficiency of long-term cycling performance at 1.0 C of NMC and NMC@CLA 18650 full-cells. Reproduced with permission.[271] Copyright 2023, Elsevier.

C. The results indicated that NMC811cs had higher capacity with reduced polarization during charging and discharging at all current densities. The lower overpotential observed in NMC811cs indicated that Li$^+$ insertion and extraction occurs without being impeded by Li$^+$ diffusion or (dis)charge kinetics. Additionally, after 200 cycles at a high current of 1.0 C, NMC811cs showed a capacity retention of 78%, which was significantly higher than the bare NMC811 cell (18%).

The charge and discharge profiles and stability test results for the 18650 cylindrical full-cells constructed of NMC811//Graphite and NMC811cs//Graphite are shown in Figure 14e. The charge-discharge profiles were evaluated using constant current constant voltage (CCCV) in the voltage range of 3.0–4.2 V at 0.1 C. Compared to NMC811 in its pure state, the NMC811cs exhibits a similar expected capacity of around 2.4 Ah (216 Wh·kg^{-1}$_{cell}$) at a nominal voltage of 3.66 V. In addition, the stability test was performed for 150 cycles at a high rate of 1.0 C. After testing, the NMC811//Graphite 18 650 cell shows a rapid capacity decline to 50%. That is potentially caused by the pure NMC811, which was exposed to crack formation, electrolyte side reactions, and low conductivity.

On the other hand, the NMC811cs shows capacity retention of 90% after 150 cycles. In 18 650 battery prototype cells, NMC811cs exhibit superior cycle stability and better specific capacity and energy compared to pure NMC811. This research offers foundational knowledge and a financial plan for reliable high-energy

LIBs. These findings demonstrate the critical role that carbon nanosphere coating plays in achieving superior specific capacity, energy density, and cycle stability compared to pristine NMC811, which is advantageous for pilot plant scale high-energy 18 650 LIBs.[236]

In Figure 14f, novel multi-functional three materials coatings on NMC811 are presented, which have been produced via a dry, green, and scalable solvent-free mechanofusion process (NMC@CLA). The coating materials include a high chemical stable Al_2O_3, high electrical carbon black (CB), and high ionic conductive $Li_7La_3Zr_2O_{12}$ (LLZO) to reduce parasitic reactions, internal charge transfer resistance, and enhance Li$^+$ diffusion, respectively. The morphology of these materials has been characterized by FE-SEM and STEM with EDS mapping (Figure 14g). After coating with mechanofusion (NMC811@CLA), the FE-SEM images showed a smoother surface with a slight change in particle diameter. The STEM image with EDS mapping demonstrates uniformly dispersed chemical elements, and all overlaying elements results demonstrate the thickness of CLA around 100 nm. In other words, mechanofusion may produce spherical NMC811 particles as core–shell structures with smooth surfaces and low surface energies. That indicates the formation of modified surface structures, microstrains, and local lattice variation, which improves the stability of NMC811.

In addition, the cross-sectional FE-SEM image confirms the shell thickness of around 100 nm, which agrees with the result

**ADVANCED
SCIENCE NEWS**

www.advancedsciencenews.com

**small
methods**

www.small-methods.com

of STEM. Figure 14h demonstrates the rate capability at various C-rates, ranging from 0.1 to 2.0 C, and capacity retention at 0.5 C for 200 cycles of the uncoated and coated NMC811 cathode coin half-cells. Consequently, the use of NMC811@CLA coating materials in the multi-functional three materials coating strategy of this study significantly enhances the overall cell performance. The coating of three combinations of materials on NMC811 exhibits high discharge capacities of 205, 193, 184, 174, 158, and 192 mAh·g^{-1} at 0.1, 0.25, 0.5, 1.0, 2.0, and 0.1 C, respectively. The cells were tested during long-term cycling at 0.5 C in a window potential of 3.0–4.3 V for 200 cycles. The NMC@CLA cells demonstrated outstanding capacity retention during the stability test up to 73%. The synergistic effect of the three combinations can enhance electrochemical performance in rate capability and cycling ability due to better electronic conductivity (CB), inert shell protectability (Al$_2$O$_3$), and good ionic conductive (LLZO).

Figure 14i demonstrates the rate capability test at various C-rates in the range of 0.1–2.0 C and capacity retention at 1.0 C for 1000 cycles of the NMC811//Graphite and NMC@CLA//Graphite 18 650 cylindrical full-cells. The increased specific discharge capacity is due to the CLA multi-functional layer at the surface of NMC811, especially at high C-rates, delivering 167, 149, 128, 103, 62, and 171 mAh·g^{-1} at 0.1, 0.25, 0.5, 1.0, 2.0, and 0.1 C, respectively. Compared to the uncoated NMC811, the discharge capacity of NMC@CLA is approximately two times higher at 2.0 C. The identical specific capacity at low C-rates (0.1–0.5 C) showed that using CLA materials as a shell does not decrease the usage of active material but rather improves the Li$^+$ diffusion pathway and enhances the kinetics of the thick electrode, particularly at high current rates. The higher electrical conductivity of CB as a shell component of CLA can reduce the IR drop of the cell compared with bare NMC811 cells. After the cycling test at 1.0 C with a window potential from 3.0 to 4.2 V for 1000 cycles, NMC@CLA outperforms the bare NMC811, maintaining capacity retention of over 80%, whereas NMC811 gives ≈38%. CLA-shielded NMC811 particles outperform the bare NMC811, maintaining capacity retention of over 80%. In comparison, NMC811 provides only 38% after cycling tested at 1.0 C with a window potential from 3.0 to 4.2 V for 1000 cycles. This work[271] exhibited that the combination of three shell materials can overcome intrinsic drawbacks of high Ni-rich cathode materials, including micro-cracking, parasitic reactions, and metal dissolution at the upscale production for a 18 650 cylindrical full-cell configuration with a high overall electrochemical performance.

Sawangphruk et al. exhibited the nano-sized conductive carbon coated on the LMO (LMO@C) with the core–shell structure synthesized using a dry mechanofusion process.[272] The morphologies of LMO@C materials synthesized by the mechanofusion process were investigated by FE-SEM and HR-TEM with EDS mapping (**Figure 15**a). FE-SEM images show the uniform cover on the LMO surface, providing a core–shell structure with a diameter of around 8 µm after mechanofusion processing by coating carbon nanoparticles. In the HR-TEM images, the carbon shells are composed of 2–4 overlapping carbon nanospheres with a thickness of around 40–50 nm. There are no void areas between the core particles and the carbon shells. Because of the strong compressive force and high heat energy produced during the mechano-thermal process, carbon, and LMO adhere

to one another very well. The carbon coating layer is expected to enhance the electrical conductivity and decrease the dissolution of Mn in LMO by preventing direct contact with the electrolyte and severe HF attack. Additionally, EDS mapping supports the uniformity of the carbon coating, in which the C atomic ratio at the shell decreases to 0% as the LMO@C particle approaches its center. In contrast, the percentage of Mn atoms increases as it approaches the center of the particle. Figure 15b shows the contour plots of the in operando measured XRD spectra of LMO@C during lithium deintercalation and intercalation. The in operando XRD results of LMO@C cathodes showed two peaks in the dQ/dV curves, corresponding to a two-phase transition throughout the (dis)charge operation. The XRD peaks slowly changed to higher 2θ in the initial charging state with <50% Li$^+$ extraction by the decrease in lattice characteristics. The ionic radius and cell diameters decreased as the average Mn oxidation state increased. Following that, additional deintercalation of Li$^+$ from Li$_{0.5}$Mn$_2$O$_4$ triggers a solid-solution reaction to produce Li-deficient Li$_{1-\delta}$Mn$_2$O$_4$ when Li$^+$ extraction approaches 50% at 4.05 V. The mixed phase of Li$_{1-\delta}$Mn$_2$O$_4$ and λ-MnO$_2$ was also generated at a high state of charge (SOC). The formation can be seen as a new phase towards the end of charging (red circle). The XRD peaks migrated back to lower 2θ during Li$^+$ re-intercalation (discharging), showing a reversible phase change to cubic LiMn$_2$O$_4$. The variation of lattice parameters during (de)lithiation was also estimated using in operando XRD with Rietveld refinement. During the charging process in P-LMO, the lattice parameter constantly reduced from 8.20 to 8.0 Å with the λ-MnO$_2$ phase at xLi$^+$ with x is reduced from 0.4 to 0.2 (60% Li$^+$ deintercalation). While LMO@C shows significantly less of the λ-MnO$_2$ phase, it did so after Li$^+$ deintercalation for about 75% (xLi$^+$ = 0.25–0.15). Lesser formation of λ-MnO$_2$ and suppressed contraction and expansion of the crystal lattice are demonstrated by the minor appearance of the λ-MnO$_2$ phase and lower variation in the parameter of LMO@C. In other words, the mechano–thermal carbon-coated LMO core–shell can inhibit phase transformation, particularly lowering the occurrence of an unstable two-phase area (Li$_{1-\delta}$Mn$_2$O$_4$ + λ-MnO$_2$ mixed phase) at high voltages.

These findings demonstrate that carbon shells can stabilize the phase transition, reduce Mn dissolution, and prolong battery life. The electrochemical performance of LMO material in coin-type half-cell batteries before and after the coating is shown in Figure 15c. The rate performance for P-LMO and LMO@C at potentials 3.0–4.3 V at various C-rates is plotted. About 129, 115, 107, 93, and 82 mAh·g^{-1} discharge capacities for LMO@C were achieved at 0.1, 0.5, 1.0, 2.0, and 3.0 C, respectively. On the other hand, the specific discharge capacities of P-LMO are 121, 107, 96, 84, 66, and 48 mAh·g^{-1}, which correspond to 0.1, 0.5, 1.0, 2.0, and 3.0 C, respectively. The growing electrode polarization, caused by the rising overpotential and rising internal resistance, or IR drop, is responsible for the poor specific capacities at high C-rates. LMO@C exhibits lower polarization and higher capacities at high C-rates than the P-LMO; this difference might be attributed to the increased e$^-$ conductivity, which increases the usage of the active material. The electrochemical performance of cylindrical 18 650 P-LMO//Graphite and LMO@C//Graphite full-cells are shown in Figure 15d. At faster rates of 0.75 and 1.0 C, the LMO@C//Graphite cells showed slightly better rate-capability, possibly because of the enhanced conductivity from
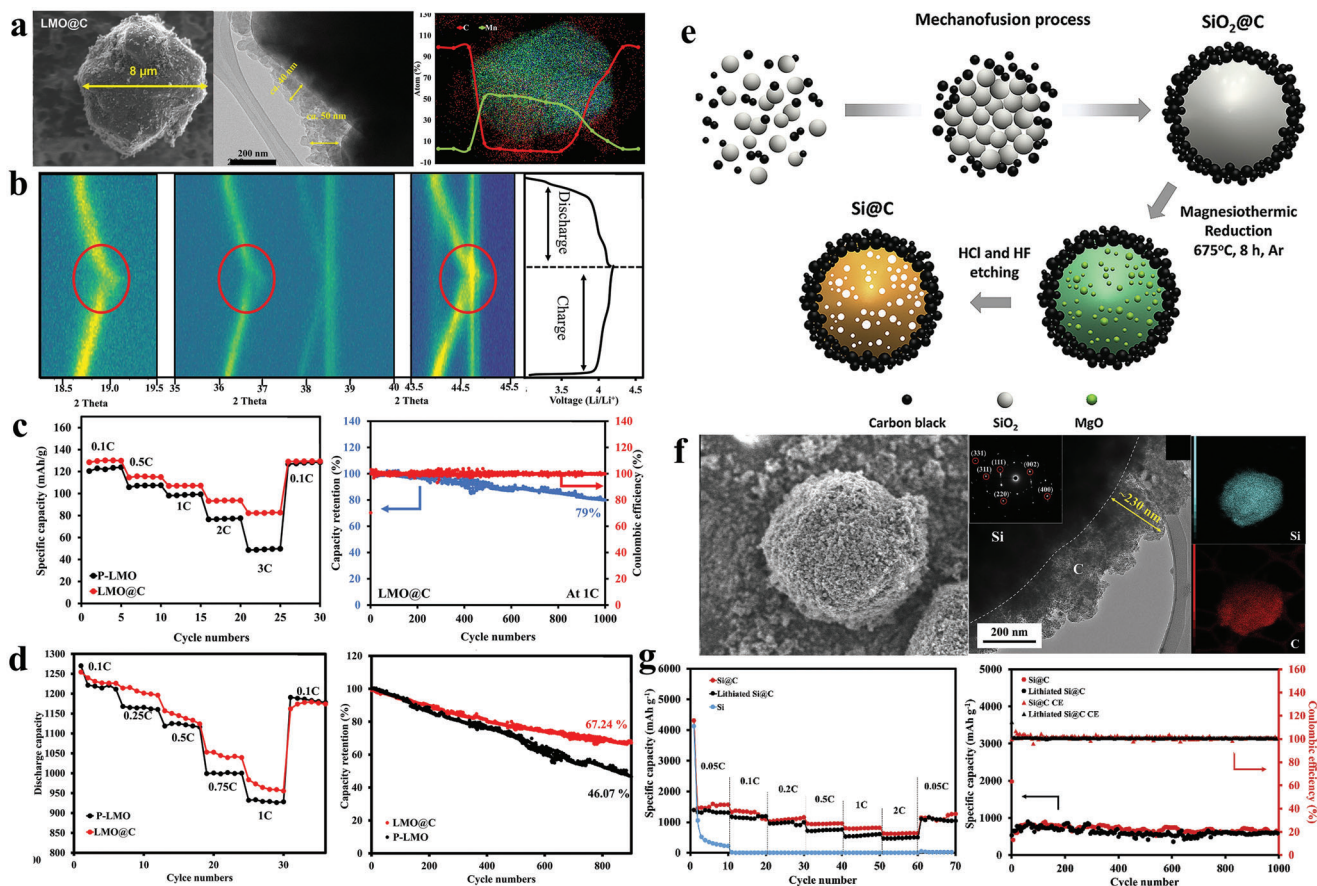
**ADVANCED
SCIENCE NEWS**

www.advancedsciencenews.com

**small
methods**

www.small-methods.com

Figure 15. a) FE-SEM, HR-TEM images and EDS mapping of LMO@C. b) Contour plots of in operando XRD spectra of LMO@C. c) Rate capabilities and cycle performance and coulombic efficiency at 1.0 °C after 1000 cycles of LMO@C. d) Rate capabilities and cycling stabilities of P-LMO and LMO@C 18 650 full-cells. Reproduced with permission.[272] Copyright 2021, Springer Nature. e) Schematic illustration of Si@C core–shell preparation via mechanofusion process. f) FE-SEM, TEM images, and EDS mapping of Si@C. g) rate capability tested at 0.05–2.0 C and cycling performance at 1.0 C of Si@C, lithiated Si@C, and Si anodes. Reproduced with permission.[257] Copyright 2020, Elsevier.

the carbon coating, as discussed earlier. The constant current stability test was conducted at a high rate of 1.0 C for 900 cycles. The capacity retention of the P-LMO//Graphite cell declined significantly to 46% after 900 cycles due to several issues, including Mn dissolution, Mn redeposition at the anode, mixed phase transition, and low conductivity. On the other hand, the LMO@C cell maintained its capacity retention at 67% after 900 cycles, indicating that the carbon shell improved the stability of cylindrical LIBs.

Finally, to generate silicon–carbon nanoparticle core–shell materials (Si@C) with interparticle void space, Sawangphruk and co-workers devised a unique, scalable mechanofusion process that produced carbon nanospheres-encapsulated SiO_2 (SiO_2@C), as shown in Figure 15e.[257] Figure 15f demonstrates FE-SEM, TEM, and EDS mapping of the as-produced Si@C. The carbon was coated at the SiO_2 to produce SiO_2@C using a solvent-free mechanofusion process. Carbon nanospheres with a particle size of ≈3–5 mm are uniformly coated at the surface of the SiO_2 particles. Despite being chemically reacted with Mg at high temperatures and in an acidic environment, the Si@C core shell morphology maintains its structure with particles of a similar size to those of SiO_2@C. Encapsulation of Si with carbon nanoparticles

with an estimated shell thickness of around 230 nm can be observed in TEM images of Si@C.

The pure crystalline form of Si was confirmed by TEM analyses of the crystalline Si planes using selected area electron diffraction (SAED). In contrast, STEM-EDX images can support the coverage functionality on the surface of Si@C. For inner Si particles to expand freely within the carbon confinement without cracking during cycling, the provided core–shell structure is advantageous. Additionally, interconnected carbon nanoparticles maintain the SEI thickness by preventing Si particles from coming into direct contact with the electrolyte and improving the material's conductivity. The first discharge capacity of Si@C synthesized from SiO_2 is 4308 mAh·g^{-1} with an initial coulombic efficiency of 33.8%. In contrast, subsequent cycles show a specific capacity of 1387 mAh·g^{-1}, then gradually decline after the rate capability test and get a capacity of 1259 mAh·g^{-1} at the last discharge cycle at 0.05 C. It should be noted that the initial lithiation has a substantial irreversible capacity due to the creation of an unstabilized SEI. The problem can be solved by pre-lithiating the Si@C electrode through the use of a 20 mL electrolyte in direct contact with the Si@C anode and lithium chip. After 2 h of pre-lithiation, the anode, now in a lithiated Si@C form, was

ADVANCED
SCIENCE NEWS
www.advancedsciencenews.com

small
methods
www.small-methods.com

assembled into a coin-cell battery and tested. The first irreversible discharge capacity disappeared with a high initial coulombic efficiency of 98%, indicating that the SEI layer has already stabilized at the anode. Successive cycles provided a steady specific capacity at different applied C-rates, similar to the cell using pure Si@C.

Bare Si without an additional buffer layer demonstrates rapid degradation. That originates from the formation of thick SEI layers and significant volume changes, resulting in strong pulverization. Both Si@C and lithiated Si@C exhibit a similar trend in their long-term stability tests. Both materials can maintain a specific capacity of 600 mAh·g^{-1} after 1000 cycles with 100% coulombic efficiency at 1.0 C. The electrochemical results show that the additional carbon shell of Si@C acts as a protective layer to stabilize the SEI thickness development and prevent particle cracking owing to the severe volume expansion upon lithiation, which is advantageous for highly stable batteries (Figure 15g). One method for stabilizing the SEI and forming it uniformly during cycling tests involves the use of carbon-encapsulated silicon created through a solvent-free mechanofusion technique. This method introduces more e$^-$ and Li$^+$ to react with and enables silicon particles to expand freely within the buffer shell without breaking. Due to its stable structure, cost-effectiveness, simplicity, and scalability of synthesis, as well as its suitability for applications requiring high energy and stability, carbon-encapsulated silicon (Si@C) is a promising anode material for high energy, scalability, and stability in LIBs.

In conclusion, coating various protective shell layers on the surface of anode and cathode core materials in LIBs can be achieved through the use of the mechanofusion process. Core–shell materials show significantly improved electrochemical performance (discharge capacity, rate capability, and cycling stability) and can easily be upscaled for pilot plant production. **Table 2**. summarizes the latest research synthesis of core–shell structures of both cathodes and anodes via mechanofusion.

6.1.2. Ball-Milling Process

The complexity, inefficiency, and high cost is often a barrier to mass produce core–shell materials. Ball-milling is a low-cost, high-yielding, and scalable technique for efficiently producing core–shell structures of cathode materials (layered and spinel) and silicon anode materials, making it feasible for pilot plant manufacturing.[282] The synthesis of core–shell structures in ball-mill equipment results from the energy impact of balls between the shell and core material. A chamber, the balls, and driver roller are essential components of a ball-mill machine, as schematically shown in **Figure 16**a. The axis of the chamber might be horizontal or slightly inclined to fill the balls into the chamber. Ceramic, stainless steel, flint pebbles, and chrome steel can all be used to produce the balls. The feed and mill size determines the diameter of the balls, which account for 30–50% of the mill capacity. The interior surface of the chamber shell is often lined with abrasion-resistant material, such as rubber or manganese steel. At the start, all the materials and balls inside the chamber rotate following the rotational force of the driver roller. The balls encounter centrifugal forces from the base plate rotation, and the chamber-independent revolution causes the balls to hit the inner wall simultaneously. Balls can have energy up to 12

times greater than gravitational acceleration. The collisions between the core and the shell material are caused by two balls or a ball against a wall chamber, thus leading to the adhering of shell material into the core material generated by the impact energy during the rotation movement. The continuous coating process, which results in core–shell structures, guarantees that all the particles can go through the impact energy of balls thousands of times (Figure 16b). So, mechanical ball-milling generating the coating layer is non-destructive to the host material and is available for commercial use. In addition, literature reports applying high temperatures of the calcination process in air. That helps to create a smooth and compact surface of the core–shell structure after the ball-milling process.[283]

Operational parameters impact the coating of core–shell structures through the ball-milling process.

1) Factors determining the efficiency of the ball-milling process

Critical factors, such as the type of balls (chrome steel, stainless steel, flint pebbles, and ceramic), affect the formation of core–shell structures with different core and shell materials. Other ball factors affect the core–shell synthesis, for example, size, density, the number of balls, and the nature (hardness) of the balls and material to be ground.

2) Processor rotation rate

The rotating rate is crucial when using a ball-milling process. At slow rate, the ball mass rolls or slides over one another inefficiently. Centrifugal forces drive the balls at high rate into the wall chamber. Since there is no collision at this rate, there is no coating. Comminution cannot occur due to inadequate ball compression against the chamber wall. However, the centrifugal rate force only manifests at 50–80% of the critical rate, which causes the balls to be practically carried to the top of the mill before falling to the bottom. The core and shell materials adhering between the balls impact the coating.

3) Processing time

The core and shell particles must have a minimum processing time to adhere together by impact force. In addition, the increased time can guarantee that the shell material completely covers the surface of the core material.[284]

The group of Li[285] presented interface engineering for coating nano-LATP ($Li_{1.5}Al_{0.5}Ti_{1.5}(PO_4)_3$) at the surface of LCO (LCO@LATP) by ball-milling and annealing as a solid reaction method (**Figure 17**a). SEM and STEM images investigated the morphological evolutions of the LATP@LCO-700 after annealing, as shown in Figure 17b. After mechanically coating with LATP, SEM images demonstrate that the smooth surface of bare LCO is uniformly coated with a rough layer of microparticles. The surface becomes smooth and compact after the annealing process at high temperatures. It develops into freshly produced grains with larger particle sizes. Although the bulk structure does not change during annealing, the observed morphological modifications suggest that LCO and LATP chemical interactions occur at the surface of LCO@LATP. The high-resolution HAADF images revealed distinct, well-defined crystalline structures inside the material. The surface layer structure exhibits

**ADVANCED
SCIENCE NEWS**

www.advancedsciencenews.com

**small
methods**

www.small-methods.com

Table 2. Summary of mechanofusion synthesis of various core–shell morphologies to be applied as cathodes and anodes.

Sample	Core material	Shell material	Condition		Electrochemical performance			Note	Ref.
			Rate [rpm]	Time [min]	Capacity [mAh·g^{-1}]	Capacity [mAh·g^{-1}] @1.0C	Capacity retention [% cycles^{-1}]		
Layered cathodes									
LCO@LTO	LCO	LTO	5000	20	185@0.2C	160	84/100@0.5C		[69]
LCO@LTO//Graphite					–	–	90/15@0.5C		
NCA@C	NCA	C	5000	30	200@0.1C	178	84/250@0.5C		[115b]
NCA@LFP	NCA	LFP	1500	10	190@0.1C	–	–	Calcined at 400 °C for 1 h in air	[273]
NCA@LFP//Graphite					–	–	95/150@0.5C		
NMC622@Al$_2$O$_3$	NMC622	Al$_2$O$_3$	1400	30	200@0.1C	–	97/50@0.1C		[274]
NMC811@LATP-PC	NMC811	LATP-PC	5000	40	210@0.2C	190	81/10@1C		[275]
NMC701515@Al$_2$O$_3$	NMC701515	Al$_2$O$_3$	2000	6	182@0.1C	155	92/100@0.5C	Annealed at 600 °C for 8 h in air	[276]
NMC701515@Al$_2$O$_3$	NMC701515	Al$_2$O$_3$	2000	6	179@0.1C	153	97/75@0.5C		[277]
NMC701515@TiO$_2$	NMC701515	TiO$_2$	2000	6	177@0.1C	145	87/75@0.5C		
NMC701515@ZrO$_2$	NMC701515	ZrO$_2$	2000	6	185@0.1C	155	85/75@0.5C		
NMC831205@B$_2$O$_3$	NMC831205	B$_2$O$_3$	2000	15	204@0.1C	175	97/100@1C	Annealed at 600 °C for 4 h in O$_2$	[278]
NMC811@C	NMC811	C	5000	20	192@0.1C	160	78/200@1C		[236]
NMC811@C//Graphite					190@0.1C	160	90/150@1C		
NMC811@ZrO$_2$	NMC811	ZrO$_2$	5000	20	193@0.1C	133	83/200@1C	Annealed at 800 °C for 6 h in O$_2$	[239]
NMC811@ZrO$_2$//Graphite					185@0.1C	135	68/1000@1C		
NMC811@Al$_2$O$_3$	NMC811	Al$_2$O$_3$	5000	30	184@0.1C	110	77/300@0.5C		[245]
NMC811@Al$_2$O$_3$//Graphite					–	145	91/450@1C		
NMC811@Al$_2$O$_3$/C/LLZO	NMC811	Al$_2$O$_3$/C/LLZO	5000	20	205@0.1C	174	73/200@0.5C		[271]
NMC811@Al$_2$O$_3$/C/LLZO//Graphite					167@0.1C	103	80/1000@1C		
NMC811@Li-IL/Al$_2$O$_3$//Graphite	NMC811	Li-IL/Al$_2$O$_3$	5000	30	188@0.1C	122	80/500@1C		[279]
Spinel cathodes									
LMO@C	LMO	C	5000	30	129@0.2C	118	82/1000 @0.75C		[250]
LMO@C	LMO	C	5000	30	130@0.1C	107	79/1000@1C		[272]
LMO@C//Graphite					125@0.1C	91	67/900@1C		
LNMO@Al$_2$O$_3$	LNMO	Al$_2$O$_3$	3000	30	117@1C	117	91/100@1C		[252]
LNMO@SiO$_2$	LNMO	SiO$_2$	3000	30	127@1C	127	89/100@1C		
LNMO@TiO$_2$	LNMO	TiO$_2$	3000	30	120@1C	120	92/100@1C		
LNMO@MgCO$_3$	LNMO	MgCO$_3$	3000	30	121@1C	121	95/100@1C		
LNMO@LFP	LNMO	LFP	–	–	123@0.08C	106	75/140@1C		[280]
Silicon anodes									
Si@Graphite//NMC622	Si	Graphite	2500	60	950@0.1C	950	68/100@0.25C		[263]
Si@C	Si	C	5000	5	1500@0.1C	1000	67/1000@1C		[257]
Si@rGO/Graphite	Si	rGO/Graphite	5000	30	741@0.3A·cm^{-2}	–	50/100 @2.8A·cm^{-2}		[281]
Si@rGO/Graphite//NMC811					179@0.1C	70	40/500@1C		

recognizable spinel structural characteristics with a thickness of between 10 and 20 nm, as indicated by the enlarged structure model of spinel-like phases shown in the red and green frames, respectively.

In comparison, the bulk structure maintains a pure layered structure with an interplane spacing of 0.47 nm corresponding to the lattice plane (003) of LCO. It is fascinating to observe that only at the 700 °C temperature of interest, all phases other than the olivine Li$_3$PO$_4$ phase are spinel (Co$_3$O$_4$, CoAl$_2$O$_4$, and Co$_2$TiO$_4$),

which are structurally coherent to the layered LCO lattice. According to the STEM images, the growth at the LCO surface is made possible only by creating spinel phases, which also ensures a homogeneous and conformal coating at the particle surface. From a chemical perspective, it has been shown that the addition of Ti is effective in stabilizing lattice oxygen at high voltages. It is known that Li$_3$PO$_4$ combines good Li$^+$ conductivity and chemical stability at high voltages, which can guarantee a stable high-voltage interface with reasonably high Li$^+$ diffusion kinetics. Figure 17c

**ADVANCED
SCIENCE NEWS**

www.advancedsciencenews.com
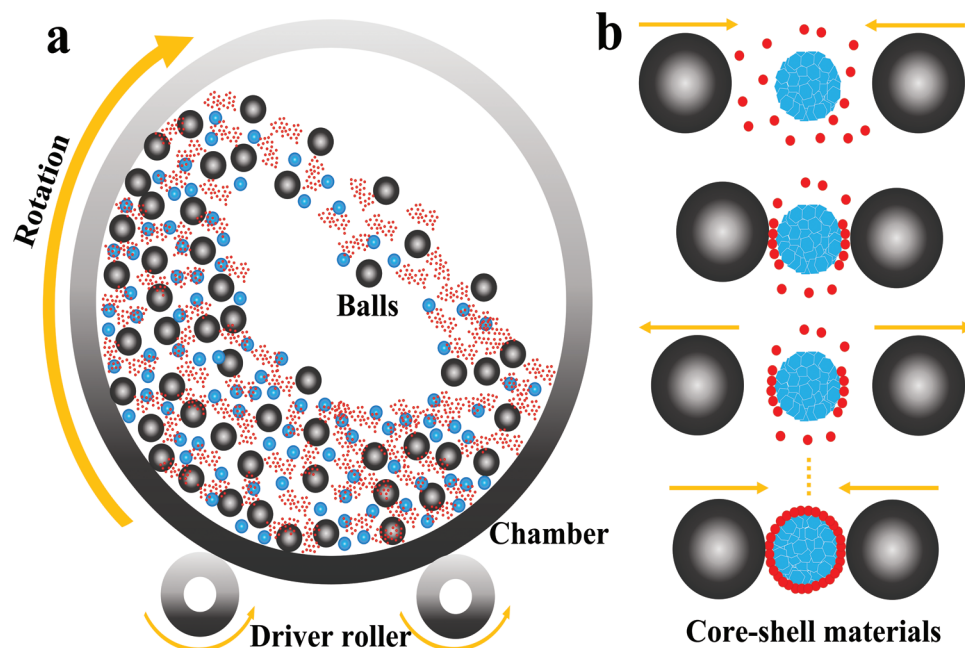
**small
methods**

www.small-methods.com

Figure 16. Schematic illustration of a) a ball-milling system and b) scalable synthesis of core–shell materials via a ball-milling process.

shows the cycling performance of bare-LCO and LATP@LCO-700 coin-type half-cells at 0.5 C at 25 and 45 °C, respectively. The rate capabilities of bare-LCO and LATP@LCO-700 are also compared in Figure 17c. At the cycling test at 25 °C, the LATP@LCO-700 demonstrates a more excellent discharge capacity retention of 88.3%.

In contrast, the bare-LCO cathode reveals a discharge capacity retention of 50% after 100 cycles. At 45 °C, the LATP@LCO-700 exhibits significantly improved cycle performance than bare-LCO, retaining 72.9% of its discharge capacity after 100 cycles compared to 32.5% for bare-LCO. The rate capabilities of the bare-LCO exhibit discharge capacity of 225, 193, 157, 120, and 68 mAh·g^{-1} at 0.1, 0.5, 1.0, 2.0, and 5.0 C, respectively. The LATP@LCO-700 shows discharge capacities of 216, 197, 181, 156, and 118 mAh·g^{-1} at 0.1, 0.5, 1.0, 2.0, and 5.0 C, respectively. That results in exceptional capacity retention of 54% at 5.0 C. Therefore, these results indicate that designing a surface coating with hybrid phases for LCO could increase the cycle stability and rate capability of cathodes. In particular, the Li$^+$ conductive Li$_3$PO$_4$ and LATP phases provide an efficient ionic transport pathway for facilitating interfacial kinetics. In contrast, the stable spinel phases can stabilize the interface between the cathode and electrolyte. These two phases collaborate to improve the cycle and rate performances of LATP@LCO-700 at severe conditions of high charging voltages and elevated temperatures. Additionally, the LATP@LCO-700 exhibits the highest high-temperature cycling performance among the given results compared to the previously reported surface-modified LCO cathodes, indicating a high initial discharge capacity and outstanding capacity retention (Figure 17d). These advantages contribute to developing a consistent, conformal, high-voltage surface layer with favorable Li$^+$ conducting kinetics at the LCO surface. At both room temperature and 45 °C, the improved LCO performs excellently over 4.6 V high-voltage cycles. Also significantly im-proved is the thermal stability, which has broad implications for developing alternative high-voltage, high-energy-density cathode materials.

In Figure 17e, Yao et al. described a coating amorphous ZrO$_2$ from UiO-66 precursor at the surface of NCM622 cathode materials (u-NCM622) by ball-milling and annealing. The development of a coating layer is demonstrated by short chain-like substances that adhere to the surface of the host material, as visualized by SEM images. Additionally, it can be concluded from the enlarged figure that the loose interspaces of UiO-66 were retained during annealing, which ultimately facilitates fast Li$^+$ and e$^-$ transfer. HR-TEM images show that the u-NCM622 particle has a coating layer of ≈5 nm thick. Meanwhile, it is evident from images of u-NCM622 materials that they have a layered hexagonal structure with a 0.239 nm lattice spacing that can be indexed to their (006) crystal planes. Notably, amorphous materials lack the crystallization process, which promotes ion migration and prevents volume expansion (Figure 17f).

As shown in Figure 17g, the current density was set between 0.2, 1.0, 2.0, 5.0, and 10 C before being progressively reduced to 0.2 C every five cycles. At 10 C, the NCM622 cathode could only discharge 81 mAh·g^{-1}, but the u-NCM622 cathode could retain 112 mAh·g^{-1}, which is 39% more than the original NCM622 cathode. The cycling stability of u-NCM622 was enhanced with a capacity retention of 82%, higher than those for pristine NCM622 (52%) over 2.8–4.5 V at 2.0 C after 100 cycles. The uniform ZrO$_2$ coating significantly stabilized the cathode/electrolyte contact, which is primarily responsible for these notable improvements. The uniform ZrO$_2$ coating layer has been demonstrated to prevent structural deterioration brought on by unfavorable side reactions with the electrolyte. The active sites on the NCM622 surface, which are also provided by the distinctive porous architecture of UiO-66, help to maintain Li$^+$ diffusion even at high levels during cycling.[240]

ADVANCED
SCIENCE NEWS
www.advancedsciencenews.com
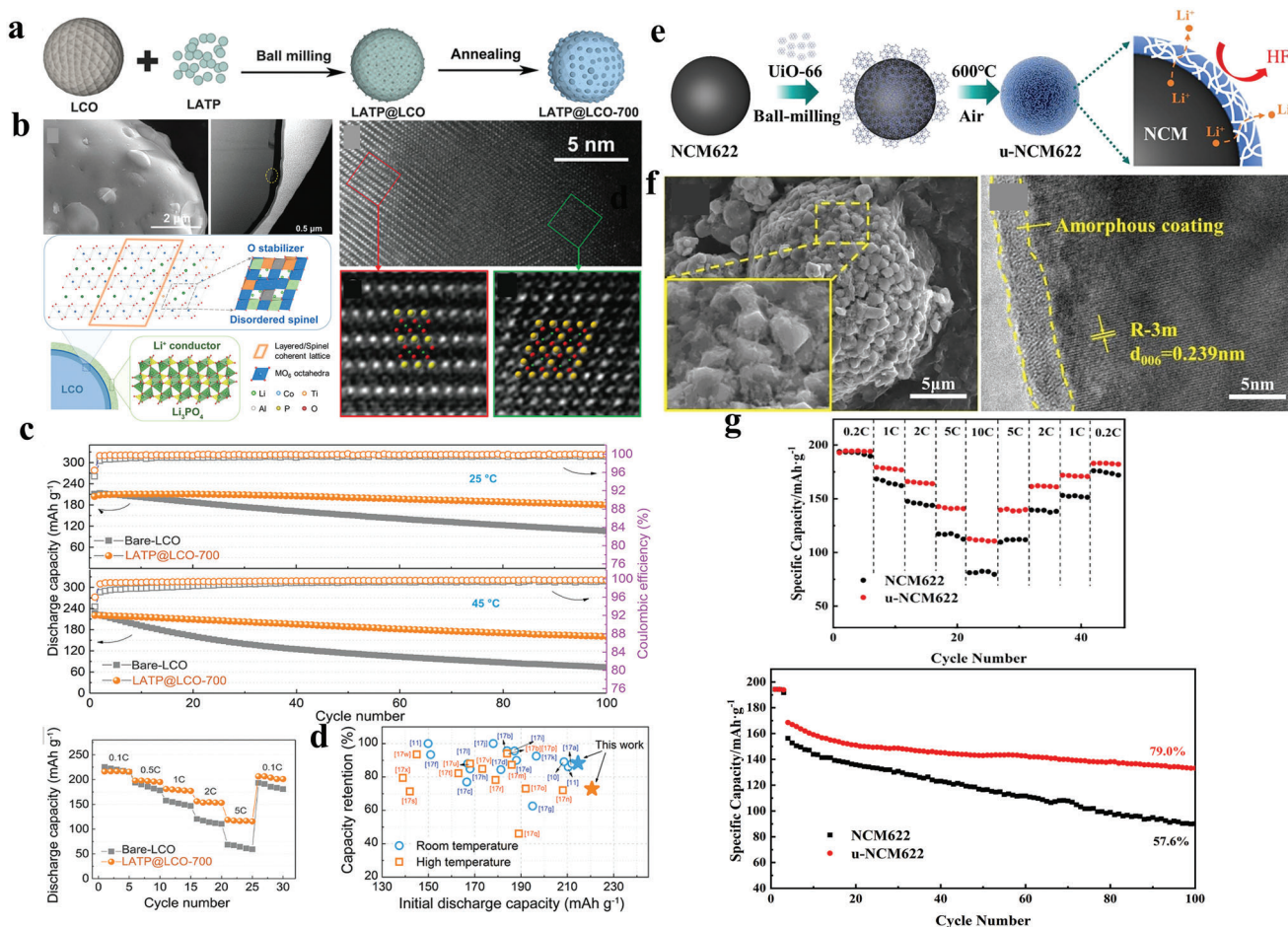
small
methods
www.small-methods.com

Figure 17. a) Schematic illustration of LCO@LATP core–shell preparation via ball-milling and subsequent annealing. b) SEM and STEM images of LCO@LATP-700. Atomic-resolution HAADF images in the surface region. Local layered and spinel-like phases are enlarged from the red and green frames, respectively, as indicated by the overlaid structural models and schematic illustration of the surface layer growth mechanism. c) Cycling performance of cells cycled at 0.5 C at 25 and 45 °C, and rate performance of bare-LCO and LCO@LATP-700 coin-type half-cells. d) Comparison of the cycling retention and initial discharge capacity of various LCO materials. Reproduced with permission.[285] Copyright 2020, Wiley-VCH. e) Schematic illustration of ZrO2 coating NMC622 (u-NMC622) prepared via ball-milling and annealing process. f) SEM and HR-TEM images of u-NMC622. g) Rate capacity and cycling performance at 2.0 C after 100 cycles of NCM622 and u-NCM622 coin-type half-cells. Reproduced with permission.[240] Copyright 2020, Elsevier.

Yin and colleagues showed the feasibility of coating WO_3 at the surface of $LiMn_2O_4$ with a core–shell structure using ball-milling and annealing in **Figure 18**a. Figure 18b shows SEM and HR-TEM images of 5 wt.% WO_3-coated $LiMn_2O_4$. The surface of the $LiMn_2O_4$ particles after WO_3 coating is noticeably rougher than the surface of bare $LiMn_2O_4$. The components at the particle surface are identified using HR-TEM of a 5 wt.% WO_3-coated $LiMn_2O_4$ particles and EDS. The average thickness of this shell is around 5 nm, and the EDS shows that Mn, O, and W elemental peaks are present. The coating is rather uniform. The results of the SEM and TEM analyses show that depositing the amorphous WO_3 layer onto the surface of $LiMn_2O_4$ by ball-milling is a successful synthesis method. The electrochemical performance before and after WO_3 coating is shown in Figure 18c. To evaluate the rate capability of bare $LiMn_2O_4$ and 2 wt% WO_3-coated $LiMn_2O_4$, charge and discharge tests have been performed at different rates. As the charge-discharge rates rise, the capacities of both materials decrease. However, the 2 wt% WO_3-coated $LiMn_2O_4$ declines

more gradually at high discharge rates than bare $LiMn_2O_4$. The sample with a 2 wt.% WO_3 coating recovers to its level at 0.2 C (125 mAh·g^{-1}), but the sample with bare $LiMn_2O_4$ recovers to its level at 0.5 C when the rate returns to 0.1 C (118 mAh·g^{-1}).

At room temperature, the cycling performance of uncoated $LiMn_2O_4$ and $LiMn_2O_4$ coated with 1, 2, 3, 4, and 5 wt% WO_3 has potential windows between 3.3 and 4.3 V at 1.0 C. Cyclability of $LiMn_2O_4$ cathode can be significantly enhanced by WO_3 coatings, especially for a coating amount of 2 wt%. The cycling characteristics deteriorate as the covering material content rises, while they are still superior to bare $LiMn_2O_4$. The inhibiting effect of the WO_3 coating at the $LiMn_2O_4$ particles is likely responsible for the improved cycling performance of WO_3-coated $LiMn_2O_4$. This layer prevents electrolyte degradation and the disproportionation reaction of manganese into the electrolyte solution. However, WO_3 will behave as an insulator, which is harmful to cycling if it excessively covers $LiMn_2O_4$. EIS was conducted on both the uncoated and coated $LiMn_2O_4$ at the 1st and 100th cycle to
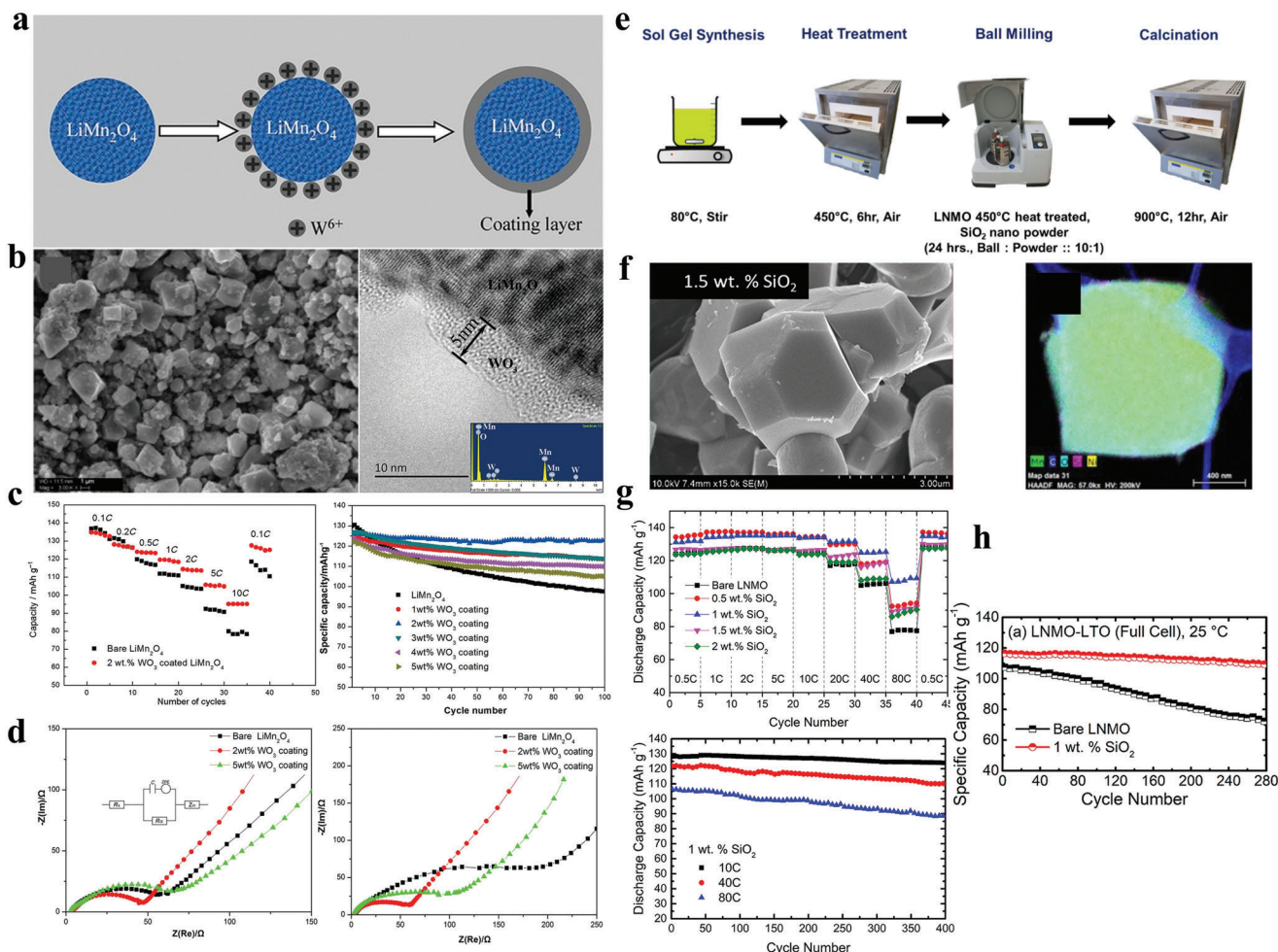
**ADVANCED
SCIENCE NEWS**

www.advancedsciencenews.com

**small
methods**

www.small-methods.com

Figure 18. a) Schematic illustration of $LiMn_2O_4@WO_3$ core–shell preparation via ball-milling. b) SEM, HR-TEM images, and EDS graph of 5 wt% WO_3-coated $LiMn_2O_4$. c) Rate capability of 2 wt.% WO_3-coated and bare $LiMn_2O_4$ coin-type half-cells and cycling performance of samples in a coin-type half-cell potential range of 3.3–4.3 V at 1.0 C after 100 cycles. d) EIS measurement of a bare $LiMn_2O_4$ and 2 and 5 wt% WO_3-coated $LiMn_2O_4$ at the 1st and 100th cycle. Reproduced with permission.[286] Copyright 2016, Wiley-VCH. e) Schematic illustration of $LNMO@SiO_2$ core–shell synthesis via the ball-milling process. f) SEM, TEM images with EDS mapping of 1.5 wt% SiO_2-coated LNMO. g) Rate capability of bare and SiO_2-modified LNMO (0.5−2 wt% SiO_2) and cycling performance of 1% SiO_2-modified LNMO at 10, 40, and 80 C at 25 °C for 400 cycles coin-type half-cells. h) Full-cell performance of LNMO//LTO and 1 wt% SiO_2-LNMO//LTO at 1.0 C (dis)charge cycling for 280 cycles. Reproduced with permission.[253] Copyright 2019, American Chemical Society.

understand further the underlying mechanisms of cycling deterioration. The cells were charged and discharged before the EIS analysis to ensure they were fully charged and activated.

The Nyquist plots for the bare $LiMn_2O_4$ and WO_3-coated $LiMn_2O_4$ are shown in Figure 18d after the second cycle and then after 100 cycles at room temperature. As a result, it can be seen that the charge-transfer resistance (R_{ct}) of electrodes made of bare $LiMn_2O_4$ and $LiMn_2O_4$ electrodes coated with 2 and 5 wt% WO_3 is 56.4, 44.2, and 65.4 Ω, respectively. At the first cycle, the R_{ct} rises in the following sequence: 2 wt% WO_3-coated $LiMn_2O_4$ < bare $LiMn_2O_4$ < 5 wt% WO_3-coated $LiMn_2O_4$. Due to WO_3, an insulator, the WO_3-coated $LiMn_2O_4$ has a slightly higher R_{ct} than bare $LiMn_2O_4$. R_{ct} values for the WO_3-coated $LiMn_2O_4$ materials grow less after the 100th cycle than for the bare $LiMn_2O_4$ electrode. The specific R_{ct}-values of the bare $LiMn_2O_4$ electrode and the electrodes with 2 and 5 wt% WO_3 coating are 178, 57.8, and

94.4 Ω, respectively. In conclusion, WO_3-coated $LiMn_2O_4$ combines a higher rate capability with a superior cycle life in comparison to bare $LiMn_2O_4$.[286]

Amin and co-workers[253] presented SiO_2-coated LNMO using a cost-effective, scalable ball-milling, and calcination process (Figure 18e). The morphology after coating with SiO_2 was evaluated by SEM and STEM with EDS mapping, as shown in Figure 18f. The truncated octahedron particle shape was visible in the SiO_2-coated SEM images, and particles were 2 µm in size on average. The 1.5 wt% SiO_2-LNMO exhibited a more uniform particle size distribution, and the particle size remained constant. The homogenous distribution of Li, Ni, Mn, O, and Si in the particles without any impurity elements is seen in the elemental mapping images of SiO_2-coated particles. Figure 18g shows the electrochemical performance before and after the SiO_2-coated LNMO coin half-cell. The discharge capacity of uncoated LNMO at 5.0 C

**ADVANCED
SCIENCE NEWS**

www.advancedsciencenews.com

**small
methods**

www.small-methods.com

is ≈125 mAh·g^{-1}. However, LNMO coated with 0.5 and 1 wt% SiO$_2$ showed greater initial capacity at all C-rates and better capacity retention compared to uncoated LNMO. The 2 wt% SiO$_2$-LNMO showed a lower capacity than 0.5, 1, and 1.5 wt% SiO$_2$-LNMO up to 10 C, which could be due to slower kinetics with an increase in coating thickness. A discharge capacity of ≈106 mAh·g^{-1} at 80 C was observed in the sample coated with 1 wt% SiO$_2$.

The rate capability results suggest that the performance of the cell at high C-rates may be limited by the charge transfer resistance at the electrode/electrolyte interface or Li$^+$ mobility in the electrolyte rather than Li$^+$ diffusion in the active materials. The excellent electrochemical performance of SiO$_2$-coated LNMO at high C-rates is attributed to the protective SiO$_2$ coating and SEI passivation layer. However, it is possible that the interfacial resistance could limit C-rates higher than 40 C. The authors discussed the LNMO electrode system thoroughly regarding various constraints at high C-rates. The 1 wt% SiO$_2$-LNMO was tested at three different high C-rates with 0.5 C charging and 10, 40, and 80 C discharge for 400 cycles.

The rate of discharge significantly impacted the cycling stability. The cell that was discharged at 10 C showed a minimal capacity loss of up to 400 cycles before becoming highly stable at 96%. In contrast, the cell that was discharged at 40 C experienced an 87% capacity retention. Despite cycling at 80 C, the cell still demonstrated a capacity retention of 82%. On the other hand, the 1 wt% SiO$_2$-LNMO showed an outstanding cycling performance when discharged at 10, 40, and 80 C. Figure 18h shows the full-cell cycle life of bare LNMO and 1% SiO$_2$-LNMO employing Li$_4$Ti$_5$O$_{12}$ (LTO) as an anode. For bare LNMO and 1% SiO$_2$-LNMO, the initial discharge capacities were around 106 and 118 mAh·g^{-1}, respectively. After 280 cycles, the uncoated LNMO//LTO battery showed a rapid decline in capacity, retaining only 67% of its initial discharge capacity. In contrast, the 1% SiO$_2$-modified LNMO//LTO battery demonstrated exceptional cycling stability, retaining 93% of its initial discharge capacity after 280 cycles at 1.0 C. The use of SiO$_2$ coatings on LNMO provides a scalable and cost-effective approach that reduces interfacial charge transfer resistance, making the material more suitable for electric vehicle batteries that require extremely fast charging.

Shen et al. produced hierarchical carbon-coated metallurgical Si material (HCC-M-Si) via a low-cost and large-scale ball-milling process. The fabrication of lightweight and free-standing electrodes consisting of the HCC-M-Si particles and carbon nanofibers via vacuum filtration, as schematically shown in **Figure 19**a. Figure 19b shows the morphological and elemental distribution of HCC-M-Si. Broad particle size dispersion and irregular particle shapes were found in SEM images. By filling the interstitial space with smaller Si particles, the wide size distribution can improve the effective occupancy of the electrodes. The Si nanoparticles in HCC-M-Si are uniformly covered by carbon shells. TEM images reveal that the void spaces left by the rigid template are visible between the carbon shell layer and the Si core. The HCC Si structure is also abundantly supported by STEM images of HCC-M-Si and the associated EELS mapping of C (green) and Si (red) components. Figure 19c shows the rate capability and cyclability of HCC-M-Si, HCC-M-Si(2), and M-Si in coin-type half-cells. HCC-M-Si and M–Si rate capabilities were

investigated under various current densities from 0.4 to 8 A·g^{-1}. The HCC-M-Si anode demonstrated substantially slower capacity losses at increasing rates than the M–Si anode. HCC-M-Si specifically provides reversible capacities of 2900, 2700, 2200, and 1500 mAh·g^{-1} with current densities of 0.4, 0.8, 2, and 4 A·g^{-1}. However, M–Si only provides 2000, 1800, 1000, and 100 mAh·g^{-1}, respectively. HCC-M-Si can maintain a reversible capacity of 950 mAh·g^{-1} at a current density of 8 A·g^{-1}, whereas M–Si shows little capacity.

This suggests that the hierarchical carbon coating can effectively decrease the interparticle resistance of silicon and increase capacity at high current densities. The cycling capacity of HCC-M-Si was compared to that of M–Si and HCC-M-Si(2), showing that HCC-M-Si has better cycling stability than HCC-M-Si(2) over 1000 cycles. After 1000 cycles, HCC-M-Si retains a reversible capacity of 1031 mAh·g^{-1}, whereas HCC-M-Si(2) only retains 540 mAh·g^{-1}. In contrast, M–Si shows poor cycling performance, with capacity dropping close to zero after only 100 cycles. The researchers attribute the high cycling stability of HCC-M-Si to the ample void space created between the carbon shells and Si particles, which supports the structure of the material after the volume changes of Si particles.

Good contact and high conductivity rely on maintaining structural integrity during the cycling process. The large surface area of the porous Si structure enhances Li$^+$ diffusion, and the thin walls between the pores decrease the diffusion route for Li$^+$ and e$^-$, resulting in superior electrochemical performance compared to monolithic Si. However, in this case, the porous structure is generated during the cycling process, which causes a significant volume expansion of particles. This volume expansion can damage the contact between Si particles and the current collector, as depicted in Figure 19d.

After 50 cycles, the HCC-M-Si STEM image indicates that the particles have maintained their smooth surface. The elemental mapping of C (green) and Si using EELS (red). The in situ formed porous Si particle occupies the original void space between the Si particle and the carbon shell while still being well confined within the carbon shell. By assisting the Si particles in maintaining good electrical contact with other materials, such as conductive additives and binders, can help to create electronic channels to the current collector and, as a result, achieve outstanding cycling performance. Galvanostatic charge–discharge profiles of the HCC-M-Si//LCO and HCC-M-Si//LNMO coin-type full-cells with operating voltage windows of 3–4.2 and 3–4.8 V, respectively, are shown in Figure 19e. The stable working voltage of the full-cells and the fabricated coin cells were used to power commercial blue and white light-emitting diodes (LEDs). The synthesis of HCC-M-Si core–shell structures, with their applications in lightweight free-standing electrodes and high-voltage full-cells, has the potential to facilitate further optimization of low-cost Si anodes with high energy density, leading to potential battery applications in the future.[287]

The Lu group[288] produced novel poly(vinyl alcohol) (PVA) coated silicon nanoparticles via reactive ball-milling (RBM). Figure 19f illustrates the RBM process, which utilizes bulk silicon to produce PVA-coated silicon nanoparticles with covalent bonds formed between PVA and the silicon surface. SEM and HR-TEM techniques were utilized to investigate the morphology of the samples after ball-milling, as depicted in Figure 19g.
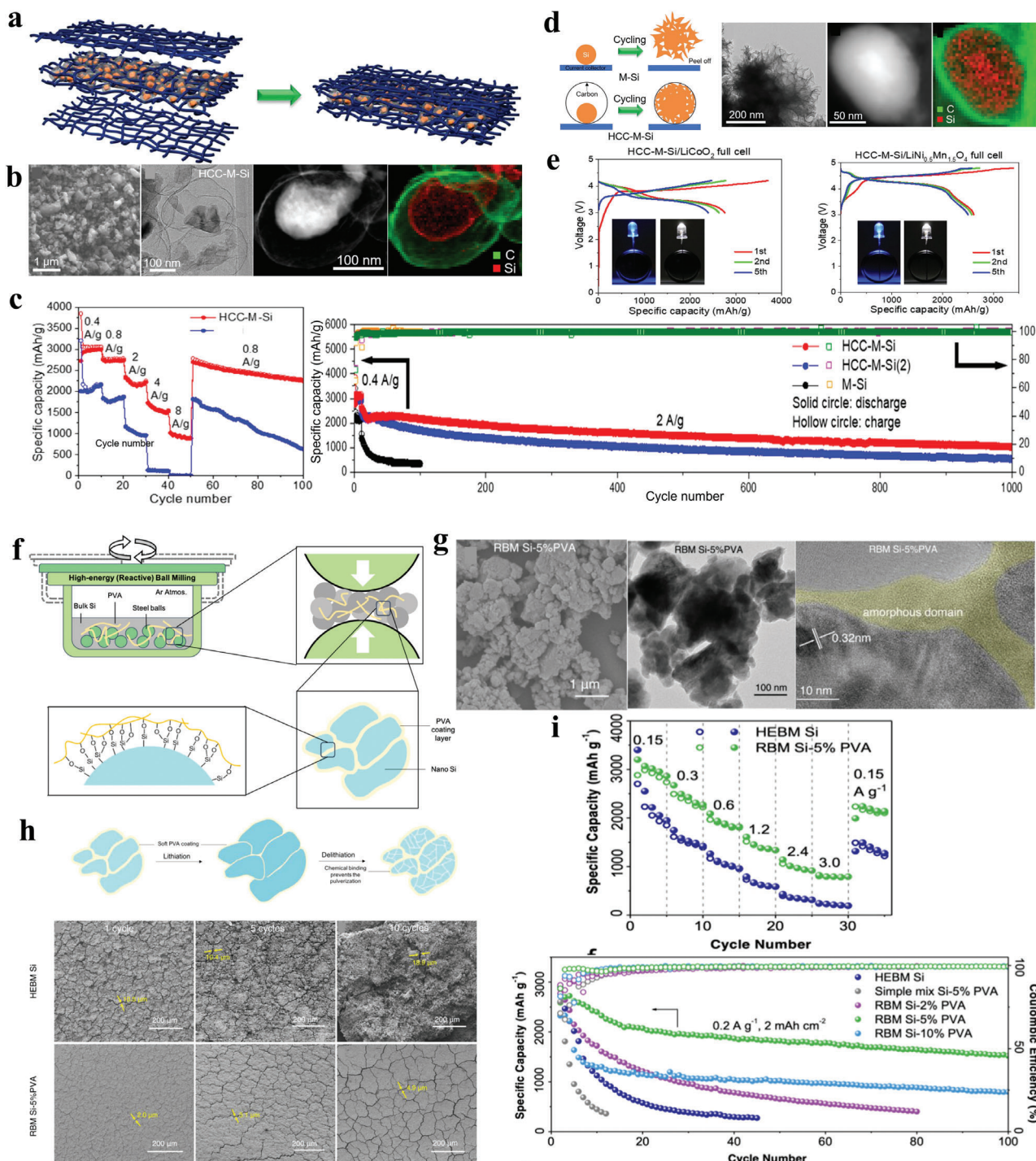
Figure 19. a) Schematic illustration of lightweight and free-standing HCC-M-Si/CNF electrode prepared via ball-milling and vacuum filtration. b) SEM, TEM, STEM images, and EELS mapping of HCC-M-Si. c) Rate capability comparison of HCC-M-Si and M-Si, and long-term cycling performance of HCC-M-Si, HCC-M-Si(2), and M-Si, the current density was 2 A·g^{-1} for 1000 cycles. d) Schematic illustration showing the morphological evolution of M-Si and HCC-M-Si after cycling. TEM image of M-Si and HCC-M-Si particle after 50 cycles and EELS mapping of elements C and Si in the HCC-M-Si particle. e) Galvanostatic charge—discharge profiles of HCC-M-Si//LiCoO$_2$ and HCC-M-Si//LiNi$_{0.5}$Mn$_{1.5}$O$_4$ full-cells. The inset shows that the full-cell can power blue and white LEDs. Reproduced with permission.[287] Copyright 2018, American Chemical Society. f) Schematic diagram of reactive ball-milling (RBM) is provided, depicting the process starting with the mixing of bulk silicon and poly(vinyl alcohol) (PVA), leading to the formation of PVA-coated silicon nanoparticles with covalent bonds between the PVA and silicon at the surface. g) TEM images of HEBM Si and RBM Si-5% PVA. HR-TEM image of RBM Si-5% PVA. h) Rate performance of HEBM Si and RBM Si-5% PVA and long-term cycling performances of ball-milled silicon materials at 0.2 A·g^{-1}. i) Schematic diagram of (de)lithiation of the ball-milled silicon materials. Morphology of cycled Si electrodes. SEM images of HEBM Si electrodes and RBM Si-5% PVA after 1, 5, and 10 cycles, respectively. Reproduced with permission.[288] Copyright 2020, American Chemical Society.

**ADVANCED
SCIENCE NEWS**

www.advancedsciencenews.com

**small
methods**

www.small-methods.com

High-energy ball-milling (HEBM) often results in severe and inevitable secondary aggregation of nanoparticles due to the high-energy surface of the particles being exposed. The absence of extra PVA causes the primary HEBM Si particles to agglomerate into secondary particles that are up to 10 μm, thus reducing the benefits of nanomaterials and producing significant structural changes during (de)lithiation. Covalent connections that develop between PVA and Si particles chemically quench the active surface, thereby reducing the formation of aggregates. In comparison to HEBM Si, RBM Si-5% PVA primary particles are typically smaller than 200 nm. SEM images illustrate that most RBM Si-5% PVA secondary particles range from 0.5 to 1 μm. The HR-TEM images of RBM around 200 nm in size and evenly scattered are the Si-5% PVA particles. The HR-TEM image reveals the silicon (111) lattice with an interplanar spacing of 0.32 nm. The amorphous layer is shown to surround the Si nanocrystals, which might be attributed to the polymer, covering the surface of amorphous Si. The in situ generated polymer framework efficiently separates the Si nanoparticles, effectively preventing agglomeration during HEBM. This unusual structure not only accommodates volume changes of the Si particles but also protects them from any potential damage.

Figure 19i compares the rate capability and cyclability before and after PVA coating in a coin-type half-cell configuration. The capacity of RBM Si-5% PVA gradually decreases to 801 mAh·g^{-1} and recovers to 2234 mAh·g^{-1} as the current returns to 0.15 A·g^{-1} in the rate performance tested at different C-rate from 0.15 to 3.0 A·g^{-1}. The silicon materials that were ball-milled at a loading of 1 mg·cm^{-2} and a current density of 0.2 A·g^{-1} were tested for cycle stability. Si-PVA nanocomposites produced using RBM synthesis present enhanced stability and higher capacity retention compared to the dramatic capacity fading of HEBM Si. Notably, the best improvement is provided by the RBM Si-5% PVA. The electrode is activated within 10 cycles, then gradually stabilizes and maintains this stability for subsequent cycles, retaining a 1526 mAh·g^{-1} reversible specific capacity after 100 cycles. For the RBM Si-10% PVA electrode, a significant capacity loss of 1395 mAh·g^{-1} occurs in the 5 cycles, and after 100 cycles, the reversible capacity is 798 mAh·g^{-1}. The rapid capacity fading in the first few cycles is thought to be caused by the extreme polymer solvation and swelling carried out by the increased PVA content, which leads to more substantial structural changes.

To further highlight the critical significance of RBM, HEBM Si is stirred and combined with 5% of PVA because of the electrolyte interactions with the reactive groups on PVA. The electrode rapidly degrades without a strong chemical reaction to maintain its integrity. The robust PVA coating production method, which supports the silicon electrode cycling stability, is shown in Figure 19h. To prevent phase separation during the volume changes of silicon particles, PVA polymer with a linear chain structure can stretch and contract at the Si surface, creating a permanent chemical interaction with the particle surface. This interaction strengthens the PVA coating, enabling it to act as a buffer layer and protect the particles from pulverization and withstand volume expansion, enhancing the stability of the electrode during cycling. In contrast, physical contact between the PVA and particle surface would not be sufficient. SEM images of cycled electrodes show the increased mechanical stability of Si-PVA nanocomposites. After a single cycle of (de)lithiation, the HEBM Si electrode surface becomes rough, and large cracks with an average width of 10.5 μm form. After 10 cycles, there is evident disintegration with over 20 μm wide cracks as the electrode layer continues to deteriorate during cycling.

However, the surface of the electrode for RBM Si-5% PVA only shows a few small cracks that are typically 2.0 μm in width. The electrode is almost undamaged from the 5 to 10 cycles. Researchers prevented pulverization with a 5% PVA coating, which increased the silicon anode cycling stability. The following factors contribute to the superior electrochemical performance:

1) Nanosized Si particles prepared by ball-milling significantly shorten the diffusion pathways of Li$^+$, resulting in enhanced kinetics.
2) Polymer coatings effectively reduce the size of primary nanoparticles.
3) Resilient PVA coatings with a robust covalent bond is adaptive to the volume changes of silicon particles. That successfully reduces the severe pulverization of Si-based anodes.

The synthesis approach features a solvent-free ball-milling process with no need for a post-processing step and low raw material cost, making it suitable for pilot plant manufacturing. Hence, the RBM technique presented in this study offers a practical solution for producing Si-based anode materials for next-generation LIBs.

In LIBs, the anode and cathode core materials are coated with protective shell materials through a ball-milling and calcination process. That improves their electrochemical performance in terms of rate capability, cycling stability, and scalability for large-scale production. The most recent studies on core–shell structures for both cathodes and anodes produced by ball-milling in LIBs are summarized in **Table 3**.

6.1.3. Spray-Drying Process

The spray-drying process, which presents the advantages of large-scale preparation, system simplicity, cost efficiency, and environmental friendliness, is often used to synthesize core–shell materials in LIBs. By rapidly evaporating the solvent with hot gas, the spray-drying process is an easy and popular technology for turning liquid solutions into solid particles. This simple one-step construction method has been successfully used to create core–shell structures, as shown in **Figure 20**.[297] The process involves the following steps[298]

1) Preparation of the solution: The solution for spray-drying process is typically prepared by mixing the core and shell materials in a solvent (water, ethanol, or propanol). The ratio of core to shell material can be adjusted to achieve the desired composition of the final product.
2) Atomization: After well mixing, the solution is pumped into an atomizer. The solution is then atomized into fine droplets using a spray nozzle, typically a high-pressure nozzle or a rotary atomizer. The droplets are typically in the range of 50–500 microns in diameter.

Table 3. Synthesis of core–shell structures of cathodes and anodes via prepared by ball-milling.

| Sample	Core material	Shell material	Condition		Electrochemical performance			Ref.
			Time of mixing [min]	Calcined in air at [°C@h]	Capacity [mAh·g^{-1}]	Capacity [mAh·g^{-1}] @1.0C	Capacity retention [% cycles^{-1}]	
Layered cathodes								
LCO@Li$_{1.5}$Al$_{0.5}$Ti$_{1.5}$(PO$_4$)$_3$	LCO	LATP	300	700@4	216@0.1C	181	73/100@0.5C	[285]
NCA@C	NCA	C	30	–	187@0.1C	175	97/80@0.2C	[232]
NMC622@ZrO$_2$	NMC622	ZrO$_2$	120	600@3	197@0.2C	175	83/100@0.5C	[240]
NMC523@C	NMC523	C	0.167	Dry-press 5 min	114@0.15C	64	33/200@1.0C	[237]
NMC811@Ca$_3$(PO$_4$)$_2$	NMC811	Ca$_3$(PO$_4$)$_2$	180	400@3	194@0.1C	180	73/150@0.3C	[289]
NMC811@Ca$_3$(PO$_4$)$_2$//Graphite					–	–	87/150@0.3C	
Spiner cathodes								
LMO@WO$_3$	LMO	WO$_3$	720	800@10	135@0.1C	120	95/100@1C	[286]
LMO@LiMnPO$_4$	LMO	LiMnPO$_4$	25	Hydrothermal 120@12	130@0.1C	–	75/30@0.1C	[290]
LNMO@SiO$_2$	LNMO	SiO$_2$	1440	900@12	130@0.5C	133	97/400@10C	[253]
LNMO@SiO$_2$//LTO					–	118	94/280@1C	
LNMO@LiPO$_3$	LNMO	LiPO$_3$	1440	760@200	130@0.1C	125	80/670@0.5C	[291]
LNMO@LiMg$_{0.5}$Mn$_{1.5}$O$_4$	LNMO	LiMg$_{0.5}$Mn$_{1.5}$O$_4$	60	800@6	132@0.2C	128	91/500@2C	[189]
Silicon anodes								
Si@Hierarchical Carbon	Si	Hierarchical carbon	300	60@12	2900@0.4A·g^{-1}	–	47/1000@2A·g^{-1}	[287]
Si@Hierarchical Carbon//LCO					2760@0.4A·g^{-1}	–	34/100@0.4A·g^{-1}	
Si@Hierarchical Carbon//LNMO					2615@0.4A·g^{-1}	–	20/100@0.4A·g^{-1}	
Si@SiO$_x$/C	Si	SiO$_x$/C	640	–	650@0.1A·g^{-1}	–	82/500@0.1A·g^{-1}	[292]
Si@FeSi$_y$/SiO$_x$	Si	FeSi$_y$/SiO$_x$	3600	120@10	1250@0.1A·g^{-1}	–	66/150@0.1A·g^{-1}	[293]
Si@SiO$_x$/C/SiC/Li$_2$SiO$_3$	Si	SiO$_x$/C/SiC/Li$_2$SiO$_3$	720	–	1924@0.1A·g^{-1}	–	75/100@0.1A·g^{-1}	[294]
Si@Cu$_3$Si	Si	Cu$_3$Si	120	600@10	2260@0.2A·g^{-1}	–	60/400@2A·g^{-1}	[295]
Si@C	Si	C	120	850@2 in N$_2$	680@0.2C	600	94/50@0.2C	[258]
Si@Graphite/void/C	Si	Graphite/void/C	360	550@5 in Ar	1800@0.1A·g^{-1}	–	50/140@0.1A·g^{-1}	[264]
Si@PVA	Si	PVA	600	–	3255@0.2A·g^{-1}	–	53/150@3A·g^{-1}	[288]
Si@PPy	Si	PPy	2400	50@8	1800@0.25mA·cm^{-2}	–	41/10@0.25mA·cm^{-2}	[296]
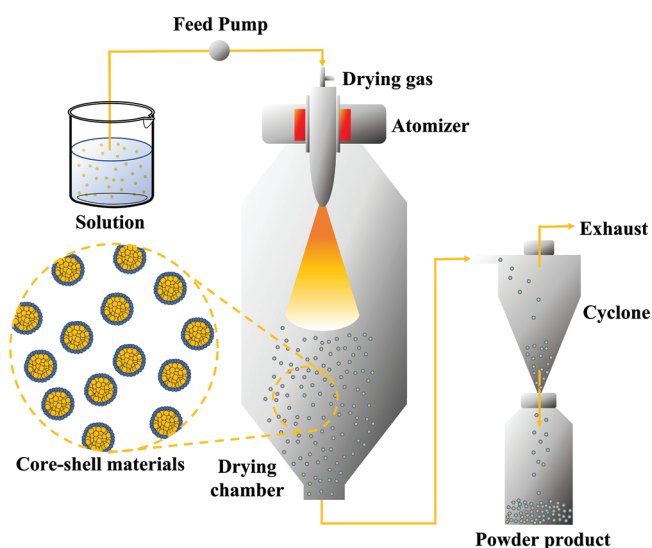
Figure 20. Schematic illustration of scalable synthesis of core–shell materials via spray-drying process.

3) Drying: The atomized droplets are then dried in a spray dryer, which typically consists of a heated chamber with a gas flow. Since there is enough moisture in each droplet to replace the liquid at the surface, the evaporation rate in the first stage is generally constant. As soon as there is not enough moisture remaining to sustain saturating conditions, the next stage begins when a dehydrated shell develops at the surface. As a result, moisture diffusion through the shell controls the evaporation rate. The droplets are then expelled into a drying gas chamber, where moisture vaporization occurs, producing dry particles. The droplets are carried through the chamber by the gas flow and are dried by hot air, forming a solid core–shell material.

4) Collection and packaging: The dried core–shell material is collected in electrostatic precipitators, bag filters, and cyclones.

5) Heat treatment: Spray-drying can also be used to thoroughly combine reactants that will later undergo a heat treatment to generate the final product. It helps to make the surface of the core–shell structure smooth and compact after the spray-drying process.

ADVANCED
SCIENCE NEWS

www.advancedsciencenews.com

small
methods

www.small-methods.com

Operational parameters impact the coating of core–shell structures through the spray-drying process.

1) Composition of the solution

The ratio of the core-to-shell material in the solution and the type of solvent and its concentration can affect the final coating properties. For example, a higher concentration of shell material in the solution can lead to thicker coatings. Using a more volatile solvent can result in a faster drying time.

2) Atomization parameters

The size and shape of the spray nozzle, as well as the pressure and flow rate of the solution, can affect the size and distribution of the atomized droplets, which in turn can influence the thickness and uniformity of the coatings.

3) Drying parameters

Inside the drying chamber, the following three drying parameters impact the core–shell structure: 1) The input air temperature influences the coating material's evaporation rate and may affect the material's properties. Higher inlet air temperatures can quicken evaporation and provide homogeneous, thicker coating layers. However, they may also result in faster degradation of the coating materials. 2) The feed rate is the amount of coating material provided to the spray dryer per unit of time. Faster feed rates can produce thicker coating layers, although this may also increase the thickness of the coated materials. 3) The humidity of the inlet air can affect the coating material's evaporation rate and the coated material's final moisture content. Higher humidity can result in slower evaporation and lower final moisture content. However, it may also increase the thickness of the coated layer.[299]

Du et al. demonstrate the enhanced performance of NCA materials via a $LiAlO_2$ coating (SDCNCA) deposited by the spray-drying process, as shown in **Figure 21**a.[300] The SEM image shows a slight change in the borders between the grains on the surface of SDCNCA particles, appearing blurred as the particles were coated with $LiAlO_2$. A coating layer with a thickness of around 10–40 nm covers the NCA material reasonably effectively. It is evident from the HR-TEM image of SDCNCA2 that the planar distance of the outer part of space differs from that of the interior part (0.2401 and 0.2449 nm, respectively). They both exhibit highly well-developed crystal lattice fringes that are neatly oriented along the (101) axes of the respective materials, NCA and $LiAlO_2$ (Figure 21b). Spray-dried materials, in particular core–shell products, are consistent, having high homogeneity, dispersion, mobility, and solubility. The rate capabilities for all samples at various C-rates between 0.1 and 5.0 C. The capabilities of the samples decrease at increasing rates.

The SDCNCA samples had similar discharge capabilities as bare NCA at low rates (<1.0 C). The SNCNCA2 delivered the maximum discharge capacity of 162 mAh·g^{-1} at 5.0 C, although those SDCNCA also showed superior capacity retention at 2.0 and 5.0 C. This is mainly attributed to the more stable structure of the coating layer throughout cycling at a room temperature of 1.0 C. The cycle life of all samples had also been investigated. The initial discharge capacity at 1.0 C delivered by the pristine NCA was 171 mAh·g^{-1}, compared with 167, 166, and 154 mAh·g^{-1} for SDCNCA1, SDCNCA2, and SDCNCA5, respectively. While the pristine NCA suffered a 31 mAh·g^{-1} capacity loss after 150 cycles, corresponding to a capacity retention of 81%. The capacity retention of the SDCNCA samples was noticeably improved, as SDCNCA1, SDCNCA2, and SDCNCA5 delivered retentions of 87%, 90%, and 93% after 150 cycles, respectively (Figure 21c).

The $LiAlO_2$ insulating layer on the NCA surface acts as a powerful inhibitor of HF-induced corrosion, preserving the structural integrity of the NCA material and noticeably enhancing its electrochemical performance. Furthermore, this layer slows down the deterioration of electrodes over time and protects the positive material from undesirable interfacial effects. The exceptional results can be attributed to the successful spray-drying process, which leads to a significant increase in structural stability. This process holds the potential to be applied to a variety of cathode materials, producing LIBs with enhanced safety and longer battery life.

Mao et al. showed a schematic synthesis diagram for V_2O_5/LiV_3O_8 coated with NCA via spray-drying and sintering process (Figure 21d).[301] The edges and corners of the cathode microparticles are gradually blurred in the SDCNCA2 SEM image when the number of coatings increases. The boundaries between the particles become blurred after a homogeneous coating has been applied to their surface, causing the particles to stick together and lose their sharp edges and corners. The interplanar spacings of the (101) and (001) crystal planes of V_2O_5 are 0.495 and 1.09 nm, respectively, while the (001) crystal plane of LiV_3O_8 has a spacing of 0.439 nm. This is due to the reactivity of V_2O_5 and the presence of residues (LiOH) on the NCA surface, as shown in Figure 21e. LiV_3O_8 is formed concurrently with the deposition of V_2O_5. The electrochemically inactive surface residues are reduced due to this process, which also enhances the positive electrode cycle life. The discharge capacity retentions of the original and coated samples are shown in Figure 21f at various rates in the range of 2.8–4.3 V.

The V_2O_5-coated sample does not function at a high rate in an ideal way. In contrast, the surface modified V_2O_5-sample significantly reduced the discharge capacities at high rates, demonstrating that improving the rate performance with a single V_2O_5 coating is challenging. These coatings can be made extremely thick, providing a robust physical barrier between the positive electrode material and the electrolyte and enhancing the cycle life. However, the performance of the material will be subpar in terms of charging and discharging rates due to the thickness of the coating, which hinders Li$^+$ diffusion during the intercalation and deintercalation process. The cycling performance of the three materials, at a current rate of 1.0 C, was evaluated between 2.8 and 4.3 V. The initial discharge-specific capacities of $1V_2O_5$@NCA and $2V_2O_5$@NCA coated with V_2O_5 are 188 and 196 mAh·g^{-1}, respectively. Unwashed coated NCA has a specific capacity of only 183 mAh·g^{-1}. At the same time, the sample coated with V_2O_5 has significantly better capacity retention. The specific discharge capacities of $1V_2O_5$@NCA and $2V_2O_5$@NCA are 147 and 163 mAh·g^{-1} after 100 cycles, respectively. Only 131 mAh·g^{-1} of uncoated NCA is present. 71%, 78%, and 83% are the corresponding capacity retentions after 100 cycles for NCA, $1V_2O_5$@NCA, and $2V_2O_5$@NCA, respectively. By preventing the active material from coming into direct contact with the

ADVANCED
SCIENCE NEWS
www.advancedsciencenews.com
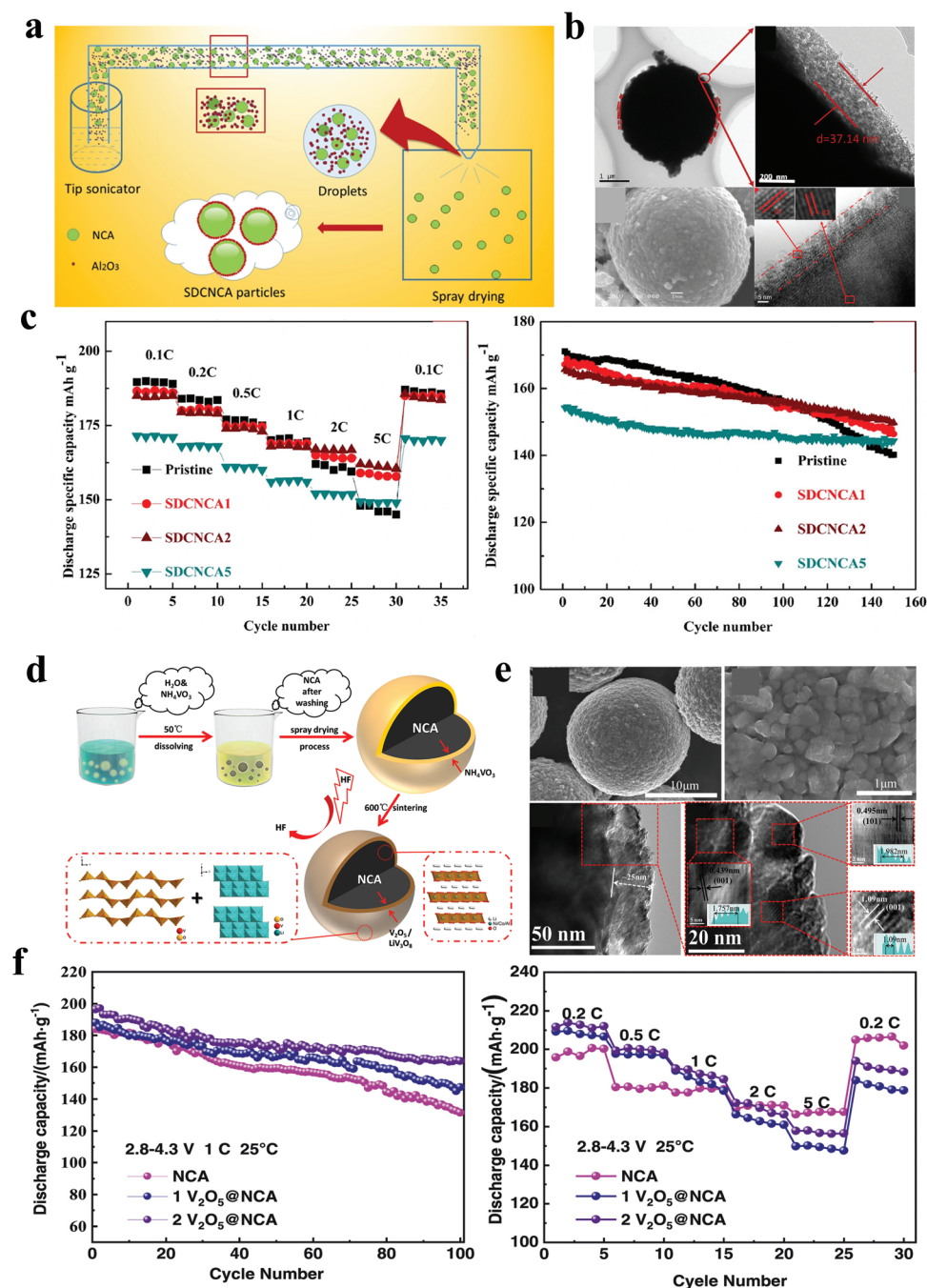
small
methods
www.small-methods.com

Figure 21. a) Schematic illustration of NCA@LiAlO$_2$ (SDCNCA2) core–shell preparation via spray-drying process. b) SEM and HR-TEM images of SDC-NCA2. c) Rate and cycling performance at room temperature of NCA and SDCNCA electrodes. Reproduced with permission.[300] Copyright 2016, American Chemical Society. d) Synthesis illustrative diagram of V$_2$O$_5$/LiV$_3$O$_8$ coated NCA (NCA@V$_2$O$_5$/LiV$_3$O$_8$) particles during spray-drying and sintering process. e) SEM and TEM images of NCA@V$_2$O$_5$/LiV$_3$O$_8$. f) Rate and cycling performance before and after coating. Reproduced with permission.[301] Copyright 2022, Elsevier.

electrolyte, the coated V$_2$O$_5$ can prevent side reactions and significantly enhance the cycle life. This improvement, in our opinion, offers great promise for the actual industrialization of nickel-rich cathode materials to be applied in LIBs.

Gao et al. have introduced a new method for modifying the surface of lithium manganese phosphate (Li–Mn–PO$_4$) using a

process that involves spray-drying and calcination, as reported in their study.[302] The SEM and TEM images of Li–Mn–PO$_4$-coated samples after calcination at 500 °C. The structure and grain size of the modified Li–Mn–PO$_4$ remains unchanged, with a size range of 100–200 nm. The surface of the grains coated with Li–Mn–PO$_4$ is comparatively rough, in contrast to those coated

**ADVANCED
SCIENCE NEWS**

www.advancedsciencenews.com
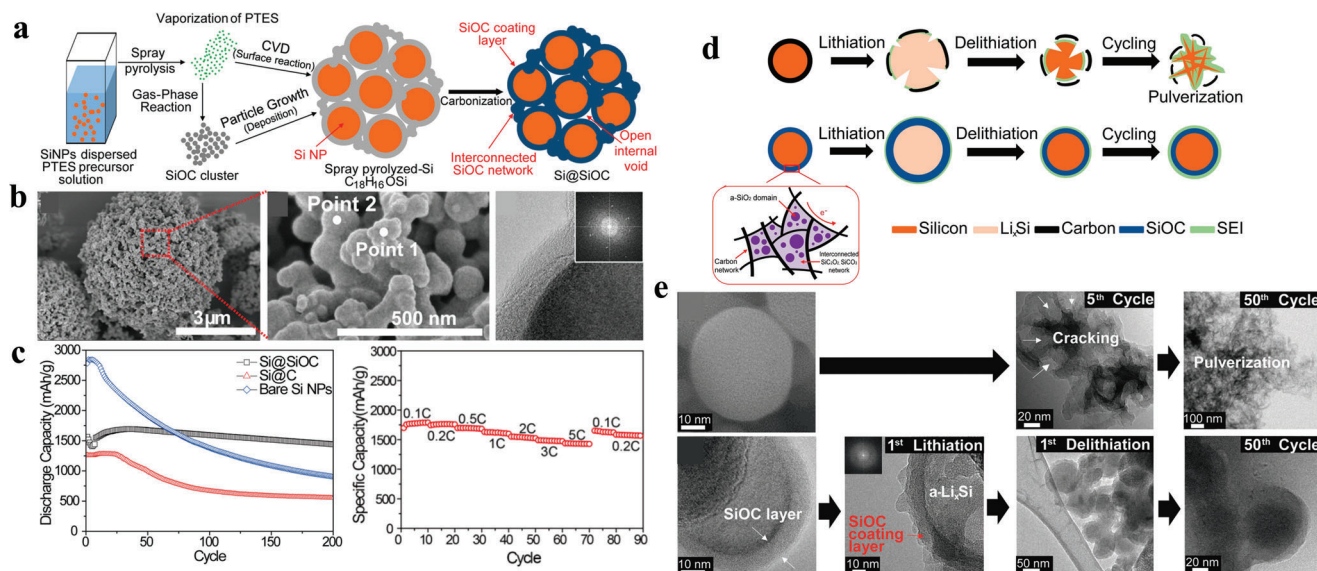
**small
methods**

www.small-methods.com

Figure 22. a) Schematic illustration of Si@SiOC core–shell preparation through vapor deposition and spray-drying process. b) SEM and HR-TEM images of Si@SiOC. c) The cycling performance of three samples was measured at a rate of 1.0 C, and the rate capability of Si@SiOC was evaluated at various C-rates ranging from 0.1 to 5.0 C. d) Graphical illustration of Si NP anodes with different coating materials during (de)lithiation. Carbon coating versus SiOC coating. (Lower inset) the internal structure of the SiOC coating material. e) TEM characterization of individual Si nanoparticles (Si NPs) for two different electrodes: bare Si NPs and Si@SiOC before and after cycling at 100 mA•g^{-1}. Reproduced with permission.[303] Copyright 2014, American Chemical Society.

with LNMO, which are smooth. Additionally, the bulk crystallographic structure, shape, and grain size of the LNMO are not significantly changed after surface coating and subsequent calcination. The cycle life and rate capability were examined before and after coating with Li–Mn–PO$_4$.

While an activation process is needed for initial discharge capacity, Li–Mn–PO$_4$ coated samples after calcination at 500 °C have outstanding cycle performance at a low current density of 0.1 C (30 mA·g^{-1}) and good discharge capacity stability. After 80 cycles, the discharge capacity of the coated sample remained at 261 mAh·g^{-1}. The strong connection between the coating and cathode surface can prevent additional HF corrosion, providing good cycling stability. High calcination temperature stabilizes the interface structure, resulting in excellent discharge capacity retention for Li–Mn–PO$_4$ coated samples. The high-rate discharge capacity of the samples at various current densities has been evaluated, and the Li–Mn–PO$_4$ coated samples after calcination at 400 and 500 °C exhibit higher discharge capacity than the as-prepared LNMO by the spray-drying method. However, the low charge transfer kinetics resulting from the strong interface interaction based on naturally poor ionic and electronic conductivity of phosphates might hinder the cycling stability of Li–Mn–PO$_4$ coated samples. Therefore, the surface coating with Li–Mn–PO$_4$ via spray-drying and calcination process at high temperatures is an effective way to enhance the electrochemical performance of LNMO cathode for LIBs.

Figure 22a schematically shows that the preparation of Si@SiOC core–shell structure through chemical vapor deposition, spray-drying, and carbonization process is suitable for large-scale production, as described by Choi and co-workers.[303] The morphology of the Si@SiOC core shell was evaluated by SEM and HR-TEM, as shown in Figure 22b. SEM established that the

secondary particles had space inside their internal structures and were made up of connected Si@SiOC nanoparticles. By using TEM, it was also confirmed that the SiOC layers exhibited conformal coatings and a framework for linking particles together. Figure 22c shows the cycle life of the three samples measured at 1.0 C and the rate capability of Si@SiOC electrodes measured at various C-rates, ranging from 0.1 to 5.0 C. Bare Si NPs started with a high capacity of 2779 mAh·g^{-1}. After 200 cycles, however, the capacity dropped dramatically to 901 mAh·g^{-1}, resulting in a low capacity retention of 33%. The initial capacity of 1266 mAh·g^{-1} for Si@C was maintained for the first 25 cycles before it abruptly decreased. Only 44% of the capacity was retained after 200 cycles.

Numerous charge-discharge cycles cause cracking and disintegration of the carbon coatings, leading to rapid capacity loss. The capacity retention of carbon layers then resembles that of bare Si NPs. In contrast, Si@SiOC retains 92% of its capacity over 200 cycles, validating the use of SiOC coatings as a design strategy. In comparison to the previous surface coating made of silica and conducting polymers, the present SiOC coating is fundamentally different because it expands more to match the volume changes of the inside Si NPs without disintegrating. The above coating is, however, not so successful in accommodating the volumetric changes of Si. The SiO$_x$ nanodomains contained by the carbon network in the SiOC surface coating and the internal free space in the micron-sized composite particles are the reasons of the excellent rate capability of Si@SiOC electrodes in the current range of 0.1–5.0 C. Figure 22d shows cycle life plots of Si NP anodes with various coating materials, including carbon and SiOC. The initial capacity fading problem of Si anodes during long-term cycling remains unresolved since the Si@C covering only the carbon is not elastic or expandable enough

2300345 (35 of 46)

**ADVANCED
SCIENCE NEWS**

www.advancedsciencenews.com

**small
methods**

www.small-methods.com

and is instead vulnerable to fracturing during the lithiation process.

On the other hand, the SiOC coating expands to some extent due to its dynamic nature in response to Li$^+$. As a result, it more robustly accommodates the volume growth of the inner Si NPs than other coating materials that experience less volume expansion. To confirm that SiOC-coatings can reduce particle cracking and pulverization during cycling, TEM measurements have been performed at different cycle numbers (Figure 22e). These images show that the severe fracturing of Si NPs might originate from Si spatially inhomogeneous volume expansion and indicate that simple nanostructuring may not address the fracture problem thoroughly after 50 cycles. At all cycling stages, including the initial 50 cycles, it was discovered that the Si@SiOC coating was very robust, maintaining grapelike core–shell structures. Once again, the robust structure of Si@SiOC is related to the capacity of SiOC to follow the volume change of inner Si NPs without disintegrating.

Shen et al. presented a scalable synthesis of silicon-graphite microspheres (Si–G) through mechanical grinding and spray-drying, as shown in **Figure 23**a: 1) commercial micron-sized silicon or graphite is reduced to nanometer-sized particles and sheets during the bead grinding process.[265] The Si–C covalent bonds strengthen the binding between silicon nanoparticles and few-layered graphite nanosheets. 2) Through the spray-drying process, the micro-sized spheres are formed by the self-assembly of the Si nanoparticles and graphite nanosheets. The production method, which uses readily available raw ingredients and a straightforward mechanical design, shows tremendous promise for the scaled-up synthesis of high-performance anodes for LIBs at low cost. The as-synthesized Si microspheres have an average diameter of around 6 μm and a homogeneous spheroidal form. The Si–G microsphere surfaces are coated with hundreds of loosely packed, homogeneous lamellar fragments, which should induce the self-assembly of S–G nanosheets. Single crystals of the (111) plane of silicon is found in HR-TEM images, showing distinct lattice fringes with a 0.313 nm spacing. Even in a broader domain, the graphite nanosheets have few layers and cover the silicon nanoparticles intimately. Si-G nanosheets are linked closely to produce a sphere of Si–G that is this size. The homogeneous distribution of silicon and carbon elements is also seen in EDS maps (Figure 23b).

The rate capability has been investigated at a current density 0.1–A·g^{-1}, and the cycle life has been determined at 0.5 A·g^{-1} for commercial Si, Si–G nanosheets, and Si–G microspheres as shown in Figure 23c. At a high current density of 4.0 A·g^{-1}, Si–G nanosheets and Si–G microspheres have higher capacities (419 and 400 mAh·g^{-1}) than commercial Si (8 mAh·g^{-1}). The rapid diffusion of Li$^+$ and transmission of e$^-$ in the composite structures are attributed to the higher rate capability when the current density reverts to 0.1 A·g^{-1}, the capacity of the Si–G microsphere electrode recovers to 2541 mAh·g^{-1}, which is higher than that of the Si–G nanosheet (2214 mAh·g^{-1}). After 500 cycles, the Si–G microspheres display the highest capacity retention of over 99% and the largest discharge capacity (1895 mAh·g^{-1}), which may be attributed to the layered graphite nanosheets that can accommodate the significant volumetric changes of silicon. The few-layered graphite nano-sheets act as a buffer layer in these microspheres and reduce the volumetric

impact and provide a conductive framework to improve electrical conductivity. Additionally, the isotropic swelling reduces the breakdown of silicon particles even more. Figure 23d shows the Si–G microsphere//NMC523 pouch-type full-cell battery and the electrochemical performance of the pouch full-cell battery. The rate capability of pouch full-cell battery was investigated at various current densities and delivers reversible capacities of 835, 814, 787, 749, and 530 mAh at 0.5, 1.0, 2.0, 3.0, and 5.0 C, respectively. A cost-effective and simple approach for commercializing a high-capacity, long-lasting silicon–graphite anode for LIBs has been demonstrated by the full-cell battery of Si–G microsphere//NMC532. The battery exhibits a capacity retention of 79.3% after 800 cycles, indicating its potential for long-term use.

Guo et al. presented the scalable synthesis of novel structure spherical Si/C granules with 3D conducting networks via a scalable spray-drying process, as shown in Figure 23e.[259] The morphology of spherical Si/C granules via the spray-drying process was evaluated by SEM and TEM (Figure 23f). Due to the polymer addiction and high solid content during the spray-drying process, the SEM image of Si/C materials shows a compact surface and interior structure with a high tap density of up to 0.91 g·cm^{-3}. While this is happening, part of the space created by solvent evaporation is still set aside so that it may support the volume expansion of Si and preserve the original structure of Si/C materials during repeated cycles. In order to prevent direct exposure of nano-Si to the electrolyte and promote the formation of stable SEI layers, the creation of a carbon-coated layer at the Si surface through pyrolysis of polymers (PVP and phenolic resin) as seen in the HR-TEM image is beneficial. The formation of homogenous suspension and the suppression of the sedimentation and agglomeration of nano-Si particles are both advantages of polymers.

In addition, PVP might serve as a thickening agent to increase the slurry viscosity, which helps to create spherical granules during the spray-drying process. At high current densities, the rate capability of Si/C anodes is greatly enhanced. When the current density is raised from 0.2 to 10 C, it maintains 85% of the initial charge capacity compared to Si/C anodes without 3D conducting networks. The exceptional rate capability is a result of the benefits provided by the excellent mechanical flexibility of graphene and super P conductive carbon black in the 3D conducting networks. This flexibility provides excellent electrical conductivity, ensuring rapid electron transport in nano-Si particles and activation of all nano-Si particles in Si/C anodes at high mass loadings. At a mass loading of 4.0 mg·cm^{-2}, the Si/C anodes exhibit excellent coulombic efficiency and cycling stability. 86% of the initial charge capacity is still present after 500 cycles, which is consistent with the excellent average CE of 99.9% from the first 10 to the last 500 cycles, which indicates the reversibility of electrode reaction. The simple method to overcome the inherent drawbacks of Si-based anodes has been successfully combined, creating 3D conducting networks and constructing porous structures. Compacted Si/C microspheres have developed 3D conducting networks based on the porous Si/C structure. The ideal Si/C anode design has a moderately porous structure, a high tap density, and a highly compelling 3D conducting framework, all of which boost electrochemical performance. The Si/C//NMC532 pouch full-cell battery presents a superior cycling performance of 87% after 100 cycles. Additionally, the pouch cell combining Si/C anode and NMC cathode could power the LED array of over
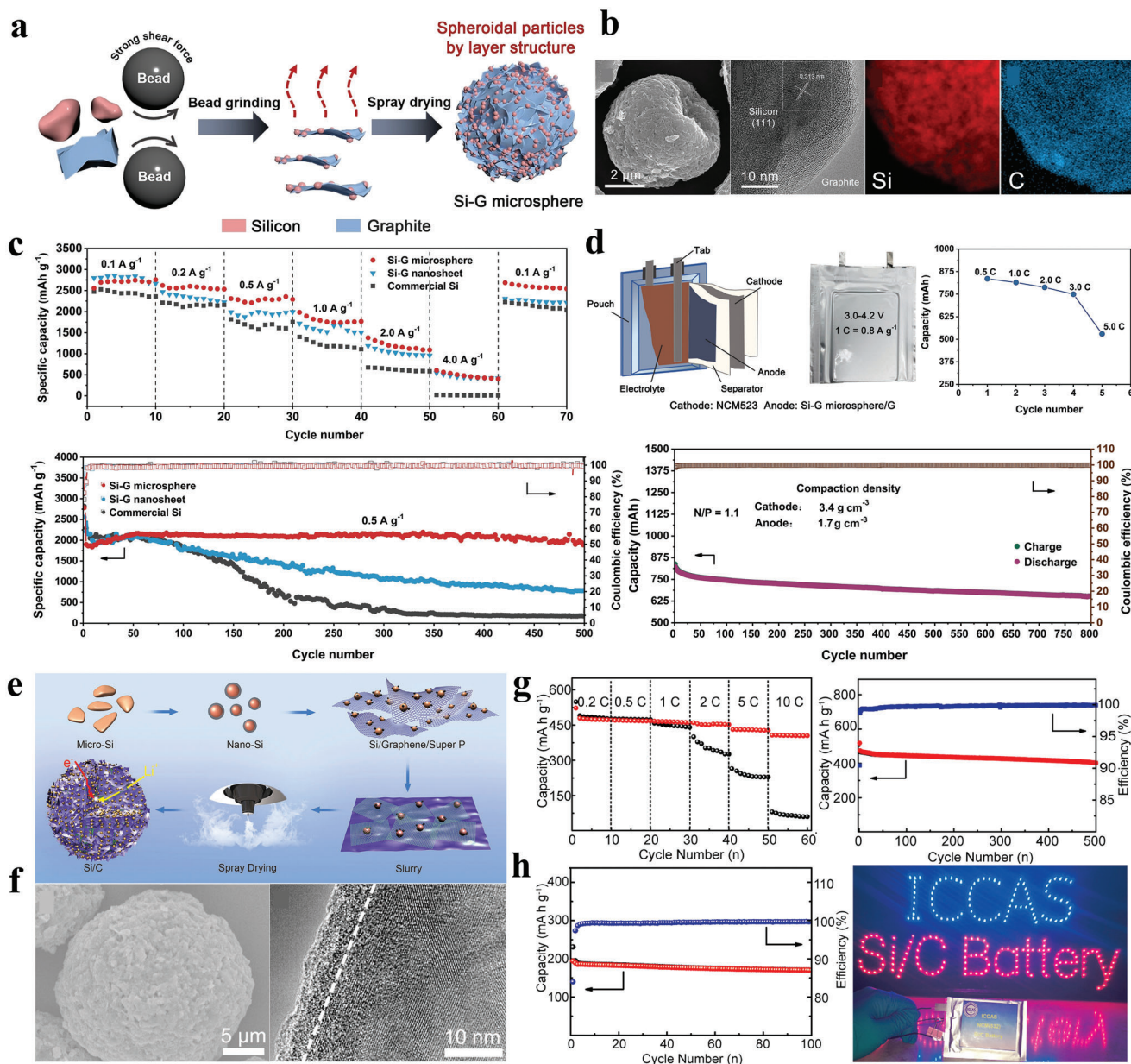
Figure 23. a) Schematic illustration of nanostructured Si-G microspheres prepared by a two-step mechanical grinding and spray-drying process. b) SEM, HR-TEM images, and EDS mapping of Si-G microsphere. c) Rate capability of commercial Si, Si–G nanosheet, and Si–G microsphere anodes at the current density varied from 0.1 to 4.0 A·g⁻¹. Cycling performance of commercial Si, Si–G nanosheet, and Si–G microsphere anodes at the current density 0.5 A·g⁻¹ during 500 cycles. d) Schematic illustration of a Si–G microsphere//NMC523 pouch-type full battery. Rate capacity and cycle life of a pouch full-cell. Reproduced with permission.[265] Copyright 2022, Wiley-VCH. e) Schematic fabrication process for spherical Si/C granules with 3D conducting networks via spray-drying process. f) SEM and HR-TEM images of spherical Si/C granules. g) Rate capability of a Si/C anode (black) without a 3D conducting network and with a 3D conducting framework (red). Cycle life and Coulombic Efficiency of Si/C anodes at 1.0 C during 500 cycles. h) Cycling performance of Si/C//NMC523 pouch full-cell at 0.2 C. LED array powered by the Si/C//NMC523 pouch full-cell. Reproduced with permission.[259] Copyright 2018, Elsevier.

220 lights for an extended time. The effective integration of Si/C anodes in next-generation LIBs is supported by studies on the excellent design and simple production method for spherical Si/C granules.

Overall, the surface of the core materials in anode and cathode core–shell structures have been coated with various protective shell layers using a spray-drying process. That has greatly improved their electrochemical performance, including rate capability and cycle life stability, as well as upscaling in the pilot plant scale. The latest studies on core–shell structures prepared through the spray-drying process are summarized in **Table 4**.

Table 4. Synthesis overview of cathode and anode core–shell structures prepared by spray-drying process.

Sample	Core material	Shell material	Condition: Shell precursor in a solvent	Spraying temperature [°C]	Calcined in O_2 at [°C@h]	Electrochemical performance: Capacity [mAh·g^{-1}]	Capacity [mAh·g^{-1}] @1.0C	Capacity retention [% cycles^{-1}]	Ref.
Layered cathodes									
LCO@LTO	LCO	LTO	Alkoxides of lithium and titanium/ethanol	–	400@0.5	$115@0.13 mA·cm^{-2}$	–	–	[304]
LCO@LTO//C		LTO/C				$48@0.13 mA·cm^{-2}$	–	–	
NCA@$LiAlO_2$	NCA	$LiAlO_2$	Al_2O_3/H_2O	180	750@12	184@0.1C	168	90/150@1C	[300]
NCA@V_2O_5/LiV_3O_8	NCA	V_2O_5/LiV_3O_8	NH_4VO_3/H_2O	–	600@5	210@0.2C	196	83/100@1C	[301]
NMC333@ZrO_2	NMC333	ZrO_2	$Zr(OC_3H_7)$/1-propanol	90	450@5	161@0.1C	139	87/40@1C	[241]
NMC333@ZrO_2	NMC333	ZrO_2	$Zr[O(CH_2)_3CH_3]_4$/ethanol	70	400@5	186@0.1C	–	152/100@0.5C	[246]
NMC333@TiO_2	NMC333	TiO_2	$Ti[O(CH_2)_3CH_3]_4$/ethanol	70	400@5	187@0.1C	–	154/100@0.5C	[305]
NMC333@Al_2O_3	NMC333	Al_2O_3	$Al(C_3H_7O)_3$/ethanol	70	400@5	182@0.1C	–	148/100@0.5C	[306]
NMC622@rGO	NMC622	rGO	GO/H_2O	200	300@5 in Ar	174@0.1C	155	96/50@0.5C	[307]
NMC135413@rGO	NMC135413	rGO	GO/H_2O	200	250@5 in N_2	247@0.1C	174	80/100@1C	
NMC333@PAALi	NMC333	PAALi	$CH_2=CHCOOH$ and $LiOH/H_2O$	–	900@12 in N_2	180@0.2C	162	93/100@1C	
Spinel cathodes									
LNMO@$LiMnPO_4$	LNMO	$LiMnPO_4$	$C_2H_3LiO_2$, $Mn(C_2H_3O_2)_2$ and $NH_4H_2PO_4/H_2O$	–	500@5	275@0.1C	187	100/80@0.1C	[302]
Silicon anodes									
Si@C	Si	C	Gelatin/H_2O	160	700@10 in Ar	$1045@0.1A·g^{-1}$	–	$32/300@0.2A·g^{-1}$	[308]
Si@C	Si	C	Lignin/H_2O	120	800@2 in Ar	$3221@0.2A·g^{-1}$	–	$71/100@0.5 A·g^{-1}$	[309]
Si@C	Si	C	Graphene and super P/H_2O	190	1000@3 in Ar	480@0.2C	460	86/500@0.2C	[259]
Si@C//NMC532	Si	C				195@0.2C	–	88/100@0.2C	
Si@Porous C	Si	Porous C	Sucrose/H_2O	500	700@0.5 in N_2	1875@0.1C	1625	91/150@2C	[310]
Si@C/C	Si	C matrix and C shell	PVP/Ethanol and H_2O	140	900@1 in Ar	$1174@0.1A·g^{-1}$	–	$87/820@1A·g^{-1}$	[311]
Si@C/C//NCA	Si					3205 mAh@0.2C	3075 mAh	81/1200@1C	
Si@C/rGO	Si	C/rGO	Sucrose and GO/H_2O	180	800@4 in H_2/Ar	$1800@0.1A·g^{-1}$	–	$99/100@0.2A·g^{-1}$	[312]
Si@Graphite	Si	Graphite	Graphite/H_2O	240	40@12	$2757@0.1A·g^{-1}$	–	$99/500@0.5A·g^{-1}$	[265]
Si@Graphite//NMC523	Si	Graphite/C				835 mAh @0.5C	787 mAh	79/800@0.5C	
Si@Graphite/C	Si	Graphite/C	Graphite and citric acid/H_2O	–	800@3 in Ar	$544@0.1A·g^{-1}$	–	$85/300@0.1A·g^{-1}$	[313]
Si@C/Graphene	Si	C/Graphene	Glucose and GO/H_2O and ethanol	195	60@3	1288@0.1C	795	52/100@0.5C	[314]
Si@SiOC	Si	SiOC	PTES/ethanol	800	800@1 in Ar	1750@0.1C	1500	92/200@1C	[303]

7. Conclusions and Outlook

This review discusses the challenges of cathode and anode materials to be applied in LIBs. These challenges can be divided into two categories: those related to layered and spinel-type of cathode materials and those related to silicon anode materials. For layered cathode materials, the challenges include adverse reactions induced by high-voltage charging, such as cation disorder, phase transition, gas release reaction, parasitic reaction, intergranular, and intragranular cracking, dissolution of transition metal ions, and thermal instability. The challenges of spinel cathode materials include the Jahn-Teller effect and the dissolution of manganese. Challenges for silicon anode materials include low electrical conductivities, high volumetric changes, materials pulverization, and the formation of unstable SEI.

The use of core–shell structures in cathode and anode materials for LIBs has gained attention as a way to improve the materials' performance and stability. These core–shell structures create a protective layer around the core material, preventing direct contact between the active core material and the electrolyte. That can enhance the electrochemical performance and improve the battery stability. This review discusses the role of different shell materials in addressing the challenges of both cathode and anode materials in LIBs.

For cathode materials, such as layered and spinel, shell materials that have been discussed include: 1) Inactive metal oxide materials. These insulating coatings help to reduce chemical reactions, metal dissolution, and parasitic reactions by preventing corrosion from hydrogen fluoride scavengers. 2) Metal fluoride materials. Such materials inhibit the rapid growth of SEI layers. They have strong ionic bonding and high ionic conductivity, which can improve the Li^+ diffusion coefficient. 3) Lithium-containing compounds. Due to their high ionic conductivity and ability to improve Li^+ transport, they enhance the rate capability of LIBs. 4) Carbon-based materials. They have high electronic conductivity and can enhance total electron transfer kinetics. 5) Conductive polymer materials. They have high electronic conductivity and structural stability and can enhance the high-rate performance and charge transfer process.

Shell materials for silicon anodes that have been reviewed include:

1) Carbon: it has good mechanical properties (softness to absorb volume changes) and electrical conductivity. That can enhance the cycling ability and kinetics of LIBs.
2) Inactive materials: they have unique properties that make it feasible to improve adhesion to conductive binders and avoid the formation of unstable SEI layers when silicon comes into direct contact with the electrolyte. Additionally, silicon particle volume expansion decreased during cycling to preserve the electrode structural integrity.
3) Metals: these materials have high mechanical strength, excellent ductility, and high electrical conductivity.
4) Conductive polymers: they also have high electrical conductivity, chemical stability, and structural stability.

Overall, core–shell structures use shell materials to enhance the cycle life of LIBs by preventing parasitic reactions from the electrolyte and volume expansion in the cathode and anode materials, respectively. In addition, core–shell structures can improve the overall conductivity and rate capability of LIBs by coating the core material with high electronic conductivity shell layers.

The synthesis techniques used to produce core–shell materials are essential for the pilot plant-scale production of LIBs. Liquid and gas phase reactions have traditionally been the most common techniques for applying coatings on cathode and anode materials. However, they have several challenges, including environmental concerns, low yields, high precursor costs, expansive reactions, and difficulty scaling up. As a result, solid phase reactions have gained attention in recent years as promising alternatives for scaling up the production of core–shell structures in LIBs. These reactions offer several benefits, including continuous operation with a high production rate, compatibility with inexpensive precursors, energy and cost savings, and an environmentally friendly approach that can be carried out at atmospheric pressure and ambient temperatures.

This review focuses on three techniques of scalable synthesis using solid-phase reactions: 1) The mechanofusion process uses mechanical coating, which relies on compression, collision, friction, and shearing forces to adhere the shell material particles to the surface of the core material particles. This coating is achieved through the convergence of the space between the fixed press head and the rotating chamber wall (high-rate operation at 1000–5000 rpm) without needing solvents and binders. However, operating parameters such as processor rotation rate, processing time, and the degree of coverage on the surface of the core material particles can affect the coating of core–shell structures. 2) The ball-milling process can synthesize a core–shell structure through the collision between the core and shell materials caused by balls. That leads to the adhering of the shell material to the core material, generated by the impact energy during the rotation movement. In addition, applying high temperatures during the calcination process in an air atmosphere after ball-milling can help smooth and compact the surface of the core–shell structure. However, the efficiency of the ball-milling process is determined by operating parameters. The ball-milling process's processor rotation rate and processing time can affect the coating as a core–shell structure. 3) The spray-drying process rapidly evaporates the solvent with hot gas, turning the mixing of the core and shell precursors in solvent solutions into dried core–shell particles. This process consists of five steps: solution preparation, atomization, drying, collection, and heat treatment. The synthesis of the core–shell structure by spray-drying process is large-scale preparation, has a simple system, is cost-efficient, and is environmentally friendly. However, the composition of the solution, atomization, and drying parameters are significant operating parameters that can affect the coating of core–shell structures for the spray-drying process.

The use of core–shell materials in LIBs has the potential to improve their performance and stability, making them more viable for large-scale applications. In addition, these materials could accelerate the transition to a low-carbon transportation system by improving the performance and lifespan of LIBs. That is critical for providing clean and efficient energy storage in electric vehicles and other clean transportation technologies. Further developments in this area will likely focus on optimizing the synthesis and performance of core–shell materials to fully realize their potential in LIBs. That will likely involve a combination of

2300345 (39 of 46)

theoretical modeling and experimental studies to optimize the design and synthesis of these materials and the scalability of synthesis techniques for producing them. Ultimately, the success of core–shell strategies in addressing the challenges of cathode and anode materials in LIBs will depend on the ability to produce these materials at a large scale in a cost-effective and environmentally friendly manner.

Conflict of Interest

The authors declare no conflict of interest.

Keywords

core–shell, layered cathodes, Li-ion batteries, scalable syntheses, silicon anodes, spinel cathodes

[1] a) M. A. Rajaeifar, P. Ghadimi, M. Raugei, Y. Wu, O. Heidrich, *Resour., Conserv. Recycl.* **2022**, *180*, 106144; b) C. Xu, Q. Dai, L. Gaines, M. Hu, A. Tukker, B. Steubing, *Commun. Mater.* **2020**, *1*, 99; c) X. Xia, P. Li, *Sci. Total Environ.* **2022**, *814*, 152870; d) J. Li, Y. Xu, Y. He, Z. Zhang, C. Zhu, X. Zhou, *J. Phys. Chem. Lett.* **2022**, *13*, 5726; e) Z. Zhang, L. Duan, Y. Xu, C. Zhao, J. Bao, J. Shen, X. Zhou, *J. Energy Chem.* **2022**, *73*, 126.

[2] a) Y. Du, W. Weng, Z. Zhang, J. He, J. Xu, J. Sun, J. Liao, J. Bao, X. Zhou, *ACS Mater. Lett.* **2021**, *3*, 356; b) Y. He, Y. Xu, J. Li, Z. Xu, Z. Zhang, J. Sun, M. Zhang, X. Zhu, X. Zhou, *Energy Fuels* **2021**, *35*, 3490; c) A. A. A.-G. S. Wageh, Q. Xu, *Acta Phys.-Chim. Sin.* **2022**, *38*, 2202001.

[3] a) J.-H. Park, J.-H. Cho, J.-S. Kim, E.-G. Shim, S.-Y. Lee, *Electrochim. Acta* **2012**, *86*, 346; b) G. Ceder, Y. M. Chiang, D. R. Sadoway, M. K. Aydinol, Y. I. Jang, B. Huang, *Nature* **1998**, *392*, 694.

[4] a) S. Kalluri, M. Yoon, M. Jo, S. Park, S. Myeong, J. Kim, S. X. Dou, Z. Guo, J. Cho, *Adv. Energy Mater.* **2017**, *7*, 1601507; b) J. L. Tebbe, A. M. Holder, C. B. Musgrave, *ACS Appl. Mater. Interfaces* **2015**, *7*, 24265.

[5] Z. Yang, R. Li, Z. Deng, *Sci. Rep.* **2018**, *8*, 863.

[6] M. D. Radin, S. Hy, M. Sina, C. Fang, H. Liu, J. Vinckeviciute, M. Zhang, M. S. Whittingham, Y. S. Meng, A. Van der Ven, *Adv. Energy Mater.* **2017**, *7*, 1602888.

[7] a) J. Qian, L. Liu, J. Yang, S. Li, X. Wang, H. L. Zhuang, Y. Lu, *Nat. Commun.* **2018**, *9*, 4918; b) G. G. Amatucci, J. M. Tarascon, L. C. Klein, *Solid State Ionics* **1996**, *83*, 167.

[8] J. Yang, M. Hou, S. Haller, Y. Wang, C. Wang, Y. Xia, *Electrochim. Acta* **2016**, *189*, 101.

[9] a) S. Laubach, S. Laubach, P. C. Schmidt, D. Ensling, S. Schmid, W. Jaegermann, A. Thißen, K. Nikolowski, H. Ehrenberg, *Phys. Chem. Chem. Phys.* **2009**, *11*, 3278; b) Z. Chen, J. Wang, D. Chao, T. Baikie, L. Bai, S. Chen, Y. Zhao, T. C. Sum, J. Lin, Z. Shen, *Sci. Rep.* **2016**, *6*, 25771.

[10] X. Tian, Y. Yi, B. Fang, P. Yang, T. Wang, P. Liu, L. Qu, M. Li, S. Zhang, *Chem. Mater.* **2020**, *32*, 9821.

[11] a) F. Lin, I. M. Markus, D. Nordlund, T.-C. Weng, M. D. Asta, H. L. Xin, M. M. Doeff, *Nat. Commun.* **2014**, *5*, 3529; b) F. Lin, D. Nordlund, I. M. Markus, T.-C. Weng, H. L. Xin, M. M. Doeff, *Energy Environ. Sci.* **2014**, *7*, 3077.

[12] J. Hong, H.-D. Lim, M. Lee, S.-W. Kim, H. Kim, S.-T. Oh, G.-C. Chung, K. Kang, *Chem. Mater.* **2012**, *24*, 2692.

[13] S. E. Renfrew, L. A. Kaufman, B. D. McCloskey, *ACS Appl. Mater. Interfaces* **2019**, *11*, 34913.

[14] a) F. Schipper, E. M. Erickson, C. Erk, J.-Y. Shin, F. F. Chesneau, D. Aurbach, *J. Electrochem. Soc.* **2016**, *164*, A6220; b) A. Manthiram, *ACS Cent. Sci.* **2017**, *3*, 1063.

[15] K. Edström, T. Gustafsson, J. O. Thomas, *Electrochim. Acta* **2004**, *50*, 397.

[16] D. Xiong, L. Ellis, J. Li, H. Li, T. Hynes, J. Allen, J. Xia, D. Hall, I. Hill, J. Dahn, *J. Electrochem. Soc.* **2017**, *164*, A3025.

[17] a) R. Jung, M. Metzger, F. Maglia, C. Stinner, H. A. Gasteiger, *J. Phys. Chem. Lett.* **2017**, *8*, 4820; b) R. Jung, M. Metzger, F. Maglia, C. Stinner, H. A. Gasteiger, *J. Electrochem. Soc.* **2017**, *164*, A1361.

[18] R. Jung, P. Strobl, F. Maglia, C. Stinner, H. A. Gasteiger, *J. Electrochem. Soc.* **2018**, *165*, A2869.

[19] a) Y.-N. Zhou, J. Ma, E. Hu, X. Yu, L. Gu, K.-W. Nam, L. Chen, Z. Wang, X.-Q. Yang, *Nat. Commun.* **2014**, *5*, 5381; b) O. Dolotko, A. Senyshyn, M. J. Mühlbauer, K. Nikolowski, H. Ehrenberg, *J. Power Sources* **2014**, *255*, 197.

[20] a) E.-J. Lee, Z. Chen, H.-J. Noh, S. C. Nam, S. Kang, D. H. Kim, K. Amine, Y.-K. Sun, *Nano Lett.* **2014**, *14*, 4873; b) H. Kim, M. G. Kim, H. Y. Jeong, H. Nam, J. Cho, *Nano Lett.* **2015**, *15*, 2111.

[21] J. Li, L. E. Downie, L. Ma, W. Qiu, J. R. Dahn, *J. Electrochem. Soc.* **2015**, *162*, A1401.

[22] a) L. Mu, R. Lin, R. Xu, L. Han, S. Xia, D. Sokaras, J. D. Steiner, T.-C. Weng, D. Nordlund, M. M. Doeff, Y. Liu, K. Zhao, H. L. Xin, F. Lin, *Nano Lett.* **2018**, *18*, 3241; b) Z. Xu, Z. Jiang, C. Kuai, R. Xu, C. Qin, Y. Zhang, M. M. Rahman, C. Wei, D. Nordlund, C.-J. Sun, X. Xiao, X.-W. Du, K. Zhao, P. Yan, Y. Liu, F. Lin, *Nat. Commun.* **2020**, *11*, 83; c) P. Yan, J. Zheng, T. Chen, L. Luo, Y. Jiang, K. Wang, M. Sui, J.-G. Zhang, S. Zhang, C. Wang, *Nat. Commun.* **2018**, *9*, 2437.

[23] W. Li, *J. Electrochem. Soc.* **2020**, *167*, 090514.

[24] C. Zhan, J. Lu, A. Jeremy Kropf, T. Wu, A. N. Jansen, Y.-K. Sun, X. Qiu, K. Amine, *Nat. Commun.* **2013**, *4*, 2437.

[25] a) X. Xiao, Z. Liu, L. Baggetto, G. M. Veith, K. L. More, R. R. Unocic, *Phys. Chem. Chem. Phys.* **2014**, *16*, 10398; b) J. Wandt, A. Freiberg, R. Thomas, Y. Gorlin, A. Siebel, R. Jung, H. A. Gasteiger, M. Tromp, *J. Mater. Chem. A* **2016**, *4*, 18300.

[26] a) D. R. Gallus, R. Schmitz, R. Wagner, B. Hoffmann, S. Nowak, I. Cekic-Laskovic, R. W. Schmitz, M. Winter, *Electrochim. Acta* **2014**, *134*, 393; b) I. Buchberger, S. Seidlmayer, A. Pokharel, M. Piana, J. Hattendorff, P. Kudejova, R. Gilles, H. A. Gasteiger, *J. Electrochem. Soc.* **2015**, *162*, A2737.

[27] a) S. Sharifi-Asl, J. Lu, K. Amine, R. Shahbazian-Yassar, *Adv. Energy Mater.* **2019**, *9*, 1900551; b) J. Geder, H. E. Hoster, A. Jossen, J. Garche, D. Y. W. Yu, *J. Power Sources* **2014**, *257*, 286.

[28] O. Tsutomu, M. Yoshinari, *Chem. Lett.* **2001**, *30*, 642.

[29] a) R. Qi, J.-L. Shi, X.-D. Zhang, X.-X. Zeng, Y.-X. Yin, J. Xu, L. Chen, W.-G. Fu, Y.-G. Guo, L.-J. Wan, *Sci. China: Chem.* **2017**, *60*, 1230; b) Y. Wang, J. Jiang, J. R. Dahn, *Electrochem. Commun.* **2007**, *9*, 2534.

[30] S.-M. Bak, E. Hu, Y. Zhou, X. Yu, S. D. Senanayake, S.-J. Cho, K.-B. Kim, K. Y. Chung, X.-Q. Yang, K.-W. Nam, *ACS Appl. Mater. Interfaces* **2014**, *6*, 22594.

[31] M. Dixit, B. Markovsky, F. Schipper, D. Aurbach, D. T. Major, *J. Phys. Chem. C* **2017**, *121*, 22628.

[32] a) J. Duan, X. Tang, H. Dai, Y. Yang, W. Wu, X. Wei, Y. Huang, *Electrochem. Energy Rev.* **2020**, *3*, 43; b) L. Jiang, Q. Wang, J. Sun, *J. Hazard. Mater.* **2018**, *351*, 260.

[33] K. Ragavendran, H. Xia, P. Mandal, A. K. Arof, *Phys. Chem. Chem. Phys.* **2017**, *19*, 2073.

[34] K. Y. Chung, H. S. Lee, W.-S. Yoon, J. McBreen, X.-Q. Yang, *J. Electrochem. Soc.* **2006**, *153*, A774.

[35] Y. Tesfamhret, H. Liu, Z. Chai, E. Berg, R. Younesi, *ChemElectroChem* **2021**, *8*, 1516.

[36] a) L. Yang, M. Takahashi, B. Wang, *Electrochim. Acta* **2006**, *51*, 3228; b) D. Aurbach, *J. Power Sources* **2000**, *89*, 206.

[37] Y. Zhang, H. Xie, H. Jin, Q. Zhang, Y. Li, X. Li, K. Li, C. Bao, *IOP Conf. Series: Earth Environ. Sci.* **2020**, *603*, 012051.

[38] a) T. Yi, J. Mei, Y.-R. Zhu, *J. Power Sources* **2016**, *316*, 85; b) J. Li, L. Wang, L. Wang, J. Luo, J. Gao, J. Li, J. Wang, X. He, G. Tian, S. Fan, *J. Power Sources* **2013**, *244*, 652.

[39] C. Liu, J. Yuan, R. Masse, X. Jia, W. Bi, Z. Neale, T. Shen, M. Xu, M. Tian, J. Zheng, J. Tian, G. Cao, *Adv. Mater.* **2021**, *33*, 1905245.

[40] a) J. Lu, K. S. Lee, *Mater. Technol.* **2016**, *31*, 628; b) J. Ma, P. Hu, G. Cui, L. Chen, *Chem. Mater.* **2016**, *28*, 3578.

[41] H. Xu, H. Zhang, J. Ma, G. Xu, T. Dong, J. Chen, G. Cui, *ACS Energy Lett.* **2019**, *4*, 2871.

[42] a) C. Zhan, T. Wu, J. Lu, K. Amine, *Energy Environ. Sci.* **2018**, *11*, 243; b) Y. Xia, Y. Zhou, M. Yoshio, *J. Electrochem. Soc.* **1997**, *144*, 2593.

[43] H. Tsunekawa, A. S. Tanimoto, R. Marubayashi, M. Fujita, K. Kifune, M. Sano, *J. Electrochem. Soc.* **2002**, *149*, A1326.

[44] C. Delacourt, A. Kwong, X. Liu, R. Qiao, W. L. Yang, P. Lu, S. J. Harris, V. Srinivasan, *J. Electrochem. Soc.* **2013**, *160*, A1099.

[45] a) K. Stokes, G. Flynn, H. Geaney, G. Bree, K. M. Ryan, *Nano Lett.* **2018**, *18*, 5569; b) S. Chae, M. Ko, K. Kim, K. Ahn, J. Cho, *Joule* **2017**, *1*, 47.

[46] a) W. Luo, X. Chen, Y. Xia, M. Chen, L. Wang, Q. Wang, W. Li, J. Yang, *Adv. Energy Mater.* **2017**, *7*, 1701083; b) S. Chae, S.-H. Choi, N. Kim, J. Sung, J. Cho, *Angew. Chem., Int. Ed.* **2020**, *59*, 110; c) X. Zhao, V.-P. Lehto, *Nanotechnology* **2020**, *32*, 042002.

[47] a) J. B. Quinn, T. Waldmann, K. Richter, M. Kasper, M. Wohlfahrt-Mehrens, *J. Electrochem. Soc.* **2018**, *165*, A3284; b) M. Saito, K. Nakai, T. Yamada, T. Takenaka, M. Hirota, A. Kamei, A. Tasaka, M. Inaba, *J. Power Sources* **2011**, *196*, 6637.

[48] a) B. Zhu, X. Wang, P. Yao, J. Li, J. Zhu, *Chem. Sci.* **2019**, *10*, 7132; b) A. Casimir, H. Zhang, O. Ogoke, J. C. Amine, J. Lu, G. Wu, *Nano Energy* **2016**, *27*, 359.

[49] a) K. Ogata, S. Jeon, D. S. Ko, I. S. Jung, J. H. Kim, K. Ito, Y. Kubo, K. Takei, S. Saito, Y. H. Cho, H. Park, J. Jang, H. G. Kim, J. H. Kim, Y. S. Kim, W. Choi, M. Koh, K. Uosaki, S. G. Doo, Y. Hwang, S. Han, *Nat. Commun.* **2018**, *9*, 479; f) F. Wu, J. Maier, Y. Yu, *Chem. Soc. Rev.* **2020**, *49*, 1569; c) G. G. Eshetu, E. Figgemeier, *ChemSusChem* **2019**, *12*, 2515.

[50] a) R. Dash, S. Pannala, *Sci. Rep.* **2016**, *6*, 27449; b) D. Reyter, S. Rousselot, D. Mazouzi, M. Gauthier, P. Moreau, B. Lestriez, D. Guyomard, L. Roué, *J. Power Sources* **2013**, *239*, 308.

[51] H. Wu, G. Chan, J. W. Choi, I. Ryu, Y. Yao, M. T. McDowell, S. W. Lee, A. Jackson, Y. Yang, L. Hu, Y. Cui, *Nat. Nanotechnol.* **2012**, *7*, 310.

[52] a) P. Verma, P. Maire, P. Novák, *Electrochim. Acta* **2010**, *55*, 6332; b) V. A. Agubra, J. W. Fergus, *J. Power Sources* **2014**, *268*, 153.

[53] a) H. Wu, Y. Cui, *Nano Today* **2012**, *7*, 414; b) R. Kumar, A. Tokranov, B. W. Sheldon, X. Xiao, Z. Huang, C. Li, T. Mueller, *ACS Energy Lett.* **2016**, *1*, 689.

[54] a) J. H. Ryu, J. W. Kim, Y. E. Sung, S. M. Oh, *Electrochem. Solid-State Lett.* **2004**, *7*, A306; b) C.-M. Park, J.-H. Kim, H. Kim, H.-J. Sohn, *Chem. Soc. Rev.* **2010**, *39*, 3115.

[55] a) P. Oh, S.-M. Oh, W. Li, S. Myeong, J. Cho, A. Manthiram, *Adv. Sci.* **2016**, *3*, 1600184; b) H. Shi, X. Wang, P. Hou, E. Zhou, J. Guo, J. Zhang, D. Wang, F. Guo, D. Song, X. Shi, L. Zhang, *J. Alloys Compd.* **2014**, *587*, 710; c) W. Bao, G. Qian, L. Zhao, Y. Yu, L. Su, X. Cai, H. Zhao, Y. Zuo, Y. Zhang, H. Li, Z. Peng, L. Li, J. Xie, *Nano Lett.* **2020**, *20*, 8832; d) K. Park, D. J. Ham, S. Y. Park, J. Jang, D.-H. Yeon,

S. Moon, S. J. Ahn, *RSC Adv.* **2020**, *10*, 26756; e) Y. Gao, J. Park, X. Liang, *ACS Appl. Energy Mater.* **2020**, *3*, 8978; f) F. Schipper, M. Dixit, D. Kovacheva, M. Talianker, O. Haik, J. Grinblat, E. M. Erickson, C. Ghanty, D. T. Major, B. Markovsky, D. Aurbach, *J. Mater. Chem. A* **2016**, *4*, 16073.

[56] a) S. Liu, Z. Dang, D. Liu, C. Zhang, T. Huang, A. Yu, *J. Power Sources* **2018**, *396*, 288; b) Y. Kim, *Int. J. Quantum Chem.* **2019**, *119*, e26028; c) H.-H. Ryu, B. Namkoong, J.-H. Kim, I. Belharouak, C. S. Yoon, Y.-K. Sun, *ACS Energy Lett.* **2021**, *6*, 2726.

[57] a) J. Cho, Y. J. Kim, T.-J. Kim, B. Park, *Angew. Chem., Int. Ed.* **2001**, *40*, 3367; b) C. Li, H. P. Zhang, L. J. Fu, H. Liu, Y. P. Wu, E. Rahm, R. Holze, H. Q. Wu, *Electrochim. Acta* **2006**, *51*, 3872.

[58] a) H.-J. Kweon, J. Park, J. Seo, G. Kim, B. Jung, H. S. Lim, *J. Power Sources* **2004**, *126*, 156; b) A. Zhou, Q. Liu, Y. Wang, W. Wang, X. Yao, W. Hu, L. Zhang, X. Yu, J. Li, H. Li, *J. Mater. Chem. A* **2017**, *5*, 24361.

[59] a) J.-H. Shim, S. Lee, S. S. Park, *Chem. Mater.* **2014**, *26*, 2537; b) Y. Iriyama, H. Kurita, I. Yamada, T. Abe, Z. Ogumi, *J. Power Sources* **2004**, *137*, 111.

[60] a) C. Hudaya, J. H. Park, J. K. Lee, W. Choi, *Solid State Ionics* **2014**, *256*, 89; b) M. A. Poyner, I. Jayasekara, D. Teeters, *MRS Adv.* **2016**, *1*, 3075.

[61] a) W. Chang, J.-W. Choi, J.-C. Im, J. K. Lee, *J. Power Sources* **2010**, *195*, 320; b) G. Kaur, B. D. Gates, *J. Electrochem. Soc.* **2022**, *169*, 043504.

[62] a) Q. Hao, C. Xu, S. Jia, X. Zhao, *Electrochim. Acta* **2013**, *113*, 439; b) Y. N. Lee, Y. S. Yoon, *J. Nucl. Sci. Technol.* **2016**, *53*, 1178.

[63] a) H. Miyashiro, A. Yamanaka, M. Tabuchi, S. Seki, M. Nakayama, Y. Ohno, Y. Kobayashi, Y. Mita, A. Usami, M. Wakihara, *J. Electrochem. Soc.* **2006**, *153*, A348; b) Z. Chen, J. R. Dahn, *Electrochem. Solid-State Lett.* **2004**, *7*, A11.

[64] a) H.-M. Cheng, F.-M. Wang, J. P. Chu, R. Santhanam, J. Rick, S.-C. Lo, *J. Phys. Chem. C* **2012**, *116*, 7629; b) F. Wang, Y. Jiang, S. Lin, W. Wang, C. Hu, Y. Wei, B. Mao, C. Liang, *Electrochim. Acta* **2019**, *295*, 1017.

[65] Y. Orikasa, D. Takamatsu, K. Yamamoto, Y. Koyama, S. Mori, T. Masese, T. Mori, T. Minato, H. Tanida, T. Uruga, Z. Ogumi, Y. Uchimoto, *Adv. Mater. Interfaces* **2014**, *1*, 1400195.

[66] Z. Fei, S. Zhou, Y. Zhang, Q. Meng, P. Dong, Y. Li, J. Fei, H. Qi, J. Yan, X. Zhao, *ACS Sustainable Chem. Eng.* **2022**, *10*, 6853.

[67] J. Xie, J. Zhao, Y. Liu, H. Wang, C. Liu, T. Wu, P.-C. Hsu, D. Lin, Y. Jin, Y. Cui, *Nano Res.* **2017**, *10*, 3754.

[68] T. Teranishi, M. Inohara, J. Kano, H. Hayashi, A. Kishimoto, K. Yoda, H. Motobayashi, Y. Tasaki, *Solid State Ionics* **2018**, *314*, 57.

[69] C.-W. Wang, Y. Zhou, J.-H. You, J.-D. Chen, Z. Zhang, S.-J. Zhang, C.-G. Shi, W.-D. Zhang, M.-H. Zou, Y. Yu, J.-T. Li, L.-Y. Zeng, L. Huang, S.-G. Sun, *ACS Appl. Energy Mater.* **2020**, *3*, 2593.

[70] J. Xie, A. D. Sendek, E. D. Cubuk, X. Zhang, Z. Lu, Y. Gong, T. Wu, F. Shi, W. Liu, E. J. Reed, Y. Cui, *ACS Nano* **2017**, *11*, 7019.

[71] M. Wang, X. Feng, H. Xiang, Y. Feng, C. Qin, P. Yan, Y. Yu, *Small Methods* **2019**, *3*, 1900355.

[72] M. Fingerle, R. Buchheit, S. Sicolo, K. Albe, R. Hausbrand, *Chem. Mater.* **2017**, *29*, 7675.

[73] K. Park, B.-C. Yu, J.-W. Jung, Y. Li, W. Zhou, H. Gao, S. Son, J. B. Goodenough, *Chem. Mater.* **2016**, *28*, 8051.

[74] S. Takai, M. Kamata, S. Fujine, K. Yoneda, K. Kanda, T. Esaka, *Solid State Ionics* **1999**, *123*, 165.

[75] a) Y. Sun, H. Dong, K. Wu, X. Chen, S. Wang, W. Gu, Z. Hong, M. Liu, Y. Shen, W. Lu, *J. Electroanal. Chem.* **2020**, *866*, 114109; b) X. Yu, A. Manthiram, *Energy Environ. Sci.* **2018**, *11*, 527.

[76] J. Lin, C. Zeng, Y. Chen, X. Lin, C. Xu, C.-Y. Su, *J. Mater. Chem. A* **2020**, *8*, 6607.

[77] Z. Chen, Y. Qin, K. Amine, Y. K. Sun, *J. Mater. Chem.* **2010**, *20*, 7606.

[78] Y.-K. Sun, S.-T. Myung, B.-C. Park, J. Prakash, I. Belharouak, K. Amine, *Nat. Mater.* **2009**, *8*, 320.

2300345 (41 of 46)

ADVANCED
SCIENCE NEWS

www.advancedsciencenews.com

small
methods

www.small-methods.com

[79] a) D. Weber, Đ. Tripković, K. Kretschmer, M. Bianchini, T. Brezesinski, *Eur. J. Inorg. Chem.* **2020**, *2020*, 3117; b) G. Hu, J. Fan, Y. Lu, Y. Zhang, K. Du, Z. Peng, L. Li, B. Zhang, Y. Shi, Y. Cao, *ChemSusChem* **2020**, *13*, 5699; c) S. Xia, W. Huang, X. Shen, J. Liu, F. Cheng, J.-J. Liu, X. Yang, H. Guo, *J. Energy Chem.* **2020**, *45*, 110.

[80] Y. Su, G. Chen, L. Chen, Q. Li, Y. Lu, L. Bao, N. Li, S. Chen, F. Wu, *Chin. J. Chem.* **2020**, *38*, 1817.

[81] a) B. Wu, J. Bi, Q. Liu, D. Mu, L. Wang, J. Fu, F. Wu, *Electrochim. Acta* **2019**, *298*, 609; b) B. Xiao, X. Sun, *Adv. Energy Mater.* **2018**, *8*, 1802057.

[82] a) L. de Biasi, B. Schwarz, T. Brezesinski, P. Hartmann, J. Janek, H. Ehrenberg, *Adv. Mater.* **2019**, *31*, 1900985; b) S. Schweidler, L. de Biasi, G. Garcia, A. Mazilkin, P. Hartmann, T. Brezesinski, J. Janek, *ACS Appl. Energy Mater.* **2019**, *2*, 7375.

[83] a) R. Jung, R. Morasch, P. Karayaylali, K. Phillips, F. Maglia, C. Stinner, Y. Shao-Horn, H. A. Gasteiger, *J. Electrochem. Soc.* **2018**, *165*, A132; b) T. Hatsukade, A. Schiele, P. Hartmann, T. Brezesinski, J. Janek, *ACS Appl. Mater. Interfaces* **2018**, *10*, 38892.

[84] J. Cabana, B. J. Kwon, L. Hu, *Acc. Chem. Res.* **2018**, *51*, 299.

[85] J. A. Gilbert, V. A. Maroni, Y. Cui, D. J. Gosztola, D. J. Miller, D. P. Abraham, *Adv. Mater. Interfaces* **2018**, *5*, 1701447.

[86] W. Liu, X. Li, D. Xiong, Y. Hao, J. Li, H. Kou, B. Yan, D. Li, S. Lu, A. Koo, K. Adair, X. Sun, *Nano Energy* **2018**, *44*, 111.

[87] a) S. Neudeck, A. Mazilkin, C. Reitz, P. Hartmann, J. Janek, T. Brezesinski, *Sci. Rep.* **2019**, *9*, 5328; b) D. S. Hall, R. Gauthier, A. Eldesoky, V. S. Murray, J. R. Dahn, *ACS Appl. Mater. Interfaces* **2019**, *11*, 14095.

[88] a) M. Rastgoo-Deylami, M. Javanbakht, H. Omidvar, *Solid State Ionics* **2019**, *331*, 74; b) H. Gao, J. Cai, G.-L. Xu, L. Li, Y. Ren, X. Meng, K. Amine, Z. Chen, *Chem. Mater.* **2019**, *31*, 2723.

[89] K. Min, K. Park, S. Y. Park, S.-W. Seo, B. Choi, E. Cho, *J. Electrochem. Soc.* **2018**, *165*, A79.

[90] W. Luo, B. Zheng, *Appl. Surf. Sci.* **2017**, *404*, 310.

[91] M. R. Laskar, D. H. K. Jackson, S. Xu, R. J. Hamers, D. Morgan, T. F. Kuech, *ACS Appl. Mater. Interfaces* **2017**, *9*, 11231.

[92] a) Y. Liu, X. Wang, J. Cai, X. Han, D. Geng, J. Li, X. Meng, *J. Mater. Sci. Technol.* **2020**, *54*, 77; b) U. Nisar, R. Petla, S. A. Jassim Al-Hail, A. A. Quddus, H. Monawwar, A. Shakoor, R. Essehli, R. Amin, *RSC Adv.* **2020**, *10*, 15274.

[93] a) S. Hildebrand, C. Vollmer, M. Winter, F. M. Schappacher, *J. Electrochem. Soc.* **2017**, *164*, A2190; b) C. Chen, T. Tao, W. Qi, H. Zeng, Y. Wu, B. Liang, Y. Yao, S. Lu, Y. Chen, *J. Alloys Compd.* **2017**, *709*, 708.

[94] X. Yan, L. Chen, S. A. Shah, J. Liang, Z. Liu, *Electrochim. Acta* **2017**, *249*, 179.

[95] S. Dong, Y. Zhou, C. Hai, J. Zeng, Y. Sun, Y. Shen, X. Li, X. Ren, G. Qi, X. Zhang, L. Ma, *Ceram. Int.* **2019**, *45*, 144.

[96] a) Q. Zhang, L. Wang, C. Zhu, Z. Sun, W. Cheng, D. Lv, W. Ren, L. Bian, J. Xu, A. Chang, *ChemElectroChem* **2017**, *4*, 1199; b) H. Y. Jeong, J. H. Jung, D. Chan Seok, S. Yoo, S. K. Kwon, D. Han, *Curr. Appl. Phys.* **2018**, *18*, 961.

[97] a) G.-R. Hu, X. Qi, H. Kaihua, X. Lai, X. Zhang, K. Du, Z. Peng, Y. Cao, *Electrochim. Acta* **2018**, *265*, 391; b) G. Hu, X. Qi, K. Hu, X. Lai, X. Zhang, K. Du, Z. Peng, Y. Cao, *Electrochim. Acta* **2018**, *265*, 391.

[98] S. Dai, G. Yan, L. Wang, L. Luo, Y. Li, Y. Yang, H. Liu, Y. Liu, M. Yuan, *J. Electroanal. Chem.* **2019**, *847*, 113197.

[99] W. Liu, X. Tang, M. Qin, G. Li, J. Deng, X. Huang, *Mater. Lett.* **2016**, *185*, 96.

[100] S. Sun, N. Wan, Q. Wu, X. Zhang, D. Pan, Y. Bai, X. Lu, *Solid State Ionics* **2015**, *278*, 85.

[101] a) K. Park, J.-H. Park, B. Choi, J. H. Kim, S.-G. Hong, H. N. Han, *Electrochim. Acta* **2017**, *257*, 217; b) Y. Wu, H. Ming, M. Li, J. Zhang, W. Wahyudi, L. Xie, X. He, J. Wang, Y. Wu, J. Ming, *ACS Energy Lett.* **2019**, *4*, 656.

[102] Z.-F. Tang, R. Wu, P.-F. Huang, Q.-S. Wang, C.-H. Chen, *J. Alloys Compd.* **2017**, *693*, 1157.

[103] a) K. Min, K. Park, S. Park, S.-W. Seo, B. Choi, E. Cho, *Sci. Rep.* **2017**, *7*, 7151; b) Z. Chen, G.-T. Kim, Y. Guang, D. Bresser, T. Diemant, Y. Huang, M. Copley, R. J. Behm, S. Passerini, Z. Shen, *J. Power Sources* **2018**, *402*, 263.

[104] a) X. Jiang, *Int. J. Electrochem. Sci.* **2018**, *13*, 2341; b) D. J. Xiong, T. Hynes, L. D. Ellis, J. R. Dahn, *J. Electrochem. Soc.* **2017**, *164*, A3174.

[105] S. Xia, F. Li, F. Chen, H. Guo, *J. Alloys Compd.* **2018**, *731*, 428.

[106] D.-J. Lee, B. Scrosati, Y.-K. Sun, *J. Power Sources* **2011**, *196*, 7742.

[107] M. A. Razmjoo Khollari, M. K. Azar, M. Esmaeili, N. Malekpour, S. M. Hosseini-Hosseinabad, R. S. Moakhar, A. Dolati, S. Ramakrishna, *ACS Appl. Energy Mater.* **2021**, *4*, 5304.

[108] a) P. Zhang, L. Zhang, X. Ren, Q. Yuan, J. Liu, Q. Zhang, *Lancet* **2011**, *161*, 1092; b) P. Zhang, L. Zhang, X. Ren, Q. Yuan, J. Liu, Q. Zhang, *Synth. Met.* **2011**, *161*, 1092.

[109] S. H. Ju, I.-S. Kang, Y.-S. Lee, W.-K. Shin, S. Kim, K. Shin, D.-W. Kim, *ACS Appl. Mater. Interfaces* **2014**, *6*, 2546.

[110] Y. Cao, X. Qi, K. Hu, Y. Wang, Z. Gan, Y. Li, G. Hu, Z. Peng, K. Du, *ACS Appl. Mater. Interfaces* **2018**, *10*, 18270.

[111] Q. Gan, N. Qin, Y. Zhu, Z. Huang, F. Zhang, S. Gu, J. Xie, K. Zhang, L. Lu, Z. Lu, *ACS Appl. Mater. Interfaces* **2019**, *11*, 12594.

[112] H. Wang, J. Lin, X. Zhang, L. Wang, J. Yang, E. Fan, F. Wu, R. Chen, L. Li, *ACS Appl. Energy Mater.* **2021**, *4*, 6205.

[113] a) Z. Chen, Z. Zhang, P. Liu, S. Wang, W. Zhang, D. Chen, *J. Alloys Compd.* **2019**, *780*, 643; b) C. Zhu, J. Chen, S. Liu, B. Cheng, Y. Xu, P. Zhang, Q. Zhang, Y. Li, S. Zhong, *J. Mater. Sci.* **2018**, *53*, 5242.

[114] a) X. Chen, F. Ma, Y. Li, J. Liang, B. Matthews, J. Sokolowski, J. Han, G. Wu, X. Lu, Q. Li, *Electrochim. Acta* **2018**, *284*, 526; b) Z. Ye, L. Qiu, W. Yang, Z. Wu, Y. Liu, G. Wang, Y. Song, B. Zhong, X. Guo, *Chemistry* **2021**, *27*, 4249.

[115] a) I. H. Son, J. H. Park, S. Park, K. Park, S. Han, J. Shin, S.-G. Doo, Y. Hwang, H. Chang, J. W. Choi, *Nat. Commun.* **2017**, *8*, 1561; b) S. Vadivel, N. Phattharasupakun, J. Wutthiprom, S. duangdangchote, M. Sawangphruk, *ACS Appl. Mater. Interfaces* **2019**, *11*, 30719.

[116] L.-L. Zhang, J.-Q. Wang, X.-L. Yang, G. Liang, T. Li, P.-L. Yu, D. Ma, *ACS Appl. Mater. Interfaces* **2018**, *10*, 11663.

[117] a) P. Zou, Z. Lin, M. Fan, F. Wang, Y. Liu, X. Xiong, *Appl. Surf. Sci.* **2020**, *504*, 144506; b) K. Sahni, M. Ashuri, Q. He, R. Sahore, I. D. Bloom, Y. Liu, J. A. Kaduk, L. L. Shaw, *Electrochim. Acta* **2019**, *301*, 8.

[118] a) Z. Peng, G. Yang, F. Li, Z. Zhu, Z. Liu, *J. Alloys Compd.* **2018**, *762*, 827; b) G. Hu, M. Zhang, L. Wu, Z. Peng, K. Du, Y. Cao, *J. Alloys Compd.* **2017**, *690*, 589.

[119] a) H. Liang, Z. Wang, H. Guo, J. Wang, J. Leng, *Appl. Surf. Sci.* **2017**, *423*, 1045; b) B. Song, W. Li, S.-M. Oh, A. Manthiram, *ACS Appl. Mater. Interfaces* **2017**, *9*, 9718.

[120] a) Z. Xiao, C. Hu, L. Song, L. Li, Z. Cao, H. Zhu, J. Liu, X. Li, F. Tang, *Ionics* **2018**, *24*, 91; b) W. Tang, Z. Chen, F. Xiong, F. Chen, C. Huang, Q. Gao, T. Wang, Z. Yang, W. Zhang, *J. Power Sources* **2019**, *412*, 246.

[121] G. V. Zhuang, G. Chen, J. Shim, X. Song, P. N. Ross, T. J. Richardson, *J. Power Sources* **2004**, *134*, 293.

[122] C. S. Johnson, J.-S. Kim, A. Jeremy Kropf, A. J. Kahaian, J. T. Vaughey, M. M. Thackeray, *Electrochem. Commun.* **2002**, *4*, 492.

[123] C. S. Johnson, N. Li, C. Lefief, J. T. Vaughey, M. M. Thackeray, *Chem. Mater.* **2008**, *20*, 6095.

[124] a) W. Liu, G. Hu, K. Du, Z. Peng, Y. Cao, Q. Liu, *Mater. Lett.* **2012**, *83*, 11; b) W. Liu, G. Hu, K. Du, Z. Peng, Y. Cao, *Surf. Coat. Technol.* **2013**, *216*, 267.

[125] a) X. Xiong, D. Ding, Y. Bu, Z. Wang, B. Huang, H. Guo, X. Li, *J. Mater. Chem. A* **2014**, *2*, 11691; b) X. Yuan, Q.-J. Xu, X. Liu, H. Liu, Y. Min, Y. Xia, *Electrochim. Acta* **2016**, *213*, 648.

[126] J. Zhang, Y. Cao, X. Ou, J. Zhang, C. Wang, C. Peng, B. Zhang, Y. Tian, *J. Power Sources* **2019**, *436*, 226722.

[127] a) H. Xia, Z. Luo, J. Xie, *Prog. Nat. Sci.: Mater. Int.* **2012**, *22*, 572; b) A. Llusco, M. Grageda, S. Ushak, *Nanomaterials* **2020**, *10*, 1409.

[128] a) Z. Cai, Y. Ma, X. Huang, X. Yan, Z. Yu, S. Zhang, G. Song, Y. Xu, C. Wen, W. Yang, *J. Energy Storage* **2020**, *27*, 101036; b) R. Teng, H.-T. Yu, C.-F. Guo, X.-D. Wang, Y.-J. Qiao, Y. Xie, T.-F. Yi, *Ionics* **2020**, *26*, 3231.

[129] a) S. Jayaraman, V. Aravindan, P. Suresh Kumar, W. C. Ling, S. Ramakrishna, S. Madhavi, *Chem. Commun.* **2013**, *49*, 6677; b) Z. Iskandar Radzi, K. Helmy Arifin, M. Zieauddin Kufian, V. Balakrishnan, S. Rohani Sheikh Raihan, N. Abd Rahim, R. Subramaniam, *J. Electroanal. Chem.* **2022**, *920*, 116623.

[130] E. Han, Y. Li, L. Zhu, L. Zhao, *Solid State Ionics* **2014**, *255*, 113.

[131] J. H. Lee, K. J. Kim, *Electrochim. Acta* **2013**, *102*, 196.

[132] D. Arumugam, G. P. Kalaignan, *Electrochim. Acta* **2010**, *55*, 8709.

[133] J. Zhao, Y. Wang, *Nano Energy* **2013**, *2*, 882.

[134] F. Lai, X. Zhang, H. Wang, S. Hu, X. Wu, Q. Wu, Y. Huang, Z. He, Q. Li, *ACS Appl. Mater. Interfaces* **2016**, *8*, 21656.

[135] C. Lai, W. Ye, H. Liu, W. Wang, *Ionics* **2009**, *15*, 389.

[136] a) J.-S. Kim, C. Johnson, J. T. Vaughey, S. A. Hackney, K. Walz, W. Zeltner, M. Anderson, M. Thackeray, *J. Electrochem. Soc.* **2004**, *151*, A1755; b) J. Yao, C. Shen, P. Zhang, D. H. Gregory, L. Wang, *Ionics* **2013**, *19*, 739.

[137] Q. Chen, Y. Wang, T. Zhang, W. Yin, J. Yang, X. Wang, *Electrochim. Acta* **2012**, *83*, 65.

[138] Y. Wang, X. Wang, S. Yang, H. Shu, Q. Wei, Q. Wu, Y. Bai, B. Hu, *J. Solid State Electrochem.* **2012**, *16*, 2913.

[139] a) A. Tron, Y. D. Park, J. Mun, *J. Power Sources* **2016**, *325*, 360; b) Y. Liu, J. Lv, Y. Fei, X. Huo, Y. Zhu, *Ionics* **2013**, *19*, 1241.

[140] S. Zhao, Y. Bai, Q. Chang, Y. Yang, W. Zhang, *Electrochim. Acta* **2013**, *108*, 727.

[141] a) T. Xu, Y. Li, D. Wang, M. Wu, D. Pan, H. Zhao, Y. Bai, *ACS Sustainable Chem. Eng.* **2018**, *6*, 5818; b) S. Zhao, Y. Bai, L. Ding, B. Wang, W. Zhang, *Solid State Ionics* **2013**, *247–248*, 22.

[142] S. Lee, M. Jeong, J. Cho, *Adv. Energy Mater.* **2013**, *3*, 1623.

[143] a) Y. Shang, J. Liu, T. Huang, A. Yu, *Electrochim. Acta* **2013**, *113*, 248; b) C. Qing, Y. Bai, J. Yang, W. Zhang, *Electrochim. Acta* **2011**, *56*, 6612.

[144] P. Mohan, G. P. Kalaignan, *Ceram. Int.* **2014**, *40*, 1415.

[145] J. Tu, X. B. Zhao, G. S. Cao, D. G. Zhuang, T. J. Zhu, J. P. Tu, *Electrochim. Acta* **2006**, *51*, 6456.

[146] C. Zhang, J. Su, T. Wang, K. Yuan, C. Chen, S. Liu, T. Huang, J. Wu, H. Lu, A. Yu, *ACS Sustainable Chem. Eng.* **2018**, *6*, 7890.

[147] S. M. Abbas, A. M. Hashem, A. E. Abdel-Ghany, E. H. Ismail, M. Kotlár, M. Winter, J. Li, C. M. Julien, *Energies* **2020**, *13*, 5194.

[148] a) J. Cao, S. Guo, R. Yan, C. Zhang, J. Guo, P. Zheng, *J. Alloys Compd.* **2018**, *741*, 1; b) Q. Jiang, X. Wang, Z. Tang, *Fullerenes, Nanotubes Carbon Nanostruct.* **2015**, *23*, 676.

[149] M. Michalska, D. A. Buchberger, J. B. Jasiński, A. K. Thapa, A. Jain, *Materials* **2021**, *14*, 4134.

[150] A. Li, Z. Shao, S. Yang, X. Li, A. Zhang, *Ionics* **2020**, *26*, 3231.

[151] H. Zhang, Z. Zhang, L. Zhao, X. Q. Liu, *Adv. Mater. Res.* **2013**, *734–737*, 2523.

[152] B. Lin, Q. Yin, H. Hu, F. Lu, H. Xia, *J. Solid State Chem.* **2014**, *209*, 23.

[153] P. R. Ilango, K. Prasanna, S. J. Do, Y. N. Jo, C. W. Lee, *Sci. Rep.* **2016**, *6*, 29826.

[154] a) H. Li, H. Zhou, *Chem. Commun.* **2012**, *48*, 1201; b) Q. Liang, J. Gou, Arramel, Q. Zhang, W. Zhang, A. T. S. Wee, *Nano Res.* **2020**, *13*, 3439.

[155] H.-L. Du, M.-G. Jeong, Y.-S. Lee, W. Choi, J. K. Lee, I.-H. Oh, H.-G. Jung, *ACS Appl. Mater. Interfaces* **2015**, *7*, 10250.

[156] L. Su, Y. Jing, Z. Zhou, *Nanoscale* **2011**, *3*, 3967.

[157] L. Zhu, Y. Zhang, X. Zhao, Y. Jiao, Z. Zhao, Y. Wang, N. Yang, *Electrochem. Commun.* **2021**, *124*, 106951.

[158] R. Vidu, P. Stroeve, *Ind. Eng. Chem. Res.* **2004**, *43*, 3314.

[159] L. Su, P. M. Smith, P. Anand, B. Reeja-Jayan, *ACS Appl. Mater. Interfaces* **2018**, *10*, 27063.

[160] J.-W. Fang, J. Wang, Z.-Y. Ji, J.-L. Cui, Z.-Y. Guo, J. Liu, Y.-Y. Zhao, J.-S. Yuan, *Sep. Purif. Technol.* **2022**, *280*, 119726.

[161] a) S. Li, W. Liang, J. Xie, Y. Wei, X. Cui, *J. Electrochem. Energy Convers. Storage* **2020**, *17*, 31007; b) A.-m. Wang, N. Bai, *Solid State Ionics* **2019**, *336*, 19; c) Y.-R. Zhu, T.-F. Yi, X.-Y. Li, Y. Xie, S. Luo, *Mater. Lett.* **2019**, *239*, 56.

[162] a) M.-C. Kim, Y.-W. Lee, T. K. Pham, J. I. Sohn, K.-W. Park, *Appl. Surf. Sci.* **2020**, *504*, 144514; b) S. Li, Y. Wei, P. Wang, Y. Feng, W. Liang, H. Ding, X. Cui, *J. Alloys Compd.* **2020**, *820*, 153140.

[163] a) N. P. W. Pieczonka, L. Yang, M. P. Balogh, B. R. Powell, K. Chemelewski, A. Manthiram, S. A. Krachkovskiy, G. R. Goward, M. Liu, J.-H. Kim, *J. Phys. Chem. C* **2013**, *117*, 22603; b) D. Zhao, S. Song, X. Ye, P. Wang, J. Wang, Y. Wei, C. Li, L. Mao, H. Zhang, S. Li, *Appl. Surf. Sci.* **2019**, *491*, 595.

[164] a) X. Yang, T. Yang, S. Liang, X. Wu, H. Zhang, *J. Mater. Chem. A* **2014**, *2*, 10359; b) X. Xu, S. Deng, H. Wang, J. Liu, H. Yan, *Nano-Micro Lett.* **2017**, *9*, 22.

[165] X. Fang, F. Lin, D. Nordlund, M. Mecklenburg, M. Ge, J. Rong, A. Zhang, C. Shen, Y. Liu, Y. Cao, M. M. Doeff, C. Zhou, *Adv. Funct. Mater.* **2017**, *27*, 1602873.

[166] S. Tao, F. Kong, C. Wu, X. Su, T. Xiang, S. Chen, H. Hou, L. Zhang, Y. Fang, Z. Wang, W. S. Chu, B. Qian, L. Song, *J. Alloys Compd.* **2017**, *705*, 413.

[167] U. Nisar, R. Amin, R. Essehli, R. A. Shakoor, R. Kahraman, D. K. Kim, M. A. Khaleel, I. Belharouak, *J. Power Sources* **2018**, *396*, 774.

[168] R. L. Patel, S. A. Palaparty, X. Liang, *J. Electrochem. Soc.* **2017**, *164*, A6236.

[169] H. Sun, B. Xia, W. Liu, G. Fang, J. Wu, H. Wang, R. Zhang, S. Kaneko, J. Zheng, H. Wang, D. Li, *Appl. Surf. Sci.* **2015**, *331*, 309.

[170] F. Ma, Y. Wu, G. Wei, S. Qiu, J. Qu, *J. Solid State Electrochem.* **2019**, *23*, 2213.

[171] J. Wang, S. Yao, W. Lin, B. Wu, X. He, J. Li, J. Zhao, *J. Power Sources* **2015**, *280*, 114.

[172] a) W. K. Pang, H.-F. Lin, V. K. Peterson, C.-Z. Lu, C.-E. Liu, S.-C. Liao, J.-M. Chen, *J. Phys. Chem. C* **2017**, *121*, 3680; b) U. Nisar, R. K. Petla, S. Al-Hail, R. Shakoor, R. Essehli, R. Kahraman, S. Al-Qaradawi, D. K. Kim, I. Belharouak, M. Amin, *ACS Appl. Energy Mater.* **2019**, *2*, 7263.

[173] Z.-H. Wu, J.-Y. Shih, Y.-J. Li, Y.-D. Tsai, T.-F. Hung, C. Karuppiah, R. Jose, C.-C. Yang, *Nanomaterials* **2022**, *12*, 409.

[174] J. Y. Shi, C.-W. Yi, K. Kim, *J. Power Sources* **2010**, *195*, 6860.

[175] J. Chong, S. Xun, J. Zhang, X. Song, H. Xie, V. Battaglia, R. Wang, *Chemistry* **2014**, *20*, 7479.

[176] J. W. Kim, D. H. Kim, D. Y. Oh, H. Lee, J. H. Kim, J. H. Lee, Y. S. Jung, *J. Power Sources* **2015**, *274*, 1254.

[177] X. Ding, Y.-X. Li, F. Chen, X.-D. He, A. Yasmin, Q. Hu, Z.-Y. Wen, C.-H. Chen, *J. Mater. Chem. A* **2019**, *7*, 11513.

[178] A. Tron, J. Mun, *J. Solid State Chem.* **2021**, *302*, 122411.

[179] T. Chen, H. Wu, D. Zhou, Y. Zhou, W. Yan, J. Song, J. Guo, *J. Mater. Sci.: Mater. Electron.* **2022**, *33*, 11712.

[180] C.-T. Chu, A. Mondal, N. V. Kosova, J.-Y. Lin, *Appl. Surf. Sci.* **2020**, *530*, 147169.

[181] a) P. Guan, L. Zhou, Z. Yu, Y. Sun, Y. Liu, F. Wu, Y. Jiang, D. Chu, *J. Energy Chem.* **2020**, *43*, 220; b) A. Tron, H. Kang, J. Kim, J. Mun, *J. Electrochem. Sci. Technol.* **2018**, *9*, 60.

[182] J. Li, Y. Zhu, L. Wang, C. Cao, *ACS Appl. Mater. Interfaces* **2014**, *6*, 18742.

[183] J. R. Croy, M. Balasubramanian, D. Kim, S.-H. Kang, M. M. Thackeray, *Chem. Mater.* **2011**, *23*, 5415.

[184] J. Zhang, G. Sun, Y. Han, F. Yu, X. Qin, G. Shao, Z. Wang, *Electrochim. Acta* **2020**, *343*, 136105.

ADVANCED
SCIENCE NEWS

www.advancedsciencenews.com

small
methods

www.small-methods.com

[185] J. C. Deng, Y. L. Xu, L. Li, T. Y. Feng, L. Li, *J. Mater. Chem. A* **2016**, *4*, 6561.

[186] V. Mereacre, P. Stüble, A. Ghamlouche, J. R. Binder, *Nanomaterials* **2021**, *11*, 548.

[187] a) M.-M. Deng, B.-K. Zou, Y. Shao, Z.-F. Tang, C.-H. Chen, *J. Solid State Electrochem.* **2017**, *21*, 1733; b) H. R. Lee, H. R. Seo, B. Lee, B. W. Cho, K.-Y. Lee, S. H. Oh, *Appl. Surf. Sci.* **2017**, *392*, 448.

[188] a) Y. Li, J. She, Z. Hua, H. Chen, M. Ruan, D. Yan, *Nano Lett.* **2003**, *3*, 609; b) M. Choi, K. Na, J. Kim, Y. Sakamoto, O. Terasaki, R. Ryoo, *Nature* **2009**, *461*, 246.

[189] X. Li, Y. Zhang, W. Li, Y. Qiao, H. Shang, W. Ge, M. Qu, W. Fan, Z. Xie, *ChemistrySelect* **2020**, *5*, 2593.

[190] a) T. Yang, N. Zhang, Y. Lang, K. Sun, *Electrochim. Acta* **2011**, *56*, 4058; b) X. Fang, M. Ge, J. Rong, C. Zhou, *J. Mater. Chem. A* **2013**, *1*, 4083.

[191] Y. Kwon, Y. Lee, S.-O. Kim, H.-S. Kim, K. J. Kim, D. Byun, W. Choi, *ACS Appl. Mater. Interfaces* **2018**, *10*, 29457.

[192] J.-H. Cho, J.-H. Park, M.-H. Lee, H.-K. Song, S.-Y. Lee, *Energy Environ. Sci.* **2012**, *5*, 7124.

[193] X. Zheng, W. Liu, Q. Qu, Q. Shi, H. Zheng, Y. Huang, *Appl. Surf. Sci.* **2018**, *455*, 349.

[194] X.-W. Gao, Y.-F. Deng, D. Wexler, G.-H. Chen, S.-L. Chou, H.-K. Liu, Z.-C. Shi, J.-Z. Wang, *J. Mater. Chem. A* **2015**, *3*, 404;

[195] a) H. Wu, G. Chan, J. W. Choi, I. Ryu, Y. Yao, M. T. McDowell, S. W. Lee, A. Jackson, Y. Yang, L. B. Hu, Y. Cui, *Nat. Nanotechnol.* **2012**, *7*, 309; b) M.-H. Park, M. G. Kim, J. Joo, K. Kim, J. Kim, S. Ahn, Y. Cui, J. Cho, *Nano Lett.* **2009**, *9*, 3844.

[196] J. Guo, X. Chen, C. Wang, *J. Mater. Chem.* **2010**, *20*, 5035.

[197] a) Y.-G. Guo, Y.-S. Hu, W. Sigle, J. Maier, *Adv. Mater.* **2007**, *19*, 2087; b) H. Yoo, J.-I. Lee, H. Kim, J.-P. Lee, J. Cho, S. Park, *Nano Lett.* **2011**, *11*, 4324.

[198] Y.-S. Hu, R. Demir-Cakan, M.-M. Titirici, J.-O. Müller, R. Schlögl, M. Antonietti, J. Maier, *Angew. Chem., Int. Ed.* **2008**, *47*, 1645.

[199] a) B. M. Bang, H. Kim, H.-K. Song, J. Cho, S. Park, *Energy Environ. Sci.* **2011**, *4*, 5013; b) H. T. Nguyen, M. R. Zamfir, L. D. Duong, Y. H. Lee, P. Bondavalli, D. Pribat, *J. Mater. Chem.* **2012**, *22*, 24618.

[200] J.-K. Yoo, J. Kim, M.-J. Choi, Y.-U. Park, J. Hong, K. M. Baek, K. Kang, Y. S. Jung, *Adv. Energy Mater.* **2014**, *4*, 1400622.

[201] S. C. Kim, W. Huang, Z. Zhang, J. Wang, Y. Kim, Y. K. Jeong, S. T. Oyakhire, Y. Yang, Y. Cui, *MRS Bull.* **2022**, *47*, 127.

[202] M. Ko, S. Chae, J. Ma, N. Kim, H.-W. Lee, Y. Cui, J. Cho, *Nat. Energy* **2016**, *1*, 16113.

[203] X. Zhao, M. Li, K.-H. Chang, Y.-M. Lin, *Nano Res.* **2014**, *7*, 1429.

[204] M. Choi, J.-C. Kim, D.-W. Kim, *Sci. Rep.* **2018**, *8*, 960.

[205] G. Jeong, J.-G. Kim, M.-S. Park, M. Seo, S. M. Hwang, Y.-U. Kim, Y.-J. Kim, J. H. Kim, S. X. Dou, *ACS Nano* **2014**, *8*, 2977.

[206] C. Yan, T. Huang, X. Zheng, C. Gong, M. Wu, *R. Soc. Open Sci.* **2018**, *5*, 180311.

[207] X. Zhang, D. Wang, X. Qiu, Y. Ma, D. Kong, K. Müllen, X. Li, L. Zhi, *Nat. Commun.* **2020**, *11*, 3826.

[208] a) H. Park, S. Lee, S. Yoo, M. Shin, J. Kim, M. Chun, N.-S. Choi, S. Park, *ACS Appl. Mater. Interfaces* **2014**, *6*, 16360; b) S. Chae, M. Ko, S. Park, N. Kim, J. Ma, J. Cho, *Energy Environ. Sci.* **2016**, *9*, 1251.

[209] a) D. Kim, M. Park, S.-M. Kim, H. C. Shim, S. Hyun, S. M. Han, *ACS Nano* **2018**, *12*, 10903; b) N. Li, Z. Yi, N. Lin, Y. Qian, *Nanoscale* **2019**, *11*, 16781.

[210] a) X. Zhang, T. Fang, Y. Gao, L. Liao, T. Ma, S. Gao, M. Wang, *Mater. Today Energy* **2020**, *18*, 100561; b) Y. Han, M. Chatti, Y. Ge, C. Wang, Y. Chao, A. N. Simonov, G. G. Wallace, *ChemElectroChem* **2019**, *6*, 2338.

[211] a) M. Schnabel, E. Arca, Y. Ha, C. Stetson, G. Teeter, S.-D. Han, P. Stradins, *ACS Appl. Energy Mater.* **2020**, *3*, 8842; b) K. Kong, G. Xu, Y. Lan, C. Jin, Z. Yue, X. Li, F. Sun, H. Huang, J. Yuan, L. Zhou, *Appl. Surf. Sci.* **2020**, *515*, 146026.

[212] F. Wang, G. Chen, N. Zhang, X. Liu, R. Ma, *Carbon Energy* **2019**, *1*, 219.

[213] a) Y. Yu, L. Gu, C. Zhu, S. Tsukimoto, P. A. van Aken, J. Maier, *Adv. Mater.* **2010**, *22*, 2247; b) D. Chen, X. Mei, G. Ji, M. Lu, J. Xie, J. Lu, J. Y. Lee, *Angew. Chem., Int. Ed.* **2012**, *51*, 2409.

[214] S. Yoo, J.-I. Lee, S. Ko, S. Park, *Nano Energy* **2013**, *2*, 1271.

[215] E. L. Memarzadeh, W. P. Kalisvaart, A. Kohandehghan, B. Zahiri, C. M. B. Holt, D. Mitlin, *J. Mater. Chem.* **2012**, *22*, 6655.

[216] a) T. Cetinkaya, M. Uysal, M. O. Guler, H. Akbulut, A. Alp, *Powder Technol.* **2014**, *253*, 63; b) M. T. McDowell, S. Woo Lee, C. Wang, Y. Cui, *Nano Energy* **2012**, *1*, 401.

[217] K. Xu, X. Liu, K. Guan, Y. Yu, W. Lei, S. Zhang, Q. Jia, H. Zhang, *ChemSusChem* **2021**, *14*, 5135.

[218] T. Cetinkaya, M. Uysal, M. O. Guler, H. Akbulut, *Int. J. Hydrogen Energy* **2014**, *39*, 21405.

[219] a) J. Zhou, T. Qian, M. Wang, N. Xu, Q. Zhang, Q. Li, C. Yan, *ACS Appl. Mater. Interfaces* **2016**, *8*, 5358; b) L. Gai, Y. Zhao, G. Song, Q. An, Z. Xiao, S. Zhai, Z. Li, *Composites, Part A* **2020**, *136*, 105965.

[220] R. Huang, Y. Xie, Q. Chang, J. Xiong, S. Guan, S. Yuan, G. Jiang, *Nano* **2019**, *14*, 1950078.

[221] a) M. Tian, P. Wu, *ACS Appl. Energy Mater.* **2019**, *2*, 5066; b) T. B. Truong, Y.-R. Chen, G.-Y. Lin, H.-T. Lin, Y.-S. Wu, C.-C. Yang, *Electrochim. Acta* **2021**, *365*, 137387.

[222] X. Liu, J. Zai, A. Iqbal, M. Chen, N. Ali, R. Qi, X. Qian, *J. Colloid Interface Sci.* **2020**, *565*, 270.

[223] H.-Y. Lin, C.-H. Li, D.-Y. Wang, C.-C. Chen, *Nanoscale* **2016**, *8*, 1280.

[224] J. H. Yoon, G. Lee, P. Li, H. Baik, G.-R. Yi, J. H. Park, *Appl. Surf. Sci.* **2022**, *571*, 151294.

[225] L. Zheng, C. Wei, M. D. L. Garayt, J. MacInnis, M. N. Obrovac, *J. Electrochem. Soc.* **2019**, *166*, A2924.

[226] C. Geng, S. Trussler, M. B. Johnson, N. Zaker, B. Scott, G. Botton, J. R. Dahn, *J. Electrochem. Soc.* **2020**, *167*, 110509.

[227] L. Ma, R. B. Nuwayhid, T. Wu, Y. Lei, K. Amine, J. Lu, *Adv. Mater. Interfaces* **2016**, *3*, 1600564.

[228] Y. Sun, Y. Zhao, J. Wang, J. Liang, C. Wang, Q. Sun, X. Lin, K. R. Adair, J. Luo, D. Wang, R. Li, M. Cai, T.-K. Sham, X. Sun, *Adv. Mater.* **2019**, *31*, 1806541.

[229] a) G. Lefebvre, L. Galet, A. Chamayou, *Powder Technol.* **2011**, *208*, 372; b) F. Cavaillès, R. Sescousse, A. Chamayou, L. Galet, *Adv. Powder Technol.* **2017**, *28*, 2875.

[230] Z. Liu, Z. Wang, T. Lu, P. Dai, P. Gao, Y. Zhu, *J. Alloys Compd.* **2018**, *763*, 701.

[231] H. Visbal, Y. Aihara, S. Ito, T. Watanabe, Y. Park, S. Doo, *J. Power Sources* **2016**, *314*, 85.

[232] S. Yoon, K.-N. Jung, S.-H. Yeon, C. S. Jin, K.-H. Shin, *J. Electroanal. Chem.* **2012**, *683*, 88.

[233] X. Li, X. Zhao, M.-S. Wang, K.-J. Zhang, Y. Huang, M.-Z. Qu, Z.-L. Yu, D.-S. Geng, W.-G. Zhao, J.-M. Zheng, *RSC Adv.* **2017**, *7*, 24359.

[234] C. Yang, X. Zhang, M. Huang, J. Huang, Z. Fang, *ACS Appl. Mater. Interfaces* **2017**, *9*, 12408.

[235] Q. Hou, G. Cao, P. Wang, D. Zhao, X. Cui, S. Li, C. Li, *J. Alloys Compd.* **2018**, *747*, 796.

[236] N. Phattharasupakun, J. Wutthiprom, S. Duangdangchote, S. Sarawutanukul, C. Tomon, F. Duriyasart, S. Tubtimkuna, C. Aphirakaramwong, M. Sawangphruk, *Energy Storage Mater.* **2021**, *36*, 485.

[237] B. A. Walker, C. O. Plaza-Rivera, S.-S. Sun, W. Lu, J. W. Connell, Y. Lin, *Electrochim. Acta* **2020**, *362*, 137129.

[238] F. Schipper, H. Bouzaglo, M. Dixit, E. M. Erickson, T. Weigel, M. Talianker, J. Grinblat, L. Burstein, M. Schmidt, J. Lampert, C. Erk, B. Markovsky, D. T. Major, D. Aurbach, *Adv. Energy Mater.* **2018**, *8*, 1701682.

[239] S. Tubtimkuna, N. Phattharasupakun, P. Bunyanidhi, M. Sawangphruk, *Adv. Mater. Technol.* **2022**, *7*, 2200436.

[240] L. Yao, F. Liang, J. Jin, B. V. R. Chowdari, J. Yang, Z. Wen, *Chem. Eng. J.* **2020**, *389*, 124403.

[241] S.-K. Hu, G.-H. Cheng, M.-Y. Cheng, B.-J. Hwang, R. Santhanam, *J. Power Sources* **2009**, *188*, 564.

[242] H. Zhang, J. Xu, J. Zhang, *Front. Mater.* **2019**, *6*, 309.

[243] Y. Chen, X. Wang, J. Zhang, B. Chen, J. Xu, S. Zhang, L. Zhang, *RSC Adv.* **2019**, *9*, 2172.

[244] W. Zhu, X. Huang, T. Liu, Z. Xie, Y. Wang, K. Tian, L. Bu, H. Wang, L. Gao, J. Zhao, *Coatings* **2019**, *9*, 92.

[245] K. Srimanon, S. Vadivel, M. Sawangphruk, *J. Power Sources* **2022**, *550*, 232150.

[246] D. Li, Y. Kato, K. Kobayakawa, H. Noguchi, Y. Sato, *J. Power Sources* **2006**, *160*, 1342.

[247] M. Michalska, D. A. Buchberger, J. B. Jasiński, A. K. Thapa, A. Jain, *Materials* **2021**, *14*, 4134.

[248] L. Jaber-Ansari, K. P. Puntambekar, S. Kim, M. Aykol, L. Luo, J. Wu, B. D. Myers, H. Iddir, J. T. Russell, S. J. Saldaña, R. Kumar, M. M. Thackeray, L. A. Curtiss, V. P. Dravid, C. Wolverton, M. C. Hersam, *Adv. Energy Mater.* **2015**, *5*, 1500646.

[249] M. J. Young, S. Letourneau, R. E. Warburton, W. M. Dose, C. Johnson, J. Greeley, J. W. Elam, *J. Phys. Chem. C* **2019**, *123*, 23783.

[250] V. Selvamani, N. Phattharasupakun, J. Wutthiprom, M. Sawangphruk, *Sustainable Energy Fuels* **2019**, *3*, 1988.

[251] Y. Zhao, Z. Lv, T. Xu, J. Li, *J. Alloys Compd.* **2017**, *715*, 105.

[252] S. Cho, S. Kim, W. Kim, S. Kim, *Electron. Mater. Lett.* **2019**, *15*, 481.

[253] U. Nisar, S. A. J. A. Al-Hail, R. K. Petla, R. A. Shakoor, R. Essehli, R. Kahraman, S. Y. AlQaradawi, D. K. Kim, I. Belharouak, M. R. Amin, *ACS Appl. Energy Mater.* **2019**, *2*, 7263.

[254] Y. Hwa, W.-S. Kim, S.-H. Hong, H.-J. Sohn, *Electrochim. Acta* **2012**, *71*, 201.

[255] P. Gao, J. Fu, J. Yang, R. Lv, J. Wang, Y. Nuli, X. Tang, *Phys. Chem. Chem. Phys.* **2009**, *11*, 11101.

[256] J. Yu, J. Yang, X. Feng, H. Jia, J. Wang, W. Lu, *Ind. Eng. Chem. Res.* **2014**, *53*, 12697.

[257] J. Wutthiprom, N. Phattharasupakun, C. Tomon, M. Sawangphruk, *Electrochim. Acta* **2020**, *352*, 136457.

[258] H. Dong, X. Fu, J. Wang, P. Wang, H. Ding, R. Song, S. Wang, R. Li, S. Li, *Carbon* **2021**, *173*, 687.

[259] Q. Xu, J.-K. Sun, J.-Y. Li, Y.-X. Yin, Y.-G. Guo, *Energy Storage Mater.* **2018**, *12*, 54.

[260] S. Y. Kim, J. Lee, B.-H. Kim, Y.-J. Kim, K. S. Yang, M.-S. Park, *ACS Appl. Mater. Interfaces* **2016**, *8*, 12109.

[261] S. Jeong, X. Li, J. Zheng, P. Yan, R. Cao, H. J. Jung, C. Wang, J. Liu, J.-G. Zhang, *J. Power Sources* **2016**, *329*, 323.

[262] S.-H. Choi, G. Nam, S. Chae, D. Kim, N. Kim, W. S. Kim, J. Ma, J. Sung, S. M. Han, M. Ko, H.-W. Lee, J. Cho, *Adv. Energy Mater.* **2019**, *9*, 1803121.

[263] Y. Cao, T. D. Hatchard, R. A. Dunlap, M. N. Obrovac, *J. Mater. Chem. A* **2019**, *7*, 8335.

[264] M. Ashuri, Q. He, Y. Liu, S. Emani, L. L. Shaw, *Electrochim. Acta* **2017**, *258*, 274.

[265] Q. Shen, R. Zheng, Y. Lv, Y. Lou, L. Shi, S. Yuan, *Batteries Supercaps* **2022**, *5*, 202200186.

[266] M. N. Obrovac, L. Zheng, M. D. L. Garayt, *Cell Rep. Phys. Sci.* **2020**, *1*, 100063.

[267] a) M. Alonso, M. Satoh, K. Miyanami, *Powder Technol.* **1989**, *59*, 45; b) S. Tubtimkuna, A. Krittayavathananon, P. Chiochan, S. Duangdangchote, J. Wutthiprom, J. Limtrakul, M. Sawangphruk, *Chem. Commun.* **2019**, *55*, 14263.

[268] M. Lu, N. Fatah, A. Y. Khodakov, *J. Mater. Chem. A* **2017**, *5*, 9148.

[269] R. Sharma, R. Setia, *Powder Technol.* **2019**, *356*, 458.

[270] J. Rojas, M. Cruchaga, D. Celentano, M. El Ganaoui, B. Pateyron, **2010**, https://doi.org/10.48550/arXiv.1002.2370.

[271] N. Anansuksawat, P. Chiochan, K. Homlamai, N. Joraleechanchai, W. Tejangkura, M. Sawangphruk, *J. Power Sources* **2023**, *554*, 232324.

[272] C. Tomon, S. Sarawutanukul, N. Phattharasupakun, S. Duangdangchote, P. Chomkhuntod, N. Joraleechanchai, P. Bunyanidhi, M. Sawangphruk, *Commun Chem* **2022**, *5*, 54.

[273] J. Chen, L. Zhu, D. Jia, X. Jiang, Y. Wu, Q. Hao, Y. Xia, Y. Ouyang, L. Peng, W. Tang, T. Liu, *Electrochim. Acta* **2019**, *312*, 179.

[274] L. Zheng, T. D. Hatchard, M. N. Obrovac, *MRS Commun.* **2019**, *9*, 245.

[275] L. Musuvadhi Babulal, S.-H. Wu, C.-C. Yang, *Ceram. Int.* **2020**, *46*, 22606.

[276] M. J. Herzog, N. Gauquelin, D. Esken, J. Verbeeck, J. Janek, *Energy Technol.* **2021**, *9*, 2100028.

[277] M. J. Herzog, D. Esken, J. Janek, *Batteries Supercaps* **2021**, *4*, 1003.

[278] Q. Li, W. Zhuang, Z. Li, S. Wu, N. Li, M. Gao, W. Li, J. Wang, S. Lu, *ChemElectroChem* **2020**, *7*, 998.

[279] P. Chiochan, C. Jangsan, N. Anansuksawat, K. Homlamai, N. Joraleechanchai, W. Tejangkura, M. Sawangphruk, *J. Electrochem. Soc.* **2022**, *169*, 110532.

[280] D. Liu, J. Trottier, P. Charest, J. Fréchette, A. Guerfi, A. Mauger, C. M. Julien, K. Zaghib, *J. Power Sources* **2012**, *204*, 127.

[281] K. Kongsawatvoragul, P. Bunyanidhi, C. Jangsan, W. Tejangkura, M. Sawangphruk, *J. Electrochem. Soc.* **2022**, *169*, 090524.

[282] P. Khadka, J. Ro, H. Kim, I. Kim, J. T. Kim, H. Kim, J. M. Cho, G. Yun, J. Lee, *Asian J. Pharm. Sci.* **2014**, *9*, 304.

[283] Z. H. Loh, A. K. Samanta, P. W. Sia Heng, *Asian J. Pharm. Sci.* **2015**, *10*, 255.

[284] Z. Hussain, *Int. J. Precis. Eng. Manuf.* **2021**, *22*, 679.

[285] Y. Wang, Q. Zhang, Z.-C. Xue, L. Yang, J. Wang, F. Meng, Q. Li, H. Pan, J.-N. Zhang, Z. Jiang, W. Yang, X. Yu, L. Gu, H. Li, *Adv. Energy Mater.* **2020**, *10*, 2001413.

[286] X. Feng, J. Zhang, L. Yin, *Energy Technol.* **2016**, *4*, 490.

[287] C. Shen, X. Fang, M. Ge, A. Zhang, Y. Liu, Y. Ma, M. Mecklenburg, X. Nie, C. Zhou, *ACS Nano* **2018**, *12*, 6280.

[288] W. Shi, H. B. Wu, J. Baucom, X. Li, S. Ma, G. Chen, Y. Lu, *ACS Appl. Mater. Interfaces* **2020**, *12*, 39127.

[289] H. J. Song, S. H. Oh, Y. Lee, J. Kim, T. Yim, *J. Power Sources* **2021**, *483*, 229218.

[290] T. Kozawa, T. Harata, M. Naito, *J. Asian Ceram. Soc.* **2020**, *8*, 309.

[291] J. Chong, J. Zhang, H. Xie, X. Song, G. Liu, V. Battaglia, S. Xun, R. Wang, *RSC Adv.* **2016**, *6*, 19245.

[292] L. Qian, J.-L. Lan, M. Xue, Y. Yu, X. Yang, *RSC Adv.* **2017**, *7*, 36697.

[293] M. Gao, D. Wang, X. Zhang, H. Pan, Y. Liu, C. Liang, C. Shang, Z. Guo, *J. Mater. Chem. A* **2015**, *3*, 10767.

[294] Y. Yang, X. Qu, L. Zhang, M. Gao, Y. Liu, H. Pan, *ACS Appl. Mater. Interfaces* **2018**, *10*, 20591.

[295] J. Zhou, N. Lin, Y. Han, J. Zhou, Y. Zhu, J. Du, Y. Qian, *Nanoscale* **2015**, *7*, 15075.

[296] Z. P. Guo, J. Z. Wang, H. K. Liu, S. X. Dou, *J. Power Sources* **2005**, *146*, 448.

[297] Z. Ma, B. Gao, P. Wu, J. Shi, Z. Qiao, Z. Yang, G. Yang, B. Huang, F. Nie, *RSC Adv.* **2015**, *5*, 21042.

[298] S. Shakeel, H. Rehman, M. Aslam, D. S. Naveed, S. Yasmeen, **2019**, *7*, 165.

[299] B. Vertruyen, N. Eshraghi, C. Piffet, J. Bodart, A. Mahmoud, F. Boschini, *Materials* **2018**, *11*, 1076.

[300] K. Du, H. Xie, G. Hu, Z. Peng, Y. Cao, F. Yu, *ACS Appl. Mater. Interfaces* **2016**, *8*, 17713.

[301] G. Mao, F. Xiao, L. Zeng, R. Tang, J. Li, Q. Zhou, Y. Wang, *J. Alloys Compd.* **2022**, *892*, 162161.

[302] Q. Q. Qiao, H. Z. Zhang, G. R. Li, S. H. Ye, C. W. Wang, X. P. Gao, *J. Mater. Chem. A* **2013**, *1*, 5262.

**ADVANCED
SCIENCE NEWS**

www.advancedsciencenews.com

**small
methods**

www.small-methods.com

[303] S. Choi, D. S. Jung, J. W. Choi, *Nano Lett.* **2014**, *14*, 7120.

[304] N. Ohta, K. Takada, L. Zhang, R. Ma, M. Osada, T. Sasaki, *Adv. Mater.* **2006**, *18*, 2226.

[305] P. Yue, Z. Wang, Q. Zhang, G. Yan, H. Guo, X. Li, *Ionics* **2013**, *19*, 1329.

[306] J. Cheng, X. Li, Z. He, Z. Wang, H. Guo, W. Peng, *Mater. Technol.* **2016**, *31*, 658.

[307] Y. Liu, K. Qian, J. He, X. Chu, Y.-B. He, M. Wu, B. Li, F. Kang, *Electrochim. Acta* **2017**, *249*, 43.

[308] X. Men, T. Wang, B. Xu, Z. Kong, X. Liu, A. Fu, Y. Li, P. Guo, Y.-G. Guo, H. Li, X. S. Zhao, *Electrochim. Acta* **2019**, *324*, 134850.

[309] X. Yang, X. Chen, J. Qiu, M. Li, H. Ming, S. Zhang, T. Zhang, *J. Solid State Chem.* **2021**, *296*, 121968.

[310] D. S. Jung, T. H. Hwang, S. B. Park, J. W. Choi, *Nano Lett.* **2013**, *13*, 2092.

[311] W. An, P. He, Z. Che, C. Xiao, E. Guo, C. Pang, X. He, J. Ren, G. Yuan, N. Du, D. Yang, D.-L. Peng, Q. Zhang, *ACS Appl. Mater. Interfaces* **2022**, *14*, 10308.

[312] Q. Pan, P. Zuo, S. Lou, T. Mu, C. Du, X. Cheng, Y. Ma, Y. Gao, G. Yin, *J. Alloys Compd.* **2017**, *723*, 434.

[313] W. Liu, H. Xu, H. Qin, Y. Lv, F. Wang, G. Zhu, F. Lin, L. Wang, C. Ni, *J. Solid State Electrochem.* **2019**, *23*, 3363.

[314] H. Huang, P. Rao, W. M. Choi, *Curr. Appl. Phys.* **2019**, *19*, 1349.

Suchakree Tubtimkuna is currently a Ph.D. candidate in the Department of Chemical and Biomolecular Engineering, School of Energy Science and Engineering at the Vidyasirimedhi Institute of Science and Technology under the supervision of assoc. prof. Montree Sawangphruk. He received his B.Sc. from the Department of Chemistry at Mahidol University in 2016. In 2022, he was a guest Ph.D. student at the Institute of Energy and Climate Research (IEK-9), Forschungszentrum Jülich, Germany, under the guidance of Prof. Peter H. L. Notten. His current research is focused on material design for the core–shell structure, which can be used for scalable synthesis in Li-ion batteries.

Dmitri L. Danilov has a Ph.D. and a background in physics and mathematics and obtained his M.Sc. at Saint-Petersburg University in 1993. In 2003 he got a Ph.D. degree from the University of Tilburg. In 2002 he joined the Eurandom Institute at Eindhoven University of Technology, being involved in various national and international research projects. His current research interests include the mathematical modeling of complex electrochemical systems, including Li-ion and NiMH batteries, aging and degradation processes, thin-film batteries, and advanced characterization methods. Starting in 2017, he joined IEK-9 in the Forschungszentrum Jülich. He has published as an author and co-author of more than 80 papers and book contributions.

Peter H. L. Notten joined the Philips Research Laboratories (Eindhoven, The Netherlands) from 1975 to 2010. He received his Ph.D. degree from Eindhoven University in 1989. He focuses on energy storage research, including hydrogen and lithium storage materials, new battery technologies, modeling electrochemical systems, and the design of battery-management algorithms. In 2000, he was appointed as professor at TU/e, heading the group Energy Materials and Devices. In 2014, he was appointed International Adjunct Faculty at the Amrita University, Coimbatore (India), as Group Leader at the Forschungszentrum Jülich, and in 2018 as an Honorary Professor at the University of Technology Sydney.